1-1-2011

Dipole moment effects in photodetachment from cluster anions

Foster Mbaiwa
Washington University in St. Louis

WASHINGTON UNIVERSITY IN ST. LOUIS

School of Arts and Sciences

Department of Chemistry

Dissertation Examination Committee:
Richard Mabbs, Chair
John Gleaves
Sophia Hayes
Dewey Holten
Cynthia Lo
Richard Loomis
Yan Mei Wang

DIPOLE MOMENT EFFECTS IN PHOTODETACHMENT FROM CLUSTER

ANIONS

by

Foster Mbaiwa

A dissertation presented to the School of Arts and Science
of Washington University in partial fulfillment of the
requirements for the degree of

DOCTOR OF PHILOSOPHY

December 2011
Saint Louis, Missouri

ABSTRACT OF THE DISSERTATION

DIPOLE MOMENT EFFECTS IN PHOTODETACHMENT FROM CLUSTER

ANIONS

by

Foster Mbaiwa

Doctor of Philosophy in Chemistry

Washington University in St. Louis, 2011

Research Advisor: Professor Richard Mabbs

In this dissertation results from experimental studies on the effect of the dipole moment on photodetachment from solvated iodide anion are presented. The major advantage of using solvated atomic iodide anions $(\mathrm{I}^-\cdot(\mathrm{Y})_n$ (Y = solvent molecule, $n = 1$–3)) to study this effect is that in the ground state, the excess electron is mainly localized on the iodine atom for which photodetachment behavior is well understood. The effect of the electric dipole moment of the resultant neutral cluster on the outgoing electron is studied by comparing the photoelectron angular distributions (PADs) for $\mathrm{I}^-\cdot(\mathrm{Y})_n$ and I^- photodetachment. The results show strong dipole moment effects in the vicinity of direct detachment thresholds due to the presence of dipole-supported states, $[\mathrm{I}(^2\mathrm{P}_{3/2})\cdot(\mathrm{Y})_n]^-$ and $[\mathrm{I}(^2\mathrm{P}_{1/2})\cdot(\mathrm{Y})_n]^-$. Vertical photoexcitation near the threshold for production of the excited neutral cluster $\mathrm{I}(^2\mathrm{P}_{1/2})\cdot(\mathrm{Y})_n$ shows evidence of strong mixing of the direct $(\mathrm{I}^-\cdot(\mathrm{Y})_n \xrightarrow{h\nu} \mathrm{I}(^2\mathrm{P}_{3/2}) + \mathrm{Y}_n + \mathrm{e}^-)$ channel and a dipole-supported state, $[\mathrm{I}(^2\mathrm{P}_{1/2})\cdot(\mathrm{Y})_n]^-$ in the PADs. It is shown that increasing the dipole moment of $\mathrm{I}(^2\mathrm{P}_{1/2})\cdot(\mathrm{Y})_n$ for $n = 1$ increases this channel coupling while for $n > 1$, the situation

is more complex due to competing dynamics. Results are also presented for photode-tachment from a stable dipole-bound CH_3CN^- anion in the vicinity of a well-known electron scattering resonance. Despite the presence of this π^*_{CN} it appears to have very little effect on the photoelectron angular distributions. This initially surprising behavior is attributed to the relatively low contribution of higher partial angular momenta waves in the detachment process.

Acknowledgments

I am grateful to my advisor, Prof. Richard Mabbs for all the guidance and direction over the past six years. There are many things that I have learnt from Prof. Mabbs which will be invaluable in my professional carrier. This work would not have have come this far without his inspiration, support and belief in me. I thank my Graduate work committee members for guiding me through the years.

I appreciate Financial support from Washington University in the form of grants, assistantships etc. I appreciate the staff at the IopenShell-Center for computational studies of electronic structure and spectroscopy of open-shell and electronically excited species (University of Southern California) for allowing me to use their computational facilities to perform *ab initio* calculations. I thank Kadir Diri for helping me to perform calculations using the IopenShell facilities.

I am thankful to the past and current members of the Mabbs Research Group, Diep Bich Dao, Nicholas Holtgrewe, Joshua Lasinski, Matthew Van Duzor and Jie Wei. I enjoyed every moment I spent with them and appreciate their assistance with "time consuming experiments". In particular I thank Matthew Van Duzor who built the photoelectron spectrometer used for the experiments reported in this dissertation. Members of the chemistry department in their different offices and capacities have been very supportive and for that I am grateful.

I would like to thank my friends and family members who have been a source of motivation throughout this period. In particular I appreciate the inspiration from my wife, Kele and daughters Joan and Kempho who have quietly endured few years of my absence.

Finally, I thank God and my Lord Jesus Christ for the grace and sustenance and the energy to do all that I have been able to do.

<div align="right">Foster Mbaiwa</div>

Washington University in Saint Louis
December 2011

Contents

List of Tables

List of Figures

Chapter 1

Introduction

In the field of anion spectroscopy, photodetachment refers to the removal of an "excess" electron from an anion using electromagnetic radiation.

$$AB^- \xrightarrow{\text{h}\nu} AB + e^- \tag{1.1}$$

In photodetachment spectroscopy, the kinetic energy, the number and the direction of flight of the detached electrons are analyzed. A number of molecular and atomic (neutral and anionic) properties such as vibrational frequencies and anharmonicities, force constants, electron affinities, bond lengths and angles can all be obtained using photodetachment. In some cases, it can be useful in probing geometries of transition states in reactions[1–4].

Unlike photoionization (removal of an electron from a neutral atom/molecule), in photodetachment, the departing electron is not subject to a strong Coulombic interaction with its parent. Thus the electron departure following photodetachment from AB^- is often approximated as sudden and not influenced by the neutral AB residue. However, experiments[5–7] and theory[8–10] have shown that AB can influence the electron ejection dynamics particularly if it has a non-zero dipole moment.

Our interest in polar molecules is in part due to the fact that strongly polar molecules can weakly bind electrons to form unconventional anions called *dipole-bound anions*, first proposed by Fermi and Teller[11]. Dipole-bound anions can be formed by electron attachment of electrons with very low kinetic energies to polar molecules. There are important biological implications to this as polar biomolecules may capture electrons and initiate tissue damage. Such slow electrons could be secondary electrons from

ionizing radiation[12, 13]. For example the nucleobases uracil and thymine form dipole-bound anions following slow electron attachment[14]. Dipole bound states may also couple to valence states, which may result in formation of longer lived anions or lead to dissociative reactions[15]. An example of this is $CH_3NO_2^-$. At the equilibrium geometry of neutral CH_3NO_2, $CH_3NO_2^-$ is in fact a dipole-bound anion. However, occupation of the lowest unoccupied molecular orbital (LUMO), a π^* orbital, results in a stable valence anion. The potential energy surfaces of these two types of anions interact, which has lead to the suggestion that dipole-bound anions may act as doorway states to valence anion formation[15, 16]. A similar mixing of the states occurs in uracil, but in this case the valence state is a dissociative σ^* resonance[17].

Dipole-bound anions are also important in astrophysical chemistry. Of the more than 200 bands from the diffuse interstellar clouds, the origin of very few is known[18]. It has been proposed that many of the absorption bands are due to photon excitation of anions from their ground states to dipole bound excited states just below detachment thresholds[19].

Early experimental investigations of dipole moment effects on photodetachment were performed by the groups of Lineberger[6, 20] and Brauman[5], who monitored the dependence of the photoelectron intensity (σ) on photon energy for photodetachment leading to polar molecules. By studying photodetachment from OH^-, Lineberger and co-workers showed that due to the long-range dipole potential between the electron and OH, the intensity rises as $\sigma \propto eKE^{1/4}$ near the rotational threshold, deviating from the $\sigma \propto eKE^{1/2}$ expected based on the Wigner law for photodetachment (eKE is the kinetic energy of the ejected electron). Similar results were obtained by Janousek and Brauman[5] with CH_3S^-.

Such experiments relied on starting with a stable molecular anion for which the corresponding neutral molecule has a permanent dipole moment. Unfortunately, the vast majority of polar molecules do not possess stable anionic states. The water molecule, H_2O, is in this category. In this dissertation, a different method is employed, photodetachment from cluster anions of the type $X^- \cdot Y$(X = atomic halide, Y = polar molecule).

$$X^- \cdot Y \xrightarrow{h\nu} X \cdot Y + e^- \tag{1.2}$$

The advantage of this method is that such cluster anions can be made easily in a supersonic expansion. Secondly, the dipole moment can be tuned by changing the solvent molecule Y. Changing the number of solvent molecules may also alter the dipole moment of the neutral cluster.

These cluster anions are also interesting for a number of other reasons. It is implied in the formula $X^-\cdot Y$ that the excess electron resides on the X atom. However, this is not always the case. While the negative charge is mainly localized in X for $X^-\cdot CO_2$ (X = Cl, Br and I), for X = F, this is not so, and the formula is at best written as FCO_2^-[21]. Due to interaction of X^- with molecule Y, the geometry of Y may be perturbed to a degree dependent on the potentials acting between X^- and Y. In this dissertation, the effect of the presence of Y on the electronic states and transitions of X are examined.

The photoelectron spectra of atomic halides in general have been well characterized theoretically and experimentally[22–26]. It will be shown that in most $X^-\cdot Y$ clusters, the charge is localized on X^- and the dipole moment of the neutral cluster $[X\cdot Y]$ accessed by vertical excitation of X^-Y has a strong effect on the detachment dynamics only over very specific energy ranges.

This work builds upon the studies of Johnson and co-workers[27–30], who monitored neutral products (X, Y or $X\cdot Y$) from photodetachment from $X^-\cdot Y$ cluster anions. The increase in the photoneutral intensity in the vicinity of detachment thresholds was ascribed to the formation of dipole-bound anions. Rather than monitoring photoneutral products, photoelectron spectra (I(eKE)) and photoelectron angular distributions, $I(\theta)$, of the detached electron will be monitored. In terms of a comparative study, monitoring $I(\theta)$ is particularly advantageous from an experimental perspective as will be shown below. Below (Section 1.1), a more detailed look at photodetachment is presented. Fundamental concepts (chemical and physical) of electron-molecule interaction will also be introduced.

1.1 Photodetachment

Let us consider again equation 1.1. The energy level diagram shown in Figure 1.1 illustrates the different energetic concerns involved in the process of photodetachment. In a *direct photodetachment* experiment the photon energy, $h\nu$ $(= {}^{hc}/\lambda)$, is higher than the minimum energy required to detach the excess electron. For atomic anions, this minimum energy corresponds to the electron affinity (EA) of the atom. If the photon energy is high enough, photodetachment might leave the molecule or atom in an excited state, $[AB]^*$ or $[AB]^{**}$. For molecules, the Born-Oppenheimer approximation suggests that photodetachment accesses neutral AB at the equilibrium geometry of AB^-. Such transitions are said to be vertical. This may not necessarily correspond to the global minimum on the neutral AB ground state potential energy surface. The neutral state accessed may be vibrationally and/or rotationally excited. The energy needed to access any final quantum state of AB from AB^- is called the electron binding energy (eBE). Since the photon energy has to be in excess of the minimum energy needed to detach the electron, conservation of energy requires energy in excess of eBE to be released as kinetic;
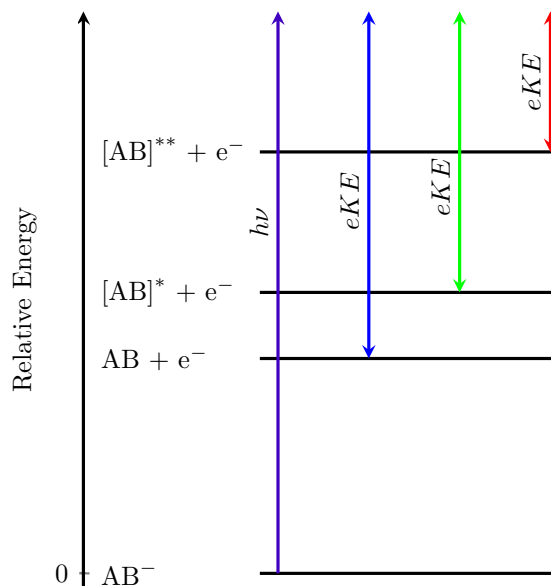
Figure 1.1: Generic energy level diagram for AB anion and neutral molecule AB. The blue, green and red arrows represent electron kinetic energies.

$$KE = h\nu - eBE \tag{1.3}$$

The kinetic energy will be partitioned among various fragments, in this case the electron and molecule (or atom) AB according to the equations[31];

$$KE_{e^-} = KE * \frac{M_{\text{AB}}}{M_{\text{AB}^-}} \tag{1.4}$$

$$KE_{\text{AB}} = KE * \frac{M_{e^-}}{M_{\text{AB}^-}} \tag{1.5}$$

Where KE_{e^-} and KE_{AB} represent the partitioning of the kinetic energy and M_{e^-}, M_{AB} and M_{AB^-} are the masses of the electron, molecule AB and anion AB^- respectively. Since M_{e^-} is much smaller than M_{AB}, for photodetachment, the kinetic energy released is essentially the electron kinetic energy (eKE)[31];

$$eKE = h\nu - eBE \tag{1.6}$$

In photodetachment, the kinetic energy of the *photoelectrons* is measured to give a photoelectron spectrum. For a given anion AB^-, the different processes and final states of AB are usually (colloquially) called "Channels". In Figure 1.1 the eKE corresponding to the different channels is represented by the blue, green and red arrows.

If the electric field of the detachment photons is polarized, electrons may show a preference for ejection in certain directions. These photoelectron angular distributions (PAD) can be measured. In Section 1.1.1 PAD will be presented in more detail and it will be shown how the PADs may be used for probing electron-molecule interactions.

In the case of rotational and vibrational excitation, it is possible to extract fundamental spectroscopic data such as bond lengths, rotational constants, vibrational anharmonicities, electron affinities etc. from the photoelectron spectra. Vertical excitation may access unstable states of the neutral and, in some cases, transition state regions of the potential energy surface. An example is photodetachment from ClHCl^-. Based on the calculated potential energy surfaces the transition state for the halogen exchange reaction $\text{Cl} + \text{HCl} \rightarrow \text{ClH} + \text{Cl}$[3] is linear with equivalent $\text{H} \cdots \text{Cl}$ bond lengths. Experimental studies have shown that the anion ClHCl^- is also linear with equivalent $\text{H} \cdots \text{Cl}$ bond lengths[3]. Therefore, photodetachment from ClHCl^- probes

the transition state.

There are also *Indirect photodetachment* processes in which excitement of AB$^-$ by the photon is the first step.

$$AB^- \xrightarrow{\text{h}\nu} AB^{-*} \longrightarrow AB + e^- \tag{1.7}$$
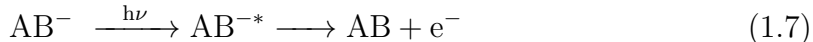
The eKE here is no longer simply based on (1.6) as electron loss is no longer correlated directly with the photon energy but by the interaction of the neutral AB surface with that of the excited state AB^{-*}.

Excited states of most anions lie higher in energy than the lowest states of the corresponding neutral species. Therefore the excited states of such anions will be unstable. Such transient anionic states are known as *resonances*. Resonance lifetimes range from 10^{-15} to 10^{-10} s[32, 33]. Therefore equation 1.7 can also represent resonance formation following excitation. Resonances are known to affect the dynamical behavior of slow electron interaction with molecules[34]. If the lifetime of the resonance is comparable to the timescale of nuclear motion, processes such as vibrational excitation and fragmentation may occur.

For molecules the formation of resonances is usually due to the trapping of an electron in a potential associated with the neutral molecule's ground electronic state. This potential is usually due to centrifugal, polarization and exchange forces. Such a resonance is called *shape resonance*[33]. A Resonance can also form by an electron binding to an electronically excited state[35]. This type of resonance is termed *Feshbach resonance*.

To date, most of the studies involving electron-molecule resonances have been performed using electron scattering methods[32, 33]. The study of resonances using photodetachment was first demonstrated in atomic anions by Patterson and coworkers on alkali metal anions[36]. As pointed out by Lee[37], because of electric-dipole selection rules in photodetachment, only a finite number of final states are possible making interpretation slightly easier. Photodetachment is potentially powerful method of studying electron-molecule resonances.

1.1.1 Photoelectron angular distributions

As mentioned previously, an important measurable quantity in photodetachment is the intensity of the photoelectron signal as a function of the detection angle, ($I\left(\theta\right)$ or $\frac{d\sigma}{d\Omega}$). As will be shown, there is an intrinsic relationship between the photoelectron angular distributions and the orbital from which it is ejected from. The angular distribution for photodetachment from an initial state described by the wavefunction $|\psi_i\rangle$, to a final state described by wavefunction $|\psi_f\rangle$, is expressed as[38]

$$\frac{d\sigma}{d\Omega} = \left(\frac{4\pi^2\alpha m\omega}{\hbar}\right)\kappa\left|\boldsymbol{\varepsilon}_p\cdot\langle\psi_f|\sum_n r_n|\psi_i\rangle\right|^2 \tag{1.8}$$

where α = fine structure constant, m is the reduced mass, ω is the frequency of the photon, $\hbar$ is the reduced Planck's constant ($^h/_{2\pi}$), κ is the wave vector of the photoelectrons ejected onto the solid angle Ω, $\boldsymbol{\varepsilon}_p$ is the unit vector in the direction of the polarization of the incident radiation, r_n is the position of nth electron and σ is total or integrated photoelectron intensity[38]. The above equation assumes the validity of the dipole approximation, that is the wavelength of the photodetachment photon is larger than the molecular or atomic size. For a one electron system, Cooper and Zare[39] express $|\psi_i\rangle$ as a product of the radial wavefunction $R_{n,\ell}$ and angular wavefunction $Y_{\ell m}(\hat{r})$. Only the correct asymptotic form of a plane wave and incoming spherical waves is required for the final $|\psi_f\rangle$, which is a continuum state of the atom without a definite angular momentum, thus

$$|\psi_i\rangle = R_{n,\ell}Y_{\ell m}(\hat{r}) \tag{1.9}$$

and

$$|\psi_f\rangle = 4\pi\sum_{\ell',m'}(i)^{\ell'}\exp^{-i\delta_{\ell'}}Y^*_{\ell'm'}(\hat{\kappa})Y_{\ell'm'}(\hat{r})G_{\kappa\ell'}(r) \tag{1.10}$$

$G_{\kappa\ell'}(r)$ is the radial wavefunction divided by κr and $\delta_{\ell'}$ is the phase shift of the partial wave ℓ'. $Y_{\ell m}$ and $Y^*_{\ell'm'}$ are spherical harmonic functions.

For one electron systems and assuming the laser electric field lies along the z-axis

(Figure 1.2) , equation 1.8 reduces to

$$\frac{d\sigma}{d\Omega} = \left(\frac{4\pi^2 \alpha m \omega \kappa}{\hbar}\right) |\langle \psi_f | z | \psi_i \rangle|^2 \tag{1.11}$$

where

$$z = \sqrt{\left(\frac{4\pi}{3}\right)} r Y_{10}(\hat{r}) \tag{1.12}$$

The integral in 1.11 is non-zero if the following rules apply

$$m' = m$$

$$\ell' = \ell \pm 1$$

Following these selection rules and further simplifying algebra, the expression for a
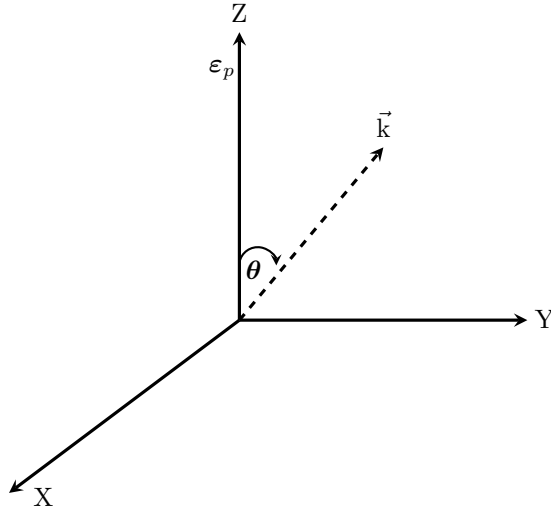
Figure 1.2: Laboratory frame coordinate system for photodetachment. $\vec{k}$ is the direction of the photoelectron and ε_p is the laser polarization vector

one photon photodetachment differential cross section is written as[39, 40]

$$\frac{d\sigma}{d\Omega} = I(\theta) = \frac{\sigma}{4\pi} \left[1 + \beta P_2 \left(\cos \theta\right)\right] \tag{1.13}$$

8

where $P_2\left(\cos\theta\right) = \frac{1}{2}\left(3\cos^2\theta - 1\right)$ and, β, the anisotropy parameter is defined as

$$\beta = \frac{\ell\left(\ell - 1\right)\sigma_{\ell-1}^2 + \left(\ell + 1\right)\left(\ell + 2\right)\sigma_{\ell+1}^2 - 6\ell\left(\ell + 1\right)\sigma_{\ell+1}\sigma_{\ell-1}\cos\left(\delta_{\ell+1} - \delta_{\ell-1}\right)}{\left(2\ell + 1\right)\left[\ell\sigma_{\ell-1}^2 + \left(\ell + 1\right)\sigma_{\ell+1}^2\right]}$$

(1.14)

where $\delta_{\ell-1}$ and $\delta_{\ell+1}$ are the phase shifts of the partial waves $\ell - 1$ and $\ell + 1$ and the the dipole integrals $\sigma_{\ell-1}$ and $\sigma_{\ell+1}$, effectively the partial cross sections for each partial wave, are given by

$$\sigma_{\ell\pm1} = \int_0^\infty r R_{n,\ell} G_{\kappa\ell\pm1}\,dr$$

(1.15)

β only has a physical meaning if values range from 2 to -1. $\beta = 2$ corresponds to a pure $\cos^2\theta$ distribution and $\beta = -1$ for a pure $\sin^2\theta$ distribution.

General comments may be made about equations (1.13) and (1.14).

1. Although equation (1.13) was presented here for a one-electron system it is also applicable to photodetachment and photoionization from randomly oriented many electron systems using a linearly polarized laser. Cooper and Zare[39] also showed that equation (1.14), commonly referred to as the Cooper-Zare equation, is also applicable to many electron atom systems in the dipole approximation provided that configuration interaction and relativistic effects are ignored. Numerically, the expression suggests that photodetachment from an s-orbital should result in $\beta = 2$. For $\ell \neq 0$ the distribution is not proportional to $\cos^2\theta$ contrary to classical expectation. This is because for $\ell \neq 0$ two partial waves, $\ell - 1$ and $\ell + 1$, for the detached electron are possible. The value of β is determined by the interference between the two partial waves.

2. The parameter β completely describes the photoelectron angular distributions within the dipole approximation and thus it is a very convenient quantity with which angular distributions can be compared and/or discussed.

The validity of the Cooper-Zare equation was first demonstrated experimentally by Hall and Siegel[41], who showed that for C^- and O^- anions the angular distribution of photoelectrons deviates from the classical distribution. Angular distributions for a wide variety of anions have been measured such as I^-[42], Cu^-[43] and V^-[44].

From the foregoing discussion, it can seen that for atomic systems the β parameter can be used as a probe for the photodetachment orbital. Reference [45] gives a more detailed discussion of this connection by comparing the photoelectron angular distributions of H^- and I^-.

For molecules complications arise because ℓ is generally not a good quantum number for molecular orbitals. In addition the presence of rotational states may lead to angular momentum coupling between rotational and electronic states[46]. Some dependence on vibrational excitation of the angular distributions adds further complication[47]. However, qualitative treatments relating the molecular anion PAD to the molecular structure have shown some success[48].

Our discussion of angular distributions up to this point has ignored the interaction of the departing electron with the parent atom or molecule. In the absence of such an interaction the dipole integrals have a dependence on the electron momentum $k, \left(= \sqrt{2m_e KE} \right)$, based on the Wigner laws for photodeatchment[49, 50]. This implies that in the limit of no phase changes between the two partial waves, β should vary smoothly with the electron kinetic energy. However, theoretical studies incorporating long-range interactions have shown that β may be sensitive to effects such as resonances[51, 52]. However, despite evidence for resonances in total photodetachment cross sections for a number of anions (eg in Cs^-[53], Na^-[54]), experimental data on angular distributions near these resonances are rare. The measurements reported in this dissertation redress in part this lack of data.

1.2   The dipole interactions on photodetachment

Wigner derived threshold laws for the behavior of cross sections near threshold for a number of processes in which two fragment particles can interact[49]. The cross section depends on the longest range potential between the two. The longest range potential between an electron and an atom following photodetachment from an atomic anion is the centrifugal potential[55]

$$V = \frac{\ell' \left(\ell' + 1 \right) \hbar^2}{2mr^2} \tag{1.16}$$

where m is the electron mass and r is the distance between the electron and the atom. For this potential, near threshold

$$\sigma_{\ell'} \propto k^{2\ell'+1} \tag{1.17}$$

For solving the Schrödinger equation for an electron with orbital angular momentum quantum number ℓ' departing from an atom after photodetachment, the centrifugal term is added to the other short range potentials to obtain an effective potential. For example, if the atom is highly polarizable, the effective potential is[56]

$$V_{eff} = -\frac{\alpha(\hat{r})}{2r^4} + \frac{\ell'(\ell'+1)\hbar^2}{2mr^2} \tag{1.18}$$

In this equation α is the polarizability of the atom and r is the distance between the electron and the atom. Such a potential will create a barrier whose height depends on the value of ℓ'. At low eKE, only low ℓ' partial waves will be sufficiently energetic to escape. The deviation of the experimental results of Lineberger[6, 20] and Brauman[5] from the Wigner threshold law show that for polar molecules the dipole effects come into play. The extension of threshold laws to polar molecules is difficult because of the anisotropic nature of the dipole potential. Beside, as already mentioned, ℓ is not usually a good quantum number for molecules. If θ is the angle between the electron and the dipole vector, for a molecule with a dipole moment μ, the dipole potential is given by

$$V = -\frac{\mu}{r^2}\cos\theta \tag{1.19}$$

O'Malley[57] and Engelking[10] have extended the Wigner law to photodetachment leading to a polar neutral state[57]. Engelking's close-coupling model for an electron interacting with a dipole predicts a rotational level dependence for the cross section behavior near thresholds. Such dependence was proved experimentally for OH^- photodetachment by Smith et al.[7]. The general conclusion so far from the experimental and theoretical studies is that for photodetachment leading to a polar molecule, the cross section rises faster than the Wigner law predicts. This is because in the presence of a dipole potential, the centrifugal potential is no longer the longest range potential between the electron and the molecule[7].

1.2.1 Dipole-bound anions

Strongly polar molecules can bind an electron to form dipole-bound anions. Fermi and Teller proposed that an electron can be bound by a point dipole provided the dipole moment is greater than 1.6 D[11]. Subsequent theoretical and experimental studies for more realistic rotating dipoles refined this value to a range 2.0–2.5 D[58, 59]. A number of such *dipole-bound anions* have since been made experimentally[14, 60–65]. In dipole-bound anions the excess electron orbital is diffuse, much like a Rydberg orbital. Unlike valence orbitals most of the electron density for dipole-bound anions lies outside the molecular framework towards the positive end of the dipole. Consequently, the electron is loosely bound to the neutral molecule by a few tens of meV. A usual test of dipole binding is that the excess electron should be detachable by modest electric fields. For example, the excess electron in the acetonitrile dipole-bound anion, CH_3CN^-, (vertical detachment energy of 18.2 meV[66]) can be detached using an electric field of about 10 kV/cm[67]. Since the dipole bound orbital lies far from the neutral framework, occupation of this orbital essentially leaves the geometry of the neutral molecule unperturbed. Stockdale et al.[60] originally exploited these properties in order to prepare dipole-bound anions by colliding highly excited atoms in rydberg states (A^{**}) in quantum state (n, ℓ) with polar molecules (BC) motivated by the theoretical results of Matsuzawa[68].

$$A^{**}(n, \ell) + BC \longrightarrow A^+ + BC^-$$
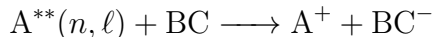
Because of the similarities in orbitals, electron transfer from the rydberg atom to the polar solvent is possible. Because of the proximity of the dipole bound and neutral potential energy surfaces, excited rovibrational states of dipole-bound anions may easily autodetach and may be considered as Feshbach resonances[29].

1.3 Overview of dissertation

The goal of the work reported here is to investigate the effect of the dipole potential on electron photodetachment. The findings are detailed in the next six Chapters of the dissertation. The next chapter details the experiment and methods used in the

investigation. In Chapter 3 photodetachment from $I^-\cdot C_4H_5N$ (C_4H_5N = pyrrole) and $I^-\cdot CO_2$ (CO_2 = carbon dioxide) will be studied. This chapter illustrates some of the basics of photoelectron spectroscopy such as vibrational excitation due to distortion of molecule Y by interaction with X^-, effect of Y on the energy levels of X etc. Chapter 4 focuses on the effect of the solvent dipole moment on photodetachment from $I^-\cdot Y$. This is done by using solvents of different dipole moments. Rather than changing the solvent molecule to change the dipole moment, in Chapter 5, the number of solvent molecules around I^- is increased, which effectively changes the dipole moment of the neutral core. In Chapter 6 a somewhat different strategy is used. Here photodetach is directly from a dipole-bound anion CH_3CN^-. Chapter 7 will give a conclusion of our findings as well as suggest future experiments.

Chapter 2

Experimental methods

In this chapter, a general description of the instrumentation and experimental approach will be given. Specific details of individual experiments will be presented in the appropriate chapters. The instrument can be divided functionally into three main units; (1) anion production, (2) separation of the ions by mass and (3) detection of the anions and electrons. The three regions are enclosed in a vacuum chamber which is differentially pumped. Typical operation pressures are 8×10^{-6} Torr and 8×10^{-9} Torr for the ion source and detection regions respectively. Anion production is based on supersonic expansion and anions are separated by time of flight (TOF) mass spectrometry. Velocity mapped imaging (pioneered by Eppink and Parker[69]) is used for photoelectron detection. Synchronization of spectrometer, laser and data collection computer software is controlled by an 8-channel digital pulse and delay generator (Berkeley Nucleonics Corporation, BNC 565). A schematic of the instrument is shown in Figure 2.1 and detailed descriptions of each of the units are given below.

2.1 Anion production

In the field of anion photoelectron spectroscopy, production of dense anion beams with low internal temperature is crucial. This is because during the mass selection and other necessary processes before detachment a significant amount of anions are lost[70]. Anions with low internal temperature are more likely to survive until photodetachment and the resulting photoelectron spectra are likely to to be less congested due to the absence of hot-bands. With high neutral number densities and associated cooling, the throat of a supersonic expansion is the ideal place to produce
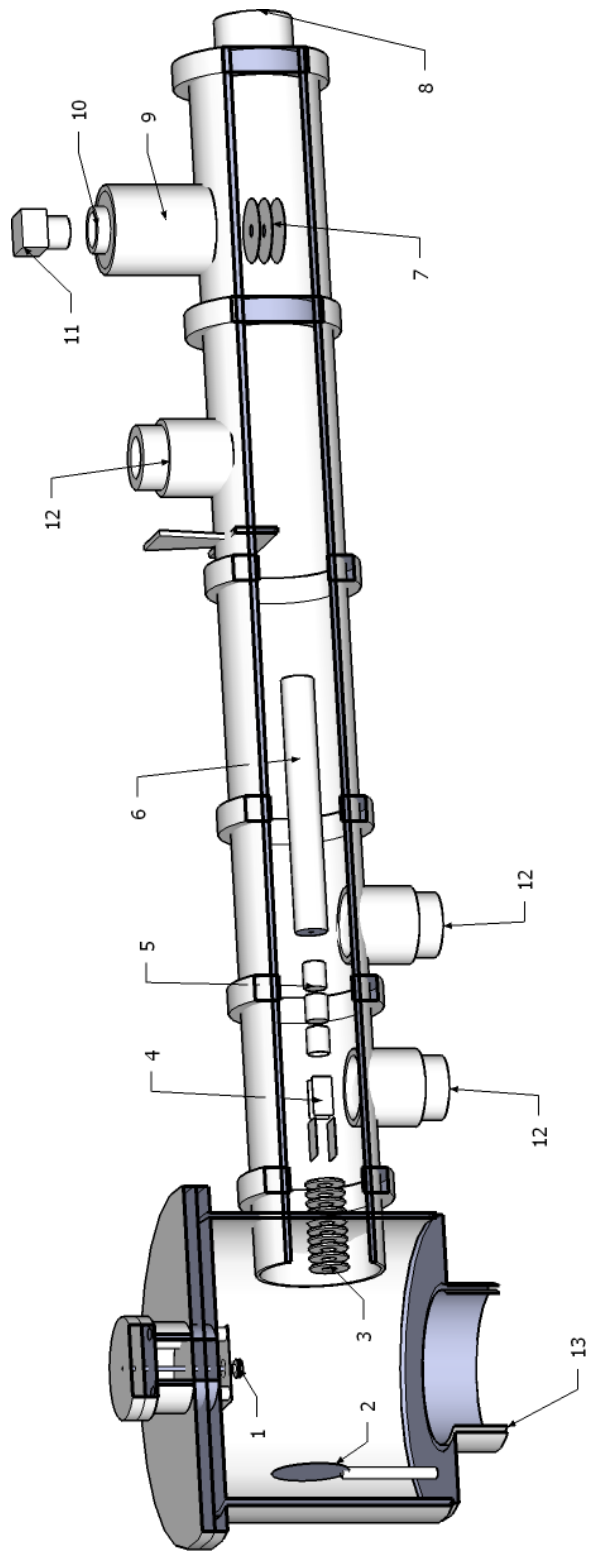
Figure 2.1: Sketch of the cross section of the velocity mapped photoelectron imaging spectrometer showing the various components: ion source (1), anion repeller (2), acceleration stack (3), deflection plates (4), einzel lens (5), potential switch (6), imaging electrodes (7), anion MCP (8), electron TOF tube (9), imaging MCP and phosphor screen (10), CCD camera (11), turbo molecular pumps (12), diffusion pump (13).

anions[71, 72]. For the past few years this has been the method of choice for most anion photoelectron spectroscopy groups[48, 73–77]. Inherent in the cooling due to supersonic expansion is that molecules and anions can easily aggregate to form cluster anions that live long enough to allow spectroscopic studies[78].

For supersonic expansion, a gaseous sample at high pressure is expanded to lower pressure through a small diameter orifice. The result is that random thermal motion of the gas particles is converted into directed motion[71, 78, 79]. The narrow velocity distribution of the beam implies low translational temperature [78]. Internal degrees of freedom (vibrations and rotations) relax to lower temperature as well due to collisions and energy transfer to the translational bath[80, 81]. Usually the precursor gas molecule for the target anion is diluted to very low concentrations in an inert gas. For production of ionic beams, the gas can be ionized at the throat of the expansion using an electric arc or by the impact of energetic electrons. The exact mechanism of formation of anions following ionization is poorly understood, but it is generally agreed that anion formation is a multi-step process[82]. In the case of ionization by electron impact, slower secondary electrons from ionization of the carrier gas molecules may attach to nearby neutral clusters to form cluster anions. Smaller clusters and bare anions may be formed by solvent evaporation which also results in cooling of the resultant anion[82]. An example is the production of O_2^-[82, 83];

$$O_2 + e^- (\text{ 1 KeV}) \rightarrow O_2^+ + e^- (\text{slow}) + e^- (<1 \text{ KeV}) \qquad \text{Ionization} \qquad (2.1)$$
$$O_4 + e^- (\text{slow}) \rightarrow O_4^- \qquad \text{Electron Attachment} \quad (2.2)$$
$$O_4^- \rightarrow O_2^- + O_2 \qquad \text{Fragmentation} \qquad (2.3)$$
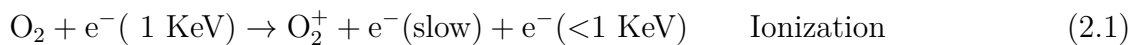
In cases where a precursor molecule is diluted in a buffer gas it is the buffer gas that is most likely to be ionized due to its high concentration. The initial neutral clusters are also likely to contain a large number of buffer gas molecules and therefore the ease with which they evaporate to form anions and smaller anionic clusters is important. In that regard inert gases (usually helium or argon) offer an advantage since these are less likely to bind to the anion of interest.

In our laboratory a gaseous mixture of argon buffer gas and precursor molecule at variable stagnation pressures are introduced into the vacuum chamber via a pulsed solenoid nozzle (General Valve, Series 9, 0.76mm orifice diameter) driven by a valve driver (General Valve, Iota One) operating at 10 Hz. The internally triggered valve driver also produces a TTL pulse that acts as an external trigger for the pulse and delay generator. Most of the experiments reported in this dissertation were done using electron impact ionization. In this case, the ionization is achieved by intersecting the expansion a few nozzle diameters below the nozzle by electrostatically focused energetic electrons (1000V) from an electron gun (Kimball Physics, EGPS 1017).
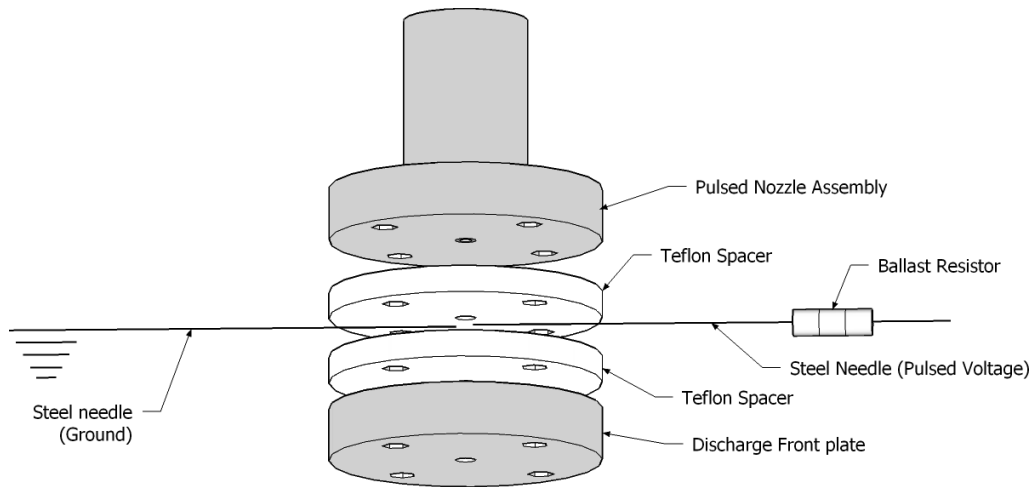
Figure 2.2: Sketch of the disassembled discharge source: The pulsed nozzle housing and the front plate are made of stainless steel and connected to ground. The two steel needles are held tightly between two grooved Teflon spacers. Teflon screws are used to hold the pieces together.

Use of electron impact ionization requires that the electron gun be operated at high filament current. Therefore routine maintenance is necessary as the cathode lifetime is shortened by operating at high current. This problem can be circumvented by using a discharge source. Most of the experiments in Chapters 3, 4 and 6 were performed using electron impact ionization. For Chapter 5 experiments, the discharge source was used. Our discharge source design is a slight modification of that used by Osborn et al[84]. The discharge source assembly, shown in Figure 2.2 consists of a pulsed nozzle (same one used for the electron impact) and a pair of stainless steel needles, one held at ground and the other pulsed and negatively biased against it at -300 to -900V (Directed Energy Inc., PVM 4210). The voltage pulse is of 10-50 μs duration.

The needle tips are 1.5 mm apart and each needle slightly protrudes into the gas stream. The Teflon pieces are used for isolating the nozzle from the needles and also to confine the discharge before the expansion. This confinement has been found to be necessary for formation of larger clusters[85]. In our experience, the discharge source usually results in less stable signal compared to the impact ionization source. Intersecting the expansion after the discharge with a low current (<50 μA) electron beam from the electron gun stabilizes the discharge[77, 84].

The above designs are very versatile in that switching between either is achieved simply by eliminating or maintaining the voltage bias of the discharge and increasing or decreasing the source current on the electron gun to use electron impact ionization or electrical arc source.

2.2   Anion separation

Anions are separated in a Wiley-McLaren time-of-flight mass spectrometer[86]. A repeller plate of variable pulsed potential (-900V to -3000V)[Fig.2.1(2)] supplied by a voltage pulse generator (Directed Energy Inc., PVX 4140) is used. Entrance into the time of flight is via a 0.5" diameter orifice. Upon entering the time of flight tube, the anions are accelerated using the acceleration stack[Fig.2.1(3)], a series of resistively connected plates, to 2 keV. Past the acceleration stack, these are steered using using two pairs of deflection plates[Fig.2.1(4)] towards an einzel lens[Fig.2.1(5)] for focusing. Upon exiting the einzel lens, the anions experience a potential of about 2 kV and are re-referenced to ground using a "Johnson type" potential switch[87]. The potential switch is a 60 cm long stainless steel tube of 7.5 cm diameter and its voltage is pulsed so that anions enter the tube when the potential is at 1.95 kV. While the anions are still inside the tube, the voltage is dropped to ground using a fast acting high voltage pulse generator (Directed Energy Inc., 4140). The ions then exit the tube at a kinetic energy of 1.95 keV but referenced to ground.

The length of the potential switch has important practical considerations. Since the potential switch length covers only part of the whole anion flight length, only a given range of masses can be inside the potential switch for a given 1.95 kV pulse. Any anions outside the potential switch by the time the voltage pulse is off (0 V) will

experience a potential gradient, be deflected and likely collide with the walls during their flight time. Therefore by changing the duration and timing of the voltage pulse on the potential switch, a range of masses is effectively selected.

After exiting the potential switch, anions separate further until the end of the flight tube where they are detected using a multichannel plate (MCP) detector[Fig.2.1(8)]. The signal from the MCP is monitored using a digital oscilloscope and the data converted from a time of flight domain to a mass per charge (m/z) domain spectrum by calibrating against known masses. An example of a mass spectrum is shown in Figure 2.3 containing I^- and $I^- \cdot (H_2O)_n$ (n=1-4). For the the narrowest peak in the displayed spectrum ($I^- \cdot (H_2O)_2$ at ∼163 amu) the resolution, $^m/_{\Delta m}$ is ∼ 300, which is sufficient to separate ions differing by a unit m/z. Focusing with the einzel lenses and fine tuning the timing, extraction and deflector potentials will optimize a different peak. For example, the spread in arrival time of I^- can easily be made narrower by optimizing the above settings.
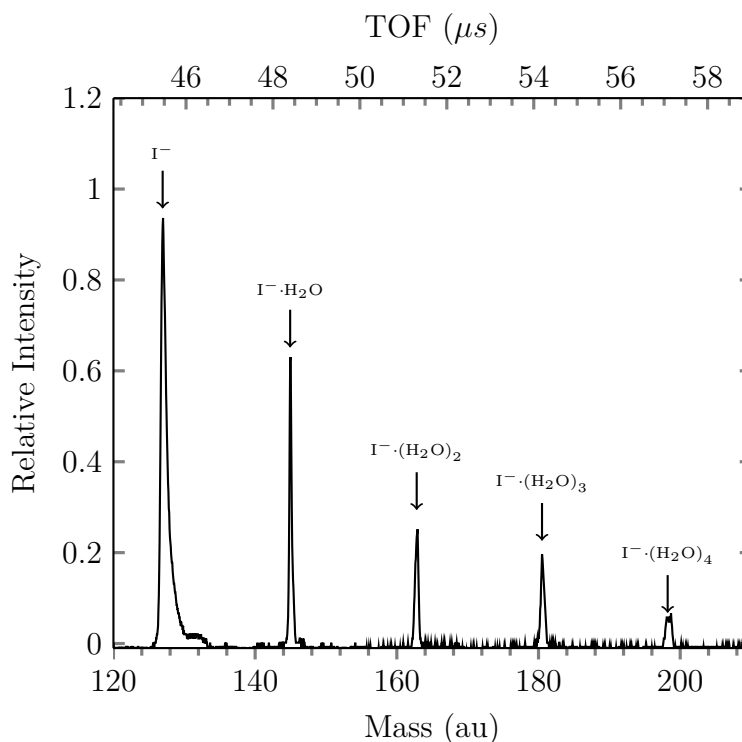
Figure 2.3: An example of a mass spectrum showing I^- and a progression of up to 4 water molecules around I^-.

2.3 Laser system and velocity map imaging

2.3.1 Nanosecond laser system

Based on the anion signal obtained from the MCP, an anion of interest can be selected and interrogated using a laser. This is done simply by adjusting the laser pulse to coincide with the anion packet at the interaction region (Figure 2.4). For all the experiments reported in this dissertation, linearly polarized nanosecond laser pulses were used. A dye laser (Cobra Stretch Pulsed Dye Laser, Sirah Laser- und Plasmatechnik GmbH) was used for the photodetachment experiments in Chapters 3-5. The dye laser is pumped by either 532 nm or 355 nm output from a Neodymium Yttrium Aluminum Garnet laser(Quanta Ray-INDI-40, Spectra Physics Inc.) operating at 10 Hz. By utilizing different dyes a range of wavelengths (450 nm-750 nm) can be obtained. Shorter wavelengths are further obtained by second harmonic generation of the above wavelength range using a beta barium borate (BBO) crystal. Therefore, utilizing the dye laser affords us very wide wavelength tunability, effectively covering the whole visible spectrum and a significant portion of the near ultraviolet. The doubling crystal results in pulses of 4-13 mJ of pulse energy with >98% polarization. Usually the laser beam is mildly focused using a 1 m lens resulting in power densities of about 10^8 Wcm^{-2}.
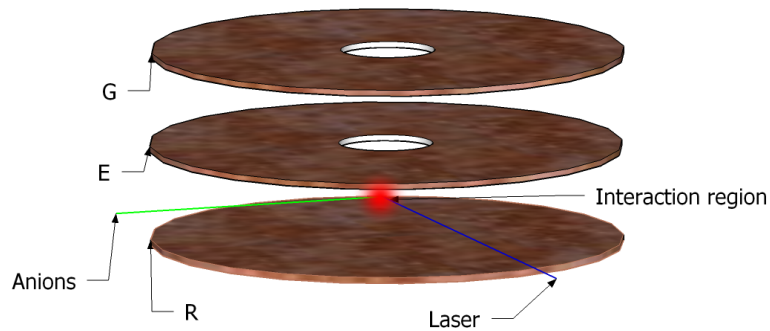
Figure 2.4: Interaction region for the anion beam and the laser (Region 7 of Figure 2.1). The anions and the laser beam interact approximately midway between the repeller (R) and extractor (E) electrodes. Electrode G is held at ground

In addition to using the dye laser for certain wavelengths, for the work discussed in Chapter 6, the fundamental and the harmonics of the YAG laser were used. The YAG laser is a solid state, Q-switched laser based on Neodynium crystal doped with Yittrium Aluminium Garnet and pumped by a flash lamp. The laser outputs 1064 nm wavelength pulses of 5-8 ns duration with a pulse energy of 450 mJ at 10 Hz, which presents a limiting rate for the experiment. The second harmonic (532 nm) of the above wavelength is obtained by utilizing the fundamental output (1064 nm) and a potassium dideuterium phosphate (KDP) non-linear crystal under phase matching conditions. Combining 532 nm and the residual 1064 nm under frequency mixing conditions on the KDP crystal generates a third harmonic (355 nm). Depending on the experiment, any of these three wavelengths can be used.

2.3.2   Velocity map imaging

Photoelectron spectroscopic methods have traditionally been based on TOF methods or magnetic bottle analyzers for separation of the electrons by their kinetic energy. To extract angular distributions one has to change the laser polarization angle or detect the electrons at different angles and thus measurement of PADs this way is time consuming and inconvenient for routine measurements of the PAD. A more efficient way to measure PADs and extract photoelectron spectra simultaneously with near 100% collection efficiency is velocity map imaging (VMI), introduced by Eppink and Parker[69]. Photofragment imaging in general was invented by Chandler and Houston[89]. In photoelectron VMI, electrons with the same initial velocity are focused onto the same point on the two dimensional (2D) detector. A charge-coupled-device (CCD) camera is then used to capture individual impacts on the detector. The result is an image from which fragment velocities (speed and direction) can be extracted, provided proper symmetry is imposed on the photoelectron distribution. Our design, illustrated in Figures 2.5 and 2.4, is a slight modification of that of Eppink and Parker[69]. In this case both the repeller (R) and extractor (E) electrodes are negatively biased against ground. The third electrode (G) is held at ground. The three electrodes are $1''$ apart. For electrons with kinetic energies of ~ 1 eV a repeller voltage of -1000 V and extractor voltage of $\approx$ -680 V to -730 V results in a reasonable flight time for electrons to cover more than 50% of the detector radius. The extractor
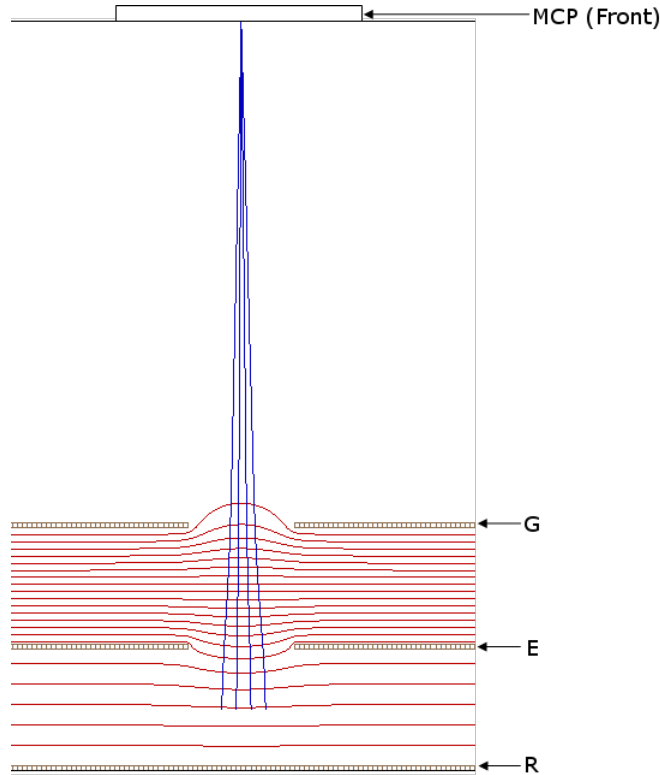
Figure 2.5: An illustration of VMI using four electrons with the same velocity vector but originating at different places. The electrons end up at the same place on the detector. For this SIMION[88] simulation, the repeller (R) and extractor (E) copper electrodes were held at -1000 V and -726 V respectively. Electrode G is held at ground and so is the front MCP. The resulting electric field contour lines are also shown.

and repeller voltages can be adjusted to spread out the transitions over a wider or smaller area of the detector but the ratio of the voltages (V_E/V_R) is always ≈ 0.7 to satisfy the velocity mapping condition. The laser pulse and anion packet interact approximately midway between the extractor and repeller. The electric field polarization direction of the laser lies along the anion flight axis. The resulting photoelectron cloud (see illustration in Figure 2.6) is repelled towards the detector (along the Z-axis in Figure 2.6) through a $1''$ hole in the extractor and ground electrodes. Immediately after photodetachment electrons initially moving in the -Z($\downarrow$) direction will experience a large potential gradient and accelerate faster than those those initially moving in the +Z($\uparrow$) direction. The result is that the intially "spherical cloud" becomes more like an "oblate spheroid" with the radii x = y > z. This will be maintained as soon

as the electrons enter into the fiels free region past electrode G. Electrons then move along a 14 cm μ-metal shielded electron TOF tube. The photoelectron cloud expands from the center in all directions as it moves towards the detector. If the electrons have different kinetic energies, a 3D electron distribution can be imagined as a series of nested oblate spheroids.
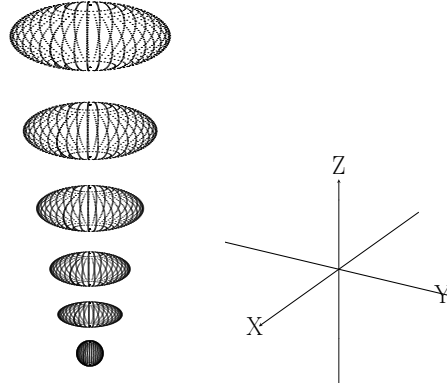
Figure 2.6: An illustration of the "photoelectron cloud". The electrons are propagating towards the MCP positioned parallel to the XY plane, that is perpendicular to the +Z-axis.

At the end of the electron TOF tube, electrons impact upon an imaging quality chevron type 40 mm diameter MCP detector (Photonis USA, Inc., APD 3040 FM) with 10 μm diameter pores and a P20 phosphor screen[Fig.2.1(10)]. Electron impacts on the front of the MCP are translated onto the same position on the phosphor and hence the detector is position sensitive. To discriminate against background noise, the potential difference across the MCP is kept too low to detect any particles except within a narrow time window coinciding with photoelectron arrival. This is done using a fast acting high voltage pulse generator (Directed Energy Inc., PVM 4150). The events on the phosphor screen are captured cycle by cycle using a 640X480 pixel CCD camera (Imperx, Inc, IPX-VGA 120-L)[Fig.2.1(11)] at a repetition rate of 10 frames per second, i.e equivalent to the 10 Hz repetition rate of the experiment. The frames are transmitted to a computer and summed up in real time to make an image. The number of frames required to make an image usually depends on a combination of factors such as the number of ions in the interaction volume, laser power and the anion photodetachment cross section. An equivalent number of frames with the laser delayed relative to the anion packet is subtracted from the image in order to remove

background noise. Beside the dark noise associated with the camera, other sources of noise are gaseous molecules within the chamber and electrons from the ionization of metal surfaces by scattered light. Maintaining low pressure in the detection region $\sim 8 \times 10^{-9}$ Torr significantly reduces the density of background gaseous molecules. Noise due to ionization of metal surfaces is the most difficult to deal with especially at photon energies >4 eV (wavelengths less than 300 nm) but can be reduced by using a well collimated laser beam.

2.4   Data treatment and analysis

A raw image of I$^-$ detachment obtained at 267 nm is shown in Figure 2.7A. The image is a projection of a 3D photoelectron distribution onto the 2D detector plane. The distance from the center of the two rings on the image is proportional to the speed of the photoelectron in the plane of the detector. At 267 nm, photodetachment from I$^-$ can result in an I atom in its ground state I(^{2}P$_{3/2}$) or excited spin-orbit state I(^{2}P$_{1/2}$). Thus the inner and outer rings in the image correspond to transitions that result in production of I(^{2}P$_{1/2}$) and I(^{2}P$_{3/2}$) spin orbit states respectively. The intensity profile from the center of the image (Figure 2.7B) shows that the image features are broad and asymmetrical. This smearing of the photoelectrons occurs because only the in-plane velocity component is recorded. All information along the electron flight tube axis is lost.

In principle it is possible to avoid such smearing by detecting only the photoelectrons at the center of the 3D distribution as illustrated in Figure 2.8. This approach, called slice imaging, has been applied to ion detection[90–93]. Ideally in slice imaging, the goal is to make the slice as thin as possible for better resolution. Because electrons move much faster than ions slice imaging is not practical for electrons. Consider for example a cloud of electrons moving towards a detector as shown in Figure 2.8. Points A and B represent electrons closest to and furthest from the MCP surface respectively. Let us assume that the diameter of the sphere (the distance between A and B) is 20 mm which is 50% of the MCP diameter. From the basic time of flight equation the time needed for electrons at B to traverse distance d (20 mm) to the
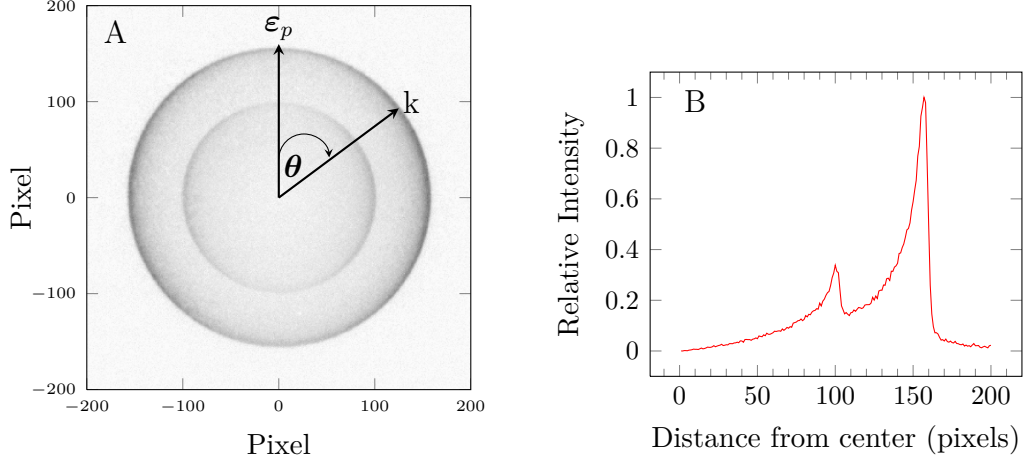
Figure 2.7: Raw photoelectron image(A) of I⁻. The intensity profile (B) from the center of the image shows asymmetric nature of the peaks in raw images.
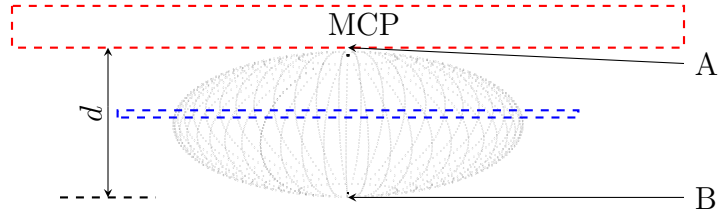
Figure 2.8: Slice Imaging of particles. Only particles in the region bounded by the blue rectangle are detected. Thinner slices are desirable for better resolution.

detector is;

$$t = \frac{d}{\sqrt{2U}}\sqrt{\frac{m}{q}} \qquad (2.4)$$

U is the ion/electron extraction potential difference, q is electron charge (1.602×10^{-19} C) and m is mass of the electron (9.11×10^{-31} kg). For a voltage of 1000 V, and distance of 20 mm, $t = 1.6$ ns. This is just the time gate required to detect all the photoelectrons between points A and B. To slice 2 mm of the sphere of photoelectrons, 0.16 ns time gate will be required! For similar settings to slice a sphere of Cl⁻ atoms a time gate of $\sim$ 30 ns is required which is achievable with moderately fast electronics[90]. Faster electronics are therefore required to apply slice imaging to the detection of photoelectrons and hence electron slice imaging is yet to be realized.

25

Instead of slice imaging, all the photoelectrons are detected. Advantage is taken of the cylindrical symmetry imposed on the photoelectron distribution by the linearly polarized photons. Mathematically, the projection $P(x, y)$ of a cylindrically symmetric distribution onto a 2D plane is an Abel transform of the distribution[94].

$$P(x, y) = 2 \int_{|x|}^{\infty} \frac{I(r, y) dr}{\sqrt{r^2 - x^2}} \tag{2.5}$$

The inverse function which gives a slice through the center, $I(r, y)$, is[94]

$$I(r, y) = -\frac{1}{\pi} \int_r^{\infty} \frac{dP}{dx} \frac{dx}{\sqrt{x^2 - r^2}} \tag{2.6}$$

The singularity at $x = r$ in (2.6) for photoelectron images introduces difficulties with direct use of this equation. The basis set expansion (Basex) method of Dribinski *et al*[95] addresses this problem by expanding $P(x, y)$ in a basis set of functions that are analytical projections of well behaved gaussian like functions. Their program BASEX was used for reconstruction of the raw images. Alternative methods include the Hansen and Law algorithm[96], Vrakking's iterative method[97] and the onion-peeling algorithm[98].

The effect of the image reconstruction is demonstrated in Figure 2.9 for the I$^-$ image shown previously. The peaks are visibly narrower after reconstruction as can be seen also by comparing the intensity profiles across each image (Figure 2.9, C and D).

2.4.1 Photoelectron spectrum

The photoelectron velocity spectrum, *I(v)*, is obtained by integrating over all angles at given radius from the image center. The photoelectron kinetic energy spectrum, *I(eKE)*, is obtained from *I(v)* by calibrating the detector with a known anion under the same velocity mapping focusing conditions (voltages on the repeller and extractor electrodes). To account for proper scaling of the intensity due to the change of variable, $I(v) \rightarrow I(eKE)$, a Jacobian transformation is applied giving,
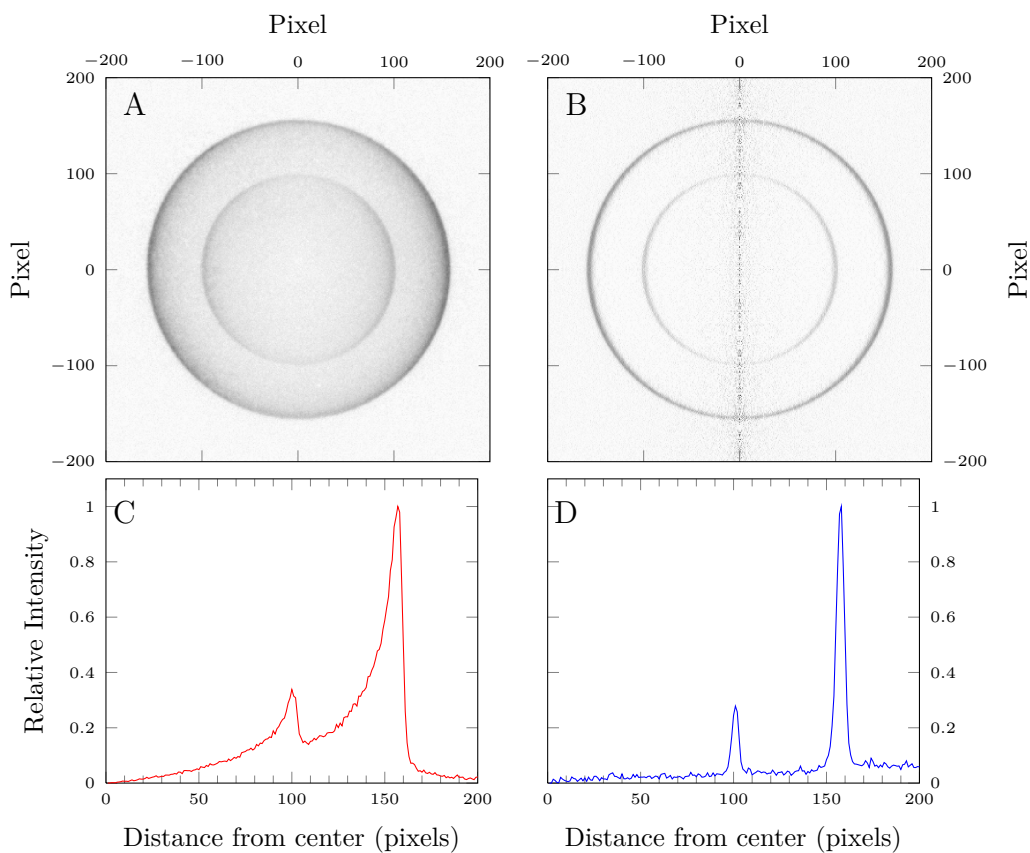
Figure 2.9: Raw photoelectron image of I⁻ (A) and the corresponding BASEX reconstructed image (B). The transitions are narrower for the reconstructed image.
The intensity profiles from the center of the images are shown below the images.

$$I(eKE) = \frac{I(v)}{v} \tag{2.7}$$

Sometimes it is convenient to use the electron binding energy (*eBE*) rather than
eKE because the *eBE* is independent of the photon energy for direct processes. By
conservation of energy, these are related by;

$$eBE = h\nu - eKE \tag{2.8}$$

where $h\nu$ is the photon energy. The photoelectron spectrum of I⁻ at 267 nm is shown
in Figure 2.10
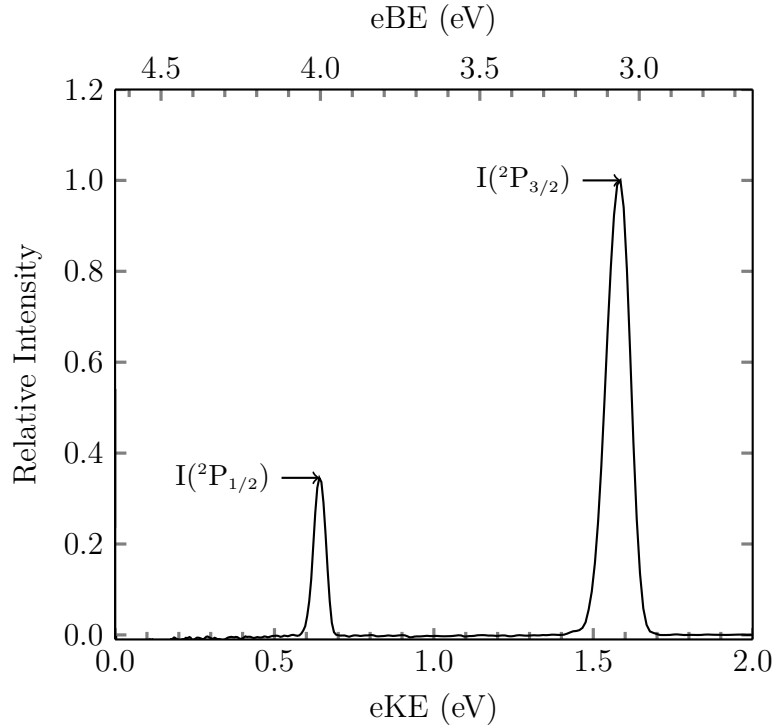
Figure 2.10: Photoelectron spectrum of I$^-$ at 267 nm obtained from the reconstructed image of Figure 2.9

2.4.2 Photoelectron angular distributions

As is apparent from Figures 2.7 and 2.9, the photoelectron intensity distributions in the I$^-$ photodetachment images are anisotropic. Defining θ as the angle between the photoelectron momentum and the direction of the electric field of the laser (see Figure 2.7), the differential cross section, $I(\theta)$ in arbitrary units, for a given transition is calculated by integrating across the full width at half maximum (FWHM) of the transition for every angle.

As mentioned in the introduction, the asymmetry parameter β is related to $I(\theta)$ by;

$$I(\theta) = \frac{\sigma}{4\pi}\left[1 + \beta P_2\left(\cos\theta\right)\right] \tag{2.9}$$

For the two I$^-$ transitions of Figures 2.7 and 2.9, $I(\theta)$ is shown in Figure 2.11. For a one photon process using a linearly polarized laser, such as was used for the I$^-$ images above, $I(\theta)$ may be fit to equation (2.9) to extract the anisotropy parameter.

In the case of $I(^2P_{3/2})$ and $I(^2P_{1/2})$ transitions from I^- at 267 nm the extracted β values depend on nature of the transition an the electronic kinetic energy. Values of $\beta_{3/2}$ and $\beta_{1/2}$ are -0.46 and -0.69 respectively.

2.4.3   Comment on the reported values of β

A number of factors can affect the value of β extracted from a photolelectron image. In theory, our photoelectron images should be circular and four-way symmetric, but in practice imperfections in the experiment and the quantum nature of the electron will lead to deviation from this behavior. Careful alignment of the laser beam, imaging electrodes, MCP and CCD camera will minimize distortions. In order to ensure that these effects are negligible in terms of extracted PADs, analysis may be performed in two ways to check for consistency. In the first case, the image can be four-way symmetrized mathematically after a careful choice of the center and the PAD extracted from the symmetrized image. In this case, a set of images can be analyzed and the standard deviation determined from this set. The second method, which is appropriate for a strong photoelectron signal, is to extract the PAD for each quadrant without without applying any symmetrization. The standard deviation can then be extracted from the β values from the four quadrants. In this dissertation most of the reported values of β were obtained using the four-way symmetrization method.
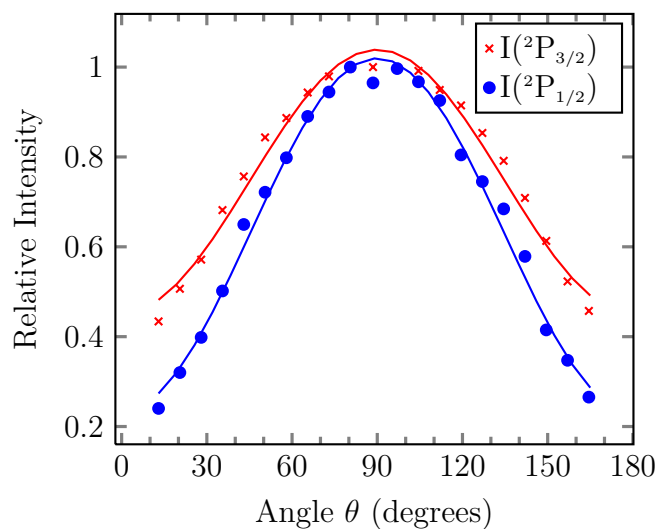
Figure 2.11: Differential cross section for photodetachment from I$^-$ at 267 nm for the first two spin-orbit states of iodine. The lines are fits of the data to equation (2.9) using β = -0.46 and -0.69 for transitions leading to I(^{2}P$_{3/2}$) and I(^{2}P$_{1/2}$) respectively.

Chapter 3

Direct and indirect detachment in I$^-\cdot$Y (Y = C$_4$H$_5$N, CO$_2$): The role of dipole-bound and neutral cluster states

3.1   Introduction

The photodetachment of atomic halides (I$^-$, Br$^-$, Cl$^-$ and F$^-$) in the near ultraviolet region of the electromagnetic spectrum is generally characterised by two bands corresponding to the two spin-orbit states of the halogen (^{2}P$_{3/2}$ and ^{2}P$_{1/2}$). This can be schematically represented as;

$$X^- \xrightarrow{\ h\nu\ } X\left(^2P_{3/2,1/2}\right) + e^- \tag{3.1}$$
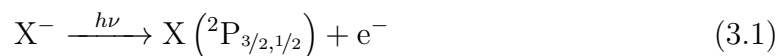
In the case of I$^-$, the minimum energy required to detach an electron is 3.059 eV[99]. Since there are no rotational or vibrational states, this energy represents the electron affinity of I$^-$. Thus photoelectron spectroscopy of atomic anions is useful in determination of electron affinities. The spin-orbit splitting between I(^{2}P$_{3/2}$) and I(^{2}P$_{1/2}$) is 0.943 eV[100]. A number of experiments have shown that the photoelectron spectra of solvated atomic halides have two characteristic bands separated by the spin-orbit splitting of the halogen[30, 101–103]. Thus these spectra resemble those of free halides

except that the minimum energy required to detached an electron increases. The bands in the $X^-\cdot Y$(X=Cl, Br, or I and Y = solvent molecule) spectra are therefore due to transitions correlating asymptotically to the production of $[X(^2P_{3/2}) + Y + e^-]$ and $[X(^2P_{1/2}) + Y + e^-]$ respectively;

$$X^-\cdot Y \longrightarrow X(^2P_{3/2}) + Y + e^- \tag{3.2}$$

$$X^-\cdot Y \longrightarrow X(^2P_{1/2}) + Y + e^- \tag{3.3}$$
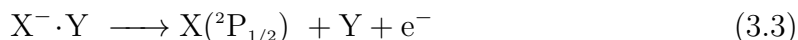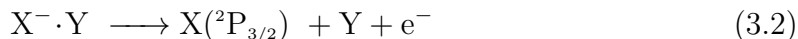
(3.2) will referred to as Channel I and (3.3) as Channel II. The shift in Channel I and Channel II thresholds is a result of stronger solvent stabilization of the atomic halide relative to the neutral halogen atom as illustrated in Figure 3.1. The magnitude of the shift, ΔE, is solvent dependent[102, 103].

An important difference between X^- and $X^-\cdot Y$ photodetachment is the possibility of vibrational and rotational excitation. Vibrational excitation in $X^-\cdot Y$ and $X\cdot Y$ clusters usually involves the low frequency van der Waals modes[104]. In some cases, however, the interaction of X^- with Y may lead to distortions of the geometry of Y. In such a case, a vibrational mode corresponding to motions that lead to the distortion will be active in $X\cdot Y$. In most cases, this occurrence is due to the loss of charge upon photodetachment which weakens the bonding between X and Y. For example, such vibrational excitations have been reported for $X^-\cdot CO_2$ photodetachment[21, 105]. Other sources of vibrational excitations are possible. The vibrational excitations observed in photodetachment of $X^-\cdot MeX$ (MeX=CH_3Cl, CH_3Br and CH_3I) have been attributed to non-adiabatic effects and not solely due to perturbations of MeX by X^-[42, 106, 107].

The dipole moment of pyrrole (point group C_{2v}) is 1.77 D[108] while carbon dioxide, a linear molecule, has no net dipole moment. The interaction of the pyrrole molecule with anions is particularly interesting, since these molecules are important subunits of the anion receptor molecules (calix[n]pyrroles) that form the basis of many colorimetric anion specific sensors[109–112]. In this Chapter, photodetachment from $I^-\cdot C_4H_5N$(C_4H_5N = pyrrole) and $I^-\cdot CO_2$ which present very different cluster environments is studied. The photoelectron spectra of these cluster anions are compared with those of I^- photodetachment. In both cases structure is observed in the detachment channels I and II mentioned above which was shown to be due to different effects in each cluster anion. An autodetachment signal is also observed in $I^-\cdot C_4H_5N$ over an
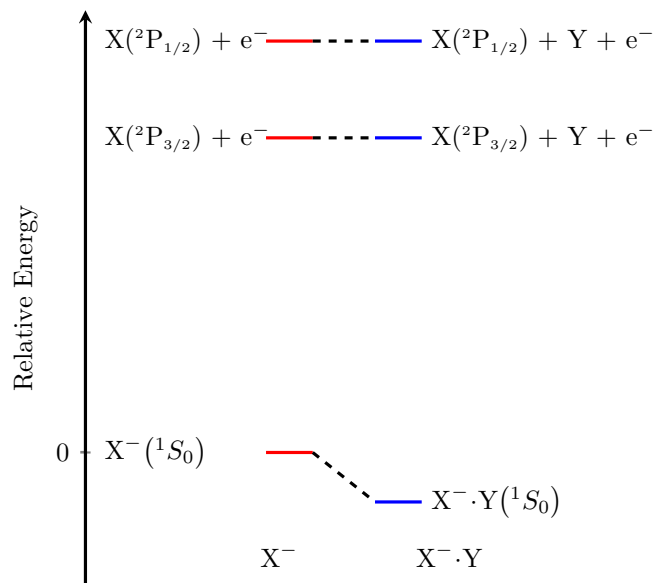
Figure 3.1: Energy level diagram for an atomic halide and halogen ^2P spin-orbit states. The energy levels on the right are those for the solvated halide as well as the asymptotic states after photodetachment

unexpectedly wide range of energies near the Channel I threshold. In both cluster anions the photoelectron angular distributions show significant deviations from those of I^- for specific narrow energy ranges. These results are discussed in terms of the solvent distortion due to interaction with I, the effect of the solvent molecule on iodine electronic structure and the role of the cluster dipole moment in photodetachment.

3.2   Experimental

Details of the velocity mapped photoelectron imaging spectrometer were presented in Chapter 2. Here only details specific to $I^- \cdot C_4H_5N$ and $I^- \cdot CO_2$ production will be presented. $I^- \cdot C_4H_5N$ was produced by electron impact upon supersonic expansion. A mixture of argon (~ 400 psig) and methyl iodide (ambient pressure) was bubbled through pyrrole at 10-20 psig stagnation pressures. For $I^- \cdot CO_2$, the discharge source was used. 200 psig gaseous CO_2 is premixed with 400 psig Ar and methyl iodide at ambient pressure and the mixture is then expanded at 30-80 psig stagnation pressure into the source chamber.

Photodetachment at different wavelengths was achieved through use of a number of laser dyes; DCM, pyrromethene 597, pyrromethene 580, coumarin 307 and coumarin 153. For each of the anions mentioned above, photoelectron images were collected at small energy intervals (<0.02 eV to 0.1 eV). Photoelectron spectra and angular distributions were extracted at each wavelength according to the methods described in Chapter 2.

To obtain further insight into the structure and dynamics of these anions, *ab initio* calculations were performed using the Q-CHEM[113] and Gaussian 03[114] suites of programs. Specifically, possible conformers of $I^-\cdot C_4H_5N$ and $[I\cdot C_4H_5N]$ were determined as well as the vertical detachment energies for the anionic conformers. The aug-cc-pvdz basis set was used for atoms H, C and N[115]. For I, the CRENBL pseudopotential and basis set of LaJohn et al[116], as modified by Combariza[117] to reproduce the experimental electron affinity of I^- was used. Q-CHEM calculations were implemented through the University of Southern California's Center for Computational Studies of Electronic Structure and Spectroscopy of Open-Shell and Electronically Excited States.

3.3 Results

3.3.1 Photoelectron spectra

A number of photoelectron images were collected between 300-260 nm at 1-5 nm intervals for both $I^-\cdot C_4H_5N$ and $I^-\cdot CO_2$. Radial and angular distributions were extracted from the BASEX[95] transformed images as described in Chapter 2. Selected photoelectron images and spectra for $I^-\cdot C_4H_5N$ and $I^-\cdot CO_2$ are shown in Figures 3.2 and 3.3. The photoelectron image and spectrum of I^- at 300 nm is also shown in Figure 3.2 for comparison. The two transitions in I^- photodetachment ($I(^2P_{3/2})$ and $I(^2P_{1/2})$) are labeled in the spectrum. The outer and inner dark rings correspond to the $I(^2P_{3/2})$ and $I(^2P_{1/2})$ transitions respectively. Photoelectron spectra for the $I^-\cdot Y$ clusters were calibrated against the I^- transitions. At sufficiently short wavelengths, the spectra of $I^-\cdot CO_2$ and $I^-\cdot C_4H_5N$ also show two bands labeled I and II which are shifted to higher binding energies relative to I^- transitions. $I^-\cdot C_4H_5N$ and $I^-\cdot CO_2$

transitions are shifted by 0.66 eV and 0.18 eV respectively. The splitting between band I and II in both clusters is close to the spin-orbit splitting of the I(^{2}P) state.
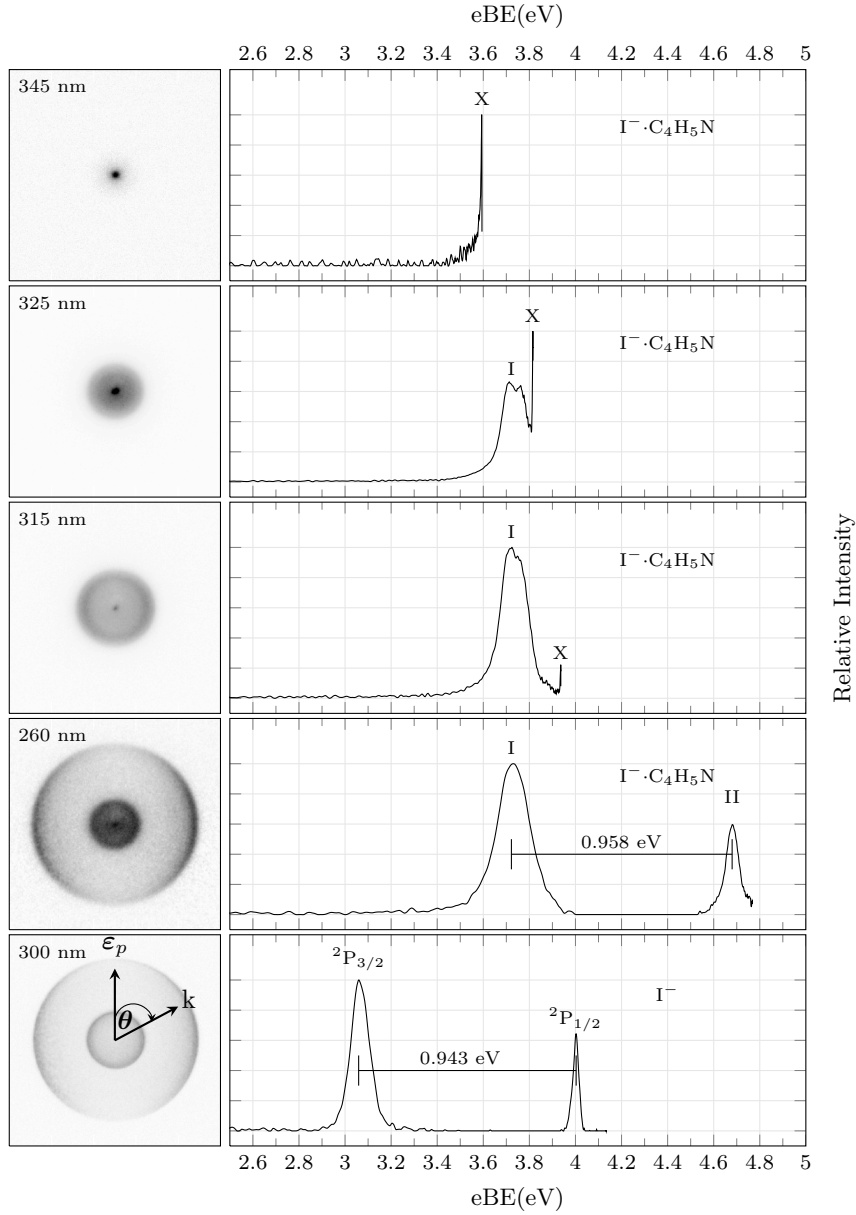
Figure 3.2: Photoelectron images and spectra of I$^-$·C$_4$H$_5$N and I$^-$ at different wavelengths. In all images the direction of the laser polarization is as indicated on the I$^-$ image.
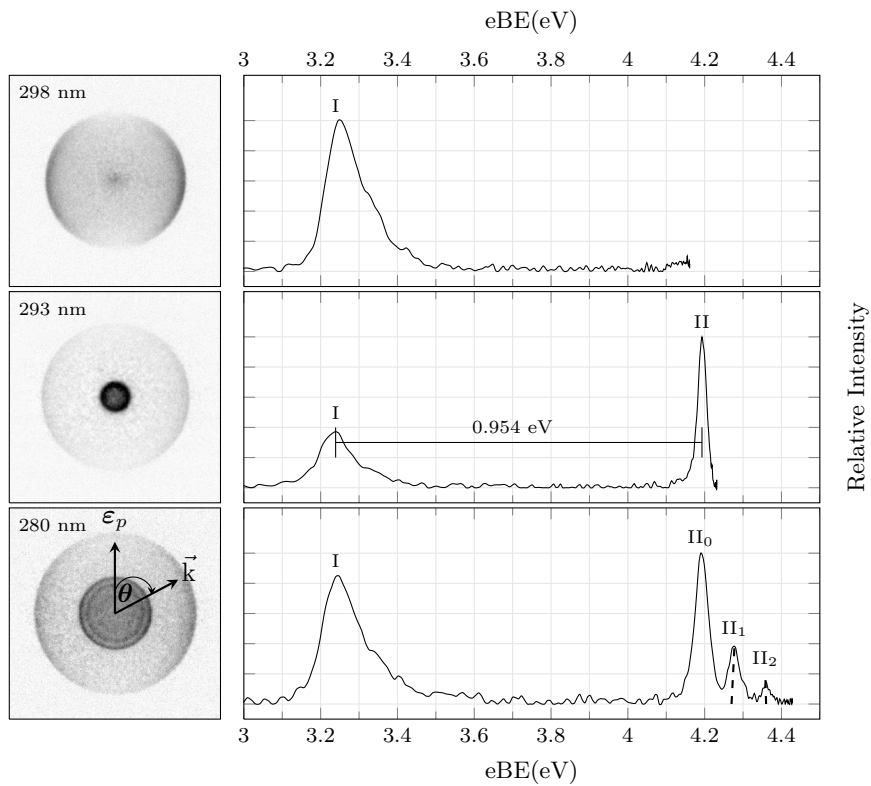
Figure 3.3: Photoelectron images and spectra of $I^- \cdot CO_2$ at different wavelengths. In all images the direction of the laser polarization is as indicated on the $I^- \cdot CO_2$ image at 280 nm.
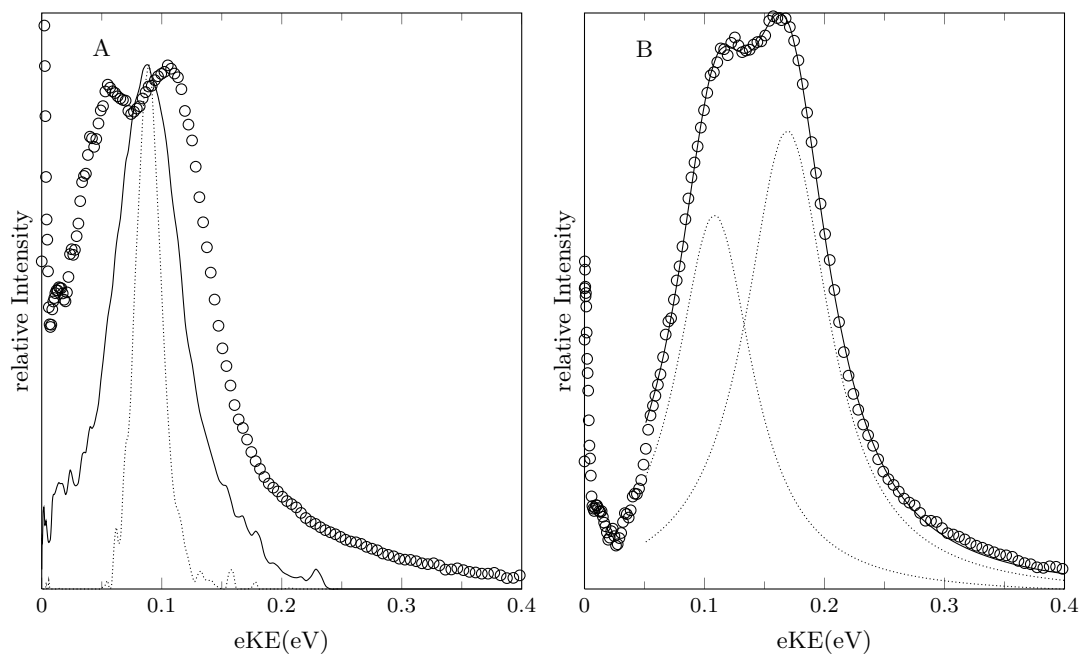
Figure 3.4: (A) Comparison of the photoelectron spectra of $I^- \cdot C_4H_5N$ at 325 nm (open cirles), peak II of $I^- \cdot C_4H_5N$ at 260 nm (solid line) and $I(^2P_{3/2})$ transition of I^- at 303 nm. (B) Photoelectron spectrum, *I(eKE)* for $I^- \cdot C_4H_5N$ at 320 nm showing the splitting of Channel I peak. The open circles are experimental data and the dotted lines are Lorentzian fits to the two peaks. The solid line is a convolution of the two Lorentzian fits.

Examining $I^- \cdot CO_2$ and $I^- \cdot C_4H_5N$ photoelectron spectra in detail reveals more differences between these spectra and the I^- photoelectron spectrum at 300 nm. The photoelectron spectrum of $I^- \cdot CO_2$ at 280 nm shows some structure in the Channel II band, with two additional peaks to the higher binding energy side of the band II origin. The three peaks labeled II_0, II_1 and II_2 are separated by 85 meV.

Figure 3.4A demonstrates that for $I^- \cdot C_4H_5N$, Channel I transitions are consistently broader than Channel II transitions at the same eKE. Comparison of the width of these peaks is only valid at the same eKE because the resolution of the imaging detector diminishes with increasing eKE. To illustrate this point, consider the photoelectron spectrum of I^- at 300 nm in Figure 3.2. The measured FWHM the $I(^2P_{3/2})$ transition (eKE = 1.074 eV) is 85 meV while that $I(^2P_{1/2})$ transition (eKE = 0.131 eV) is 23 meV.

Applying this caveat, $I^- C_4H_5N$ spectra at 325, 320 and 315 nm (Figures 3.2 and 3.4B) show that peak I is actually a convolution of two partially resolved peaks separated by 60 meV. Due to diminished detector resolution at high eKE, the spectrum at 260 nm in Figure 3.2 does not resolve this splitting.

In addition to the two aforementioned bands, the images and spectra of $I^- \cdot C_4H_5N$ show a third low electron kinetic energy feature with an electron binding energy which depends on the detachment photon energy. This feature is present in all $I^- \cdot C_4H_5N$ images recorded between 360 and 310 nm and reappears at 270 nm. The relative amount of these slow electrons (with respect to the Channel I and Channel II bands) varies across the wavelength range, but it is stronger near Channel I threshold. The threshold energy for appearance of these electrons is 3.45 eV (360 nm) which is considerably lower than the observed Channel II direct detachment vertical detachment energy (3.72 eV).

3.3.2   Photoelectron angular distributions

In all the photoelectron images of Figures 3.2 and 3.3 the intensity distributions (especially the outer rings corresponding to $I(^2P_{3/2})$ transition in I^- and Channel I transitions in $I^- \cdot CO_2$ and $I^- \cdot C_4H_5N$) are anisotropic. The angular distributions, $I(\theta)$, were fit to the equation $I(\theta) = \frac{\sigma}{4\pi}\left[1 + \beta P_2(\cos\theta)\right]$ in order to extract the anisotropy

parameter β in accordance with the method in Chapter 2. Attention is focused on the outer ring (the $I(^2P_{3/2})$ or Channel I transition) as this presents the most data points for comparison. For I^- these β values will be referred to as $\beta_{3/2}$ here and for the remainder of the dissertation. Similarly the β value reported for $I^-\cdot CO_2$ and $I^-\cdot C_4H_5N$ will be referred to as β_I. $\beta_{3/2}$(eKE) for I^- and β_I(eKE) for $I^-\cdot CO_2$ and $I^-\cdot C_4H_5N$ are shown in Figure 3.5. Each data point represents the $\beta_{3/2}$ or β_I value averaged over the FWHM of the transition (centered at the given electron kinetic energy of electrons produced in the channel). Each point arises from a different detachment wavelength. In all three cases β is seen to depend on the eKE. For I^-, at low eKE $\beta_{3/2}$ is nearly zero but gradually becomes more negative (representing a distribution which is more preferentially polarized perpendicular to the laser electric vector) as eKE increases until it reaches a minimum at eKE=0.915 eV($\beta_{3/2}$=-0.93) and thereafter continues to more positive values.

In the case of $I^-\cdot CO_2$ and $I^-\cdot C_4H_5N$, far from the Channel II threshold, β_I is similar to $\beta_{3/2}(I^-)$ at the same eKE. However, a few meV below the Channel II threshold, β_I for both clusters increases until a maximum is reached and then falls back approximately to the I^- trend. The maximum β_I, (β_{Imax}), value for $I^-\cdot C_4H_5N$ in this region is ~-0.2 while for $I\cdot CO_2$ this value is ~-0.7.
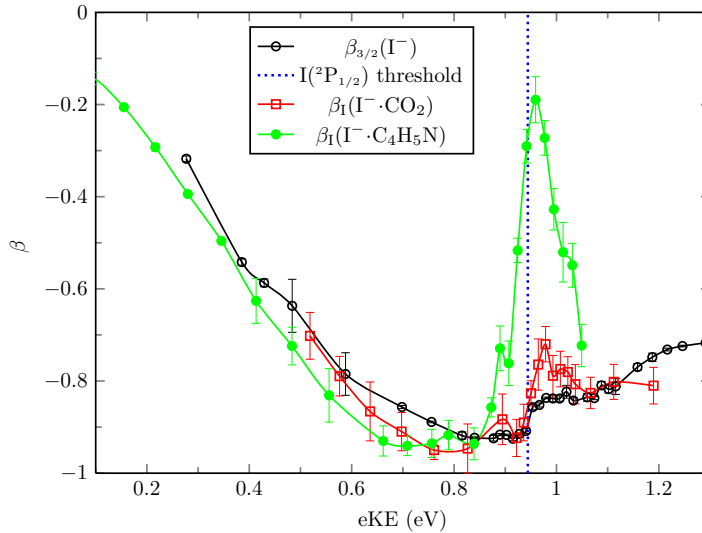
Figure 3.5: β(eKE) evolution for I^-(open circles), $I^-\cdot CO_2$(diamonds) and $I^-\cdot C_4H_5N$(closed circles). Solid lines are extended through the points as a guide to the eye. The dotted vertical line corresponds to $I(^2P_{1/2})$ channel opening in I^-.

3.3.3 *Ab initio* calculations

$I^-\cdot Y$ cluster anions often have a number of conformers because of the different ways in which I^- could interact with Y. In order to check for this possibility in $I^-\cdot C_4H_5N$ geometry optimizations were performed by initially placing the iodine atom at different positions with respect to the C_4H_5N molecule's orientation as shown in Figure 3.6. Only two conformers, A1 and A2 in Figure 3.6, were found. These lie 0.65 eV apart with the more stable conformer of $I^-\cdot C_4H_5N$ (A1) retaining the C_{2v} symmetry of the pyrrole subunit with a collinear N–$H\cdots I$ segment. The $H\cdots I$ distance is 2.465 Å and there is very little perturbation of the pyrrole moiety. In this conformer the N–H bond experiences the largest change upon cluster anion formation, a difference of 0.025 Å or an elongation of just 2.5%. Conformer A2 has the I atom on the opposite side of the pyrrole unit, and it is argued later that there is no evidence of this conformer contributing to our photodetachment images.

  A similar approach for the open shell $I\cdot C_4H_5N$ resulted in four conformers also shown in Figure 3.6. The energies of these conformers relative to the anion A1 are also shown. The global minimum corresponds to structure N1, in which the I atom is located above the plane of the pyrrole ring (but not directly above the C_2 axis) and toward the opposite end of the molecule to the N atom. In conformer N2, the iodine is displaced from the C_2 axis of pyrrole resulting in a 140° N–$H\cdots I$ angle. The third neutral conformer (N3) is nearly isoenergetic with N2 and corresponds to a structure similar to that of the cluster anion A1 conformer. The I atom again lies along the C_2 axis, but at a greater distance than in the cluster anion (2.815 Å). Neutral conformer N4 has a structure similar to that of the anion A2 conformer. The dipole moments associated with each neutral conformer are $\mu_1 = 3.45$ D, $\mu_2 = 2.37$ D, $\mu_3 = 2.58$ D, and $\mu_4 = 1.89$ D. Vibrational frequencies for each of the conformers were calculated to verify that the structures correspond to true stable conformers (as opposed to transition states). For each conformer in Figure 3.6, the vibrational frequencies associated with all 27 modes are real which verifies that these structures represent minima. As shown in the Franck-Condon calculations presented later, the van der Waals modes (ν_1, ν_2 and ν_3) are of greatest relevance. In particular, the ν_3 mode (of A1 and N3) corresponds to motion along the $(N)H\cdots I$ direction while mode ν_2 leads to displacement of the I atom from the plane containing the pyrrole moiety.
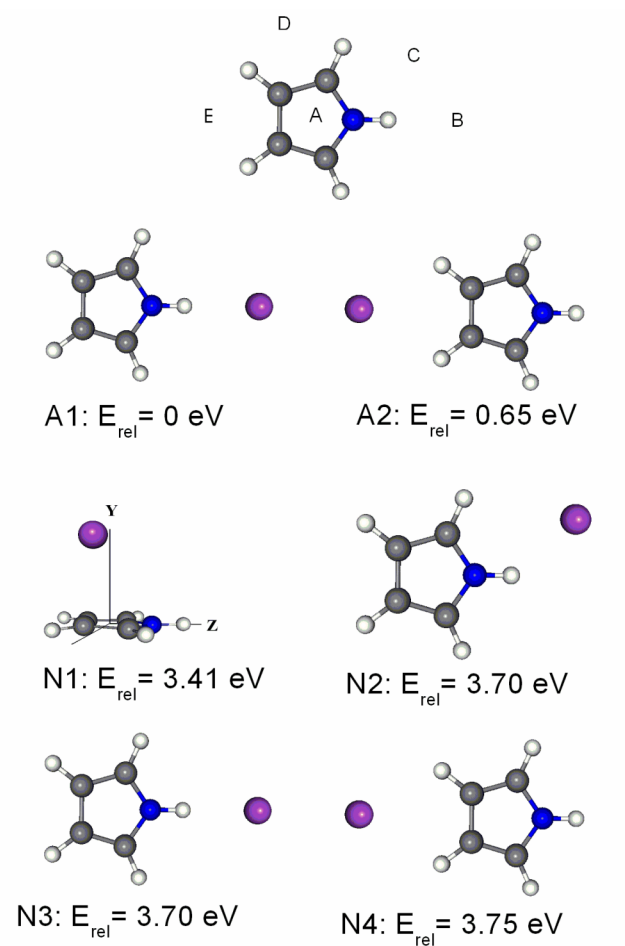
Figure 3.6: Neutral (N1-N4) and cluster anions (A1-A2) MP2 optimized *ab initio* geometries. Approximate starting points for neutral and cluster anion optimization are indicated as A-E (A lies above the plane of the pyrrole moiety). E_{rel} is the conformer energy relative to A1.

41

3.4 Discussion

The results presented above reveal some similarities and differences between I^- an $I^- \cdot Y$ photodetachment. The eKEs of the two bands labeled I and II in both cluster anions increase linearly with photon energy. These are the direct detachment channels described schematically by Equations 3.2 and 3.3 respectively which are analogous to the $I(^2P_{3/2})$ and $I(^2P_{1/2})$ transitions of free I^-. The main difference lies in the shifting of the $I^- \cdot Y$ spectra to higher binding energy which is solvent dependent. At low eKEs, a situation for which the resolution of the detector is better, some structure is noticeable in band I of $I^- \cdot C_4H_5N$ and band II of $I^- \cdot CO_2$. For $I^- \cdot C_4H_5N$ there is evidence of an indirect detachment process (autodetachment) as shown by the near zero eKE feature with a binding energy that is detachment wavelength dependent. A striking difference between I^- and $I^- \cdot Y$ is in the eKE dependence of photoelectron angular distributions, especially in the vicinity of Channel II threshold. The origins of these spectral features are discussed in this section.

3.4.1 The photoelectron spectra of $I^- \cdot CO_2$

Photodetachment from $I^- \cdot CO_2$ has been studied before by Neumark et al[21, 105] using zero-electron kinetic energy spectroscopy. Their studies were mainly focused on understanding the neutral cluster electronic potentials. Angular distributions were not measured. Results from their experiments have shown that the binding of I^- to CO_2 results in a T-shaped $I^- \cdot CO_2$ conformer with a slightly bent CO_2 moiety ($\angle$ O-C-O = 174.5°), in contrast to the linear geometry of free CO_2. In neutral $I \cdot CO_2$, the I atom is less tightly bound than in the cluster anion and there is little to no distortion in the case of $I \cdot CO_2$. Therefore, upon photodetachment the bending mode of CO_2, ν_2, is excited, leading to the observed structure in $I^- \cdot CO_2$ band II[21, 105]. Peaks II_1 and II_2 in Figure 3.3 correspond to ν_2 vibrations with 1 and 2 vibrational quanta respectively. Due to loss of resolution as eKE increases, the vibrational structure in band I is not apparent. However a fit to the band I transitions shown in Figure 3.7 using the relative heights of II_0, II_1 and II_2 of band II followed by convolution with an instrumental lineshape reproduces the broad signal quite well. Note that in Figure 3.7, each transition is represented as a doublet. This is because of the lifting

of the degeneracy in the 5p orbitals of neutral I in $[I(^2P_{3/2}) \cdot CO_2]$ results in Channel I being split into two transitions[21, 105]. The splitting is too small (225 cm^{-1}[105]) to resolve in our detector at the electron kinetic energies involved but will contribute to broadening of the Channel I signal. The origin of this splitting will be discussed in detail for $I^- \cdot C_4H_5N$(in Section 3.4.2.2) for which the transitions can be resolved.
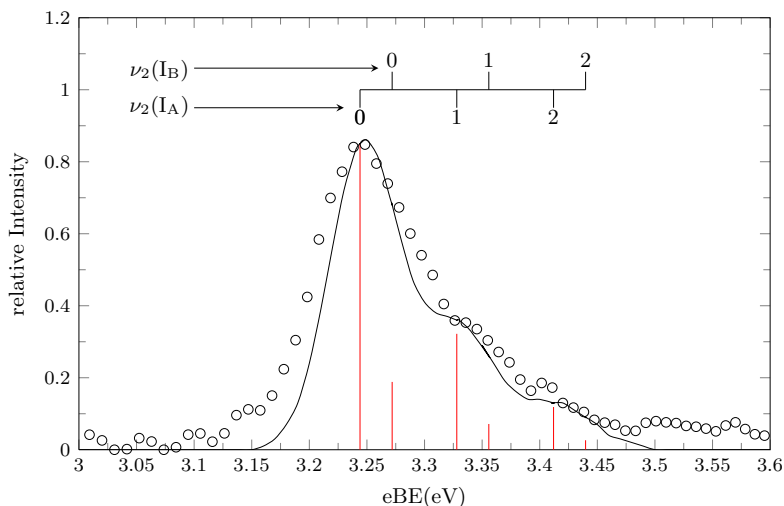
Figure 3.7: Photoelectron spectrum of $I^- \cdot CO_2$ (open circles) at 280 nm showing only the Channel I transitions. The vertical lines represent the estimated Franck-Condon factors for the ν_2 mode. The solid line is a convolution of the Franck-Condon factors with an instrumental lineshape of FWHM = 0.0685 eV. The number of vibrational quanta in the ν_2 mode of the states I_A and I_B giving rise to the Franck-Condon factors is indicated above the spectrum. The stick heights of I_B relative to I_A were obtained from reference [105].

3.4.2 The photoelectron spectra of $I^- \cdot C_4H_5N$

3.4.2.1 The shift in the photoelectron spectra of $I^- \cdot C_4H_5N$

The increase in the minimum energy required to detach an electron from $I^- \cdot Y$ relative to I^- was explained in Section 3.1 in terms of the stabilization of the I^- by the solvent Y. The magnitude of this shift depends on the nature of the anion-molecule interaction. The interaction could, for example, be charge transfer, polarization, charge-dipole interaction, charge-quadrupole interaction, etc. For polar molecules in

43

general, the strongest interaction is the ion-dipole interaction. The dipole moment of pyrrole is slightly smaller than that of water, bromomethane and chloromethane(see Table 3.1). However the observed shift in $I^- \cdot C_4H_5N$ is quite large compared to these three solvents. Thus other types of interaction play an important role in the case of $I^- \cdot C_4H_5N$. Other clusters with comparable ΔE values are $I^- \cdot$aniline($\Delta E = 0.51$ eV) and $I^- \cdot$phenol ($\Delta E = 0.75$ eV)[103]. Comparison of $I^- \cdot C_4H_5N$ with $I^- \cdot H_2O$ is particularly interesting as one might expect a similar interaction (O–H versus N–H) and perhaps the interaction in $I^- \cdot H_2O$ will be stronger due the presence of two O–H bonds. For maximum charge-dipole dominated interaction of I^- and H_2O, one might expect that the iodine atom will lie along the molecular dipole axis (along the C_{2v} axis) bisecting the H–O–H angle. However, Castleman and co-workers[118] have pointed out that a negatively charged ion aligned with the molecular dipole of H_2O will also be repelled by the quadrupole moment of H_2O. Besides, hydrogen bonding between I^- and O–H is also possible. This interaction will will be maximized for a linear O–H$\cdots$I angle[119]. Indeed at the global minimum of $I^- \cdot H_2O$, I^- is essentially bonded to H_2O through one H atom with a nearly linear O–H$\cdots$I angle[117].

In contrast, in $I^- \cdot C_4H_5N$ the iodine atom lies on the dipole axis, the collinearity of the N-H$\cdots$I segment of the cluster maximizing the ion dipole interaction. Further stabilization (of the $^2B_1$ state) is imparted by the quadrupole interaction, for which the positive component lies in the plane of the pyrrole ring, due to the net positive charge on the H atoms peripheral to the heterocycle[120, 121].

Table 3.1: Dipole moments, (μ_Y),[108] and Solvent shifts for H_2O[122], C_4H_5N, CH_3Cl[106] and CH_3Br[106]

Y	C_4H_5N	CH_3Br	H_2O	CH_3Cl
μ (D)	1.77	1.82	1.85	1.89
ΔE (eV)	0.66	0.36	0.47	0.35

3.4.2.2   Origin of the structure in band I of $I^- \cdot C_4H_5N$ spectra

Comparison of I^- and $I^- \cdot C_4H_5N$ photoelectron spectra with the same electron kinetic energies as in Figure 3.4A shows that the cluster transitions are, in general, broader than the corresponding I^- transitions. Such broadening is generally expected upon

cluster formation because of vibrational and rotational degrees of freedom, which are not applicable to atomic photodetachment. Another contributing factor is lifetime broadening due to the dissociation of the neutral cluster produced in the detachment process. An estimation of broadening due to vibrational excitation of the van der Waals modes can be obtained by a Franck-Condon analysis. A Franck-Condon simulation (implemented using the ezSpectrum program)[123] using simple harmonic wave functions and *ab initio* calculated frequencies was performed. The results are shown in Figure 3.8. In the analysis, for simplicity only A1 and N3, which have a similar geometry (hence require no coordinate transformation to account for Duschinsky rotation) and an arbitrary anion temperature of 100 K was assumed. Even though this is not a rigorous approach, it demonstrates that broadening of the direct transitions via vibrational excitation of the neutral cluster is predominantly associated with the van der Waals modes. The progression in Figure 3.8A is mainly a result of the ν_3 van der Waals stretching mode. Since the frequency of this mode is very low (~ 60 cm^{-1}), the progression cannot be resolved on our detector hence the broad peak. Convolution of the stick spectrum in Figure 3.8A with an instrumental Lorentzian line-shape (of the same FWHM as the I(^{2}P$_{3/2}$) transition at the same eKE) results in a smooth profile which is shown in Figure 3.8B. The convoluted signal is still narrower than the experimental peak. Although this treatment is not rigorous, it is sufficient to allow us to conclude that while broadening of the I$^-\cdot$Y transitions is to some extent due to van der Waals modes it is not associated with normal modes excitation of the C$_4$H$_5$N moiety. In the results section it was shown that the Channel I transition in I$^-\cdot$C$_4$H$_5$N is consistently broader than Channel II at the same electron kinetic energy (see Figure 3.4A) and that this is because Channel I transition is actually split into two transitions (Figure 3.4B). The normal modes associated with the pyrrole moiety in these transitions have just been ruled out. Moreover, it is expected that any pyrrole vibrational excitation in Channel I should be present in Channel II. The presence of two conformers can potentially result in the same spectral profile but again a similar profile should also be present in Channel II. In addition, the absence of electrons below 3.45 eV shows that A1 is the only conformer present in the ion-laser interaction region since the only other conformer, A2 has a much lower detachment threshold (3.11 eV). Similarly, the four neutral conformers might also be expected to contribute spectral structure, but again this would be evident in both channels under similar eKE conditions.
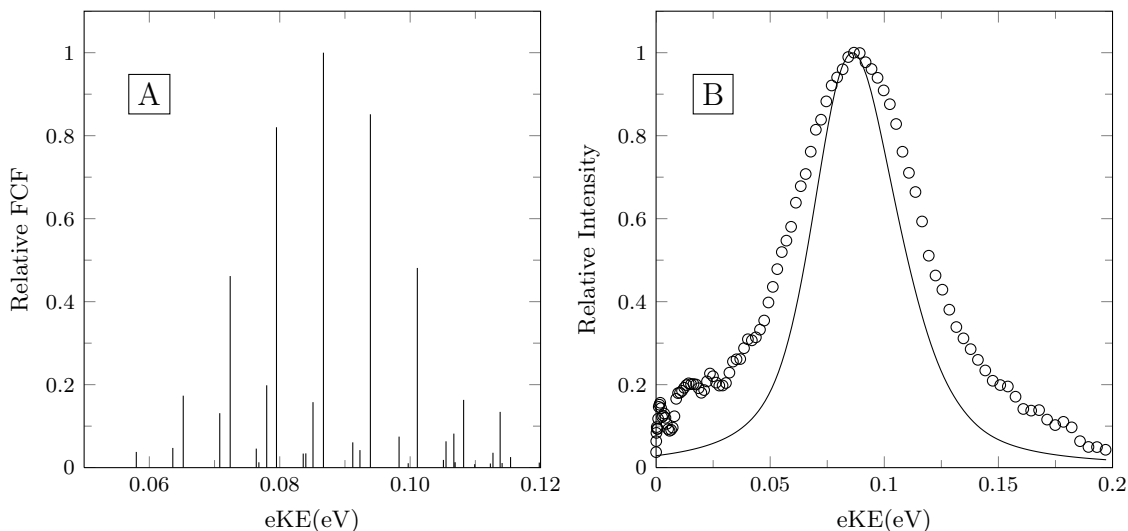
Figure 3.8: A:Relative Franck-Condon Factors associated with the A1 to N3 photodetachment transition in $I^- \cdot C_4H_5N$. B: Channel II 260 nm photoelectron spectrum of $I^- \cdot C_4H_5N$ (open circles) compared to a convolution (solid line) of the Franck-Condon factors with the instrumental, Lorentzian line shape function

Having ruled out all the above, it is argued that the splitting in Channel I arises due to an anisotropic interaction of the 5p orbitals of neutral I with C_4H_5N in $I(^2P_{3/2}) \cdot C_4H_5N$. It was noted that previously the general similarity of the I^- and $I^- \cdot Y$ spectra suggest that in $I^- \cdot C_4H_5N$, photodetachment is primarily from the I^- moiety of the cluster anion leaving an I atom with an open shell. The two lowest electronic states accessible in the removal of a single electron from a free atomic iodide anion are $I(^2P_{3/2})$ and $I(^2P_{1/2})$. Within the C_{2v} framework, the three orbitals transform according to the following irreducible representations; (i) a_1 (p_z), (ii) b_1 (p_x) and (ii) b_2 (p_y). These orbitals and their alignment with respect to the pyrrole molecule are illustrated in Figure 3.9.

Ab initio calculations to determine the relative energies of the resulting states within the C_{2v} framework have been performed . These calculations were performed by placing a hole in each of the atomic p-orbitals in turn using the equilibrium geometry of $I^- \cdot C_4H_5N$. This results in the $^2B_1$ state being the lowest in energy with $^2B_2$ and $^2A_1$ lying 0.028 and 0.159 eV higher respectively. The spin-orbit interaction can be incorporated in a manner similar to reference [124]. In this case the spin-orbit splitting is assumed to be an atomic property of iodine with matrix elements which

46

"p_x" → B$_1$ "p_y" → B$_2$ "p_z" → A$_1$
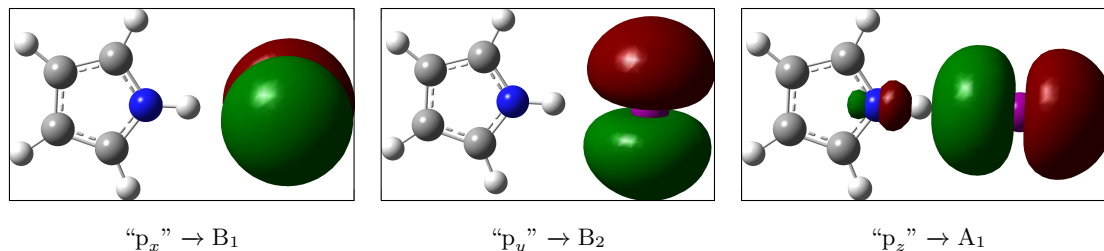
Figure 3.9: Electronic states of I·C$_4$H$_5$N within the C$_{2v}$ framework. The three p orbitals of pyrrole transform according to different irreducible representations to give the states.

do not depend on the geometry of I·C$_4$H$_5$N. The electronic hamiltonian matrix is then written as

$$H = \begin{bmatrix} ^2A_1 & \lambda & \lambda \\ \lambda & ^2B_1 & \lambda \\ \lambda & \lambda & ^2B_2 \end{bmatrix} \tag{3.4}$$

where $\lambda = 0.314$ eV ($\lambda = \xi/2$ and ξ is the spin-orbit coupling parameter). The diagonal matrix elements are the energies of the states calculated above. Diagonalizing H gives the energies of the three states, which will now be called I$_A$, I$_B$ and II, with the spin-orbit interaction included. I$_A$ and I$_B$ are separated by 93 meV and II lies 0.950 eV above I$_A$. These splittings are in fair agreement with the experimental values of 60 meV and 0.958 eV respectively. The variation in potential along the (N)H···I coordinate for each of these states can be approximated by freezing the geometry of the pyrrole moiety and diagonalizing the hamiltonian at different (N)H···I bond lengths. The resulting (diatomic-like) potential curves are shown in Figures 3.10 and 3.13 for the low lying neutral states and the cluster anion ground state. The curves show that asymptotically, I$_A$ and I$_B$ are almost iso-energetic as would be expected for these I orbitals in the absence of the pyrrole moiety. Thus the lifting of the iodine orbital degeneracy by the presence of the pyrrole molecule explains the structure and greater broadening of band I relative to band II in I$^-$·C$_4$H$_5$N photodetachment.
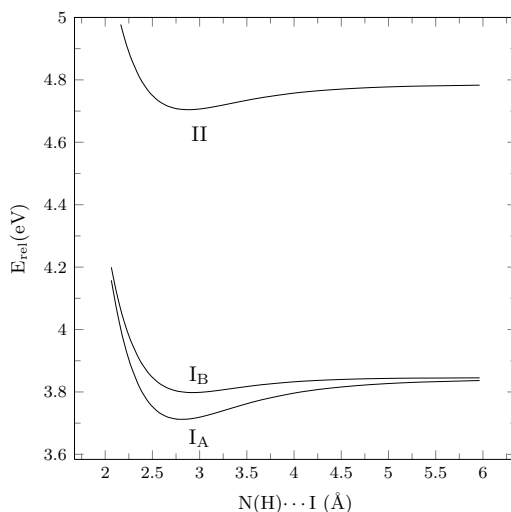
Figure 3.10: Potential energy curves of I·C$_4$H$_5$N states I$_A$, I$_B$ and II relative to anionic conformer A1 along (N)H···I coordinate

3.4.2.3 Indirect detachment channel-The origin of feature X

The presence of a spectral feature at low energy with an eBE that appears to be dependent on the photon energy is a strong indicator of an indirect detachment process. This arises due to electron loss from a temporary excited state. Different mechanisms may lead to electron loss such as energy redistribution or geometry changes within the excited cluster anion. I$^-$ and pyrrole do not possess any covalently bound excited state within the energy regime of the experiment. In fact the electron affinity of free pyrrole is -2.4 eV[125], that is the C$_4$H$_5$N$^-$ anion lies higher in energy than C$_4$H$_5$N. Therefore the excited state cannot be described as localization of an electron in an orbital of either moiety.

Similar indirect detachment features have been observed in photoelectron spectra of the iodide-aniline (I$^-$·C$_6$H$_5$NO$_2$) cluster anion[103, 126]. The dipole moment of an iodine-aniline neutral cluster, at the equilibrium geometry of the ground state iodide-aniline cluster anion was found to be 5.30 D, much larger than the critical dipole moment needed to support a dipole bound state ($\mu > 2.0$ D)[58, 59]. The authors concluded that the indirect detachment was mediated by a dipole bound anion. Upon photoexciation, the weakly bound [I·C$_6$H$_5$NO$_2$] framework of [I·C$_6$H$_5$NO$_2$]$^-$ aniline

dissociates with subsequent decrease in the dipole moment of [I·$C_6H_5NO_2$] leading to loss of an electron[126].

In the I$^-$·C_4H_5N excitation case, the dipole moment of the [I·C_4H_5N] ($\mu = 2.69$ D) at the equilibrium geometry of I$^-$·C_4H_5N is also sufficiently large to bind an electron in a dipole bound state. The existence of the dipole bound state is supported by *ab initio* calculations. The basis sets used above for the calculation of geometries can be used for dipole bound state calculations. The positive end of the dipole in [I·C_4H_5N] at the geometry of I$^-$·C_4H_5N lies on the "iodine side" of the cluster. Since the dipole bound orbital is known to be diffuse, the I basis set was supplemented by addition of 6 diffuse sp functions in a manner similar to reference [127]. These have exponents ranging from 7.35 X 10^{-3} to 2.36 X 10^{-6} with a ratio of 5 between subsequent members of this series. To calculate the dipole bound state (excited state), the initial guess method is used[127]. In this method, first the orbitals of [I·C_4H_5N] are calculated and used as an initial guess for [I·C_4H_5N]$^-$, but with the orbitals re-arranged so that the excess electron is placed one orbital above the lowest unoccupied molecular orbital (LUMO + 1). Conventional energy minimization algorithms in most *ab initio* methods will converge to ground state I$^-$·C_4H_5N rather than [I·C_4H_5N]$^-$ despite the initial orbital switch. To avoid this problem slow converging methods that are used for finding local minima are used. In QCHEM, this is the maximum overlap method while in Gaussian 03 this is the quadratic convergence method. At the cluster anion A1 equilibrium geometry, the dipole bound anion is predicted to be stable relative to the neutral cluster by 0.144 meV. A calculated dipole bound orbital for [I·C_4H_5N]$^-$ showing the characteristic diffuse structure is shown in Figure 3.11.

As discussed above the binding in I$^-$·C_4H_5N is stronger than in I·C_4H_5N. Upon photoexcitation of I$^-$·C_4H_5N to [I·C_4H_5N]$^-$, the electron is transfered from a p-orbital in iodine which effectively removes the charge-dipole and charge-quadrupole interactions between I and C_4H_5N by shifting the charge away from the inter-moiety region. Thus the potential energy surface of I·C_4H_5N is expected to be similar to that of [I·C_4H_5N]$^-$. Considering the lowest energy dipole bound potential, it is predicted that the dipole bound cluster anion is weakly bound with respect to dissociation (at least along the (N)H···I coordinate), a minimum being found at an distance of 2.815 Å. The depth of the minimum of the potential along this coordinate is 0.14 eV and lies at a much longer separation than the A1 cluster anion minimum (Figure 3.12).
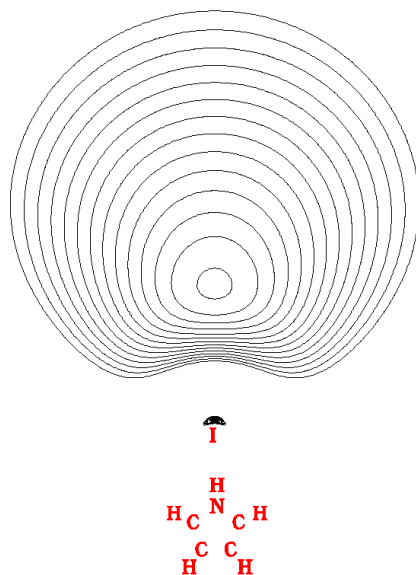
Figure 3.11: Dipole-bound orbital of $[\text{I} \cdot \text{C}_4\text{H}_5\text{N}]^-$ at the equilibrium geometry of $\text{I}^- \cdot \text{C}_4\text{H}_5\text{N}$

As shown in this Figure, the potential energy curve for $[\text{I} \cdot \text{C}_4\text{H}_5\text{N}]^-$ is very similar to that of the state I_A of the neutral cluster N3. However, as the $(\text{N})\text{H} \cdots \text{I}$ distance increases, the dipole moment decreases, consequently destabilizing the dipole bound cluster anion relative to the neutral cluster. At a distance of 3.965 Å the energies of the diabats coincide and after this point there is a reversal of the energy state ordering.

It is argued therefore that the indirect detachment channel is associated with electron loss from $[\text{I} \cdot \text{C}_4\text{H}_5\text{N}]^-$ much like in $[\text{I} \cdot \text{C}_6\text{H}_5\text{NO}_2]^-$. The disappearance of the indirect detachment band X signal at 310 nm and re-appearance at 270 nm is consistent with a dipole bound state lying in the vicinity of a neutral surface. At 310 nm the indirect detachment associated with Channel I is no longer favorable. As the Channel II threshold is approached the signal re-emerges as another dipole bound state associated with this channel opens. The autodetachment process may be envisioned as follows;

$$\text{I}^- \cdot \text{C}_4\text{H}_5\text{N} \xrightarrow{h\nu} [\text{I} \cdot \text{C}_4\text{H}_5\text{N}]^- \longrightarrow \text{I} + \text{C}_4\text{H}_5\text{N} + \text{e}^- \qquad (3.5)$$
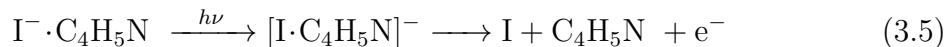
Although there is a shallow minimum along the $(\text{N})\text{H} \cdots \text{I}$ for the dipole bound state, this minimum lies at longer separation than the minimum in $\text{I}^- \cdot \text{C}_4\text{H}_5\text{N}$. Vertical excitation accesses the repulsive wall of the dipole bound species (Figure 3.13) at
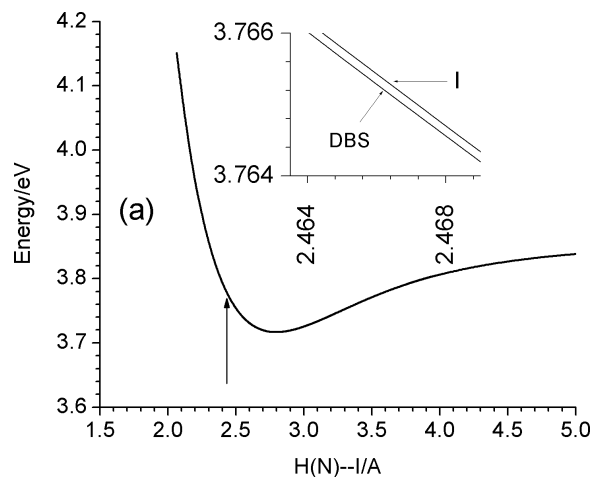
Figure 3.12: Potential energy curves along the (N)H$\cdots$I coordinate for the neutral ground state (I$_A$) and the associated dipole bound state (DBS) in the region of the A1 minimum. The vertical arrow marks the position of the minimum on the corresponding I$^-\cdot$C$_4$H$_5$N potential energy curve along the same coordinate.
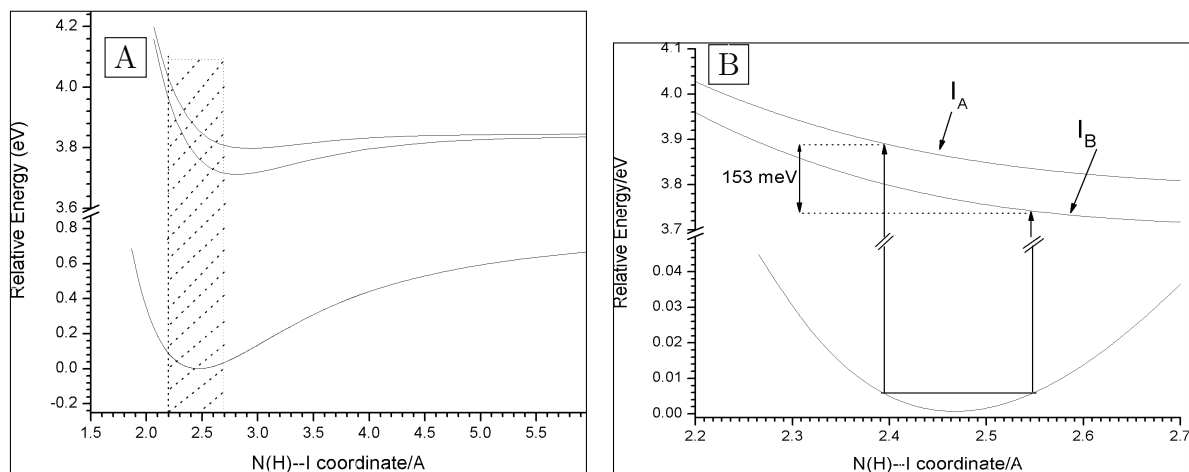
Figure 3.13: A:Relative energies along (N)H$\cdots$I coordinate for A1 conformer of I$^-\cdot$C$_4$H$_5$N and I$_A$ and I$_B$ neutral sates. B: Zoom in of the shaded part of the plot in A which gives an indication of the energy differences between these states at the zero point energy of the ν_3 mode.

51

energies predominantly close to or above the 0.14 eV dissociation limit. Subsequent motion along the inter-moiety axis lengthens the physical bond and therefore reduces the dipole moment. The result is the crossing of the dipole bound state and neutral diabats as explained above. This will result in electron loss as the dipole moment becomes too small to support a dipole bound anion.

It might be expected that because the dipole moment of [I·C$_4$H$_5$N] at the equilibrium geometry of I$^-$·C$_4$H$_5$N is so small (as also evidenced by the very small binding energy of the dipole bound anion), that the indirect detachment signal should be limited to a very narrow range of energies very close to the Channel I and Channel II thresholds. On the contrary, the autodetachment feature is observed up to 0.35 eV above, and 0.27 eV below Channel I threshold. The persistence of this signal *above* threshold can be understood by considering Figure 3.13. The potential curves of this Figure show that the repulsive region of the dipole bound state potential lies in the region covering the range of probable cluster anion ground state zero point (N)H$\cdots$I separations. This will result in good overlap of the ground state anion bound nuclear wavefunctions with continuum wavefunctions of the excited state for quite a wide range of photon energies. An estimation of this range can be made by comparing the potential energy curves of the ground and excited states of the anion in Figure 3.13B. The vertical arrows correspond to the turning points of the cluster anion ground state zero point level in a simplistic diatomic-like picture. These show that photon excitation from 3.74 to 3.89 eV can feasibly access dipole bound states immediately below the I$_A$ and I$_B$ neutral states which are of course very close to the dipole bound states. The upper limit of this estimate is within 200 meV of the photon energy at which the autodetachment feature disappears above the Channel I threshold. Given that this approximation neglects hot bands and only considers the dipole bound state along the (N)H$\cdots$I coordinate, the production of dipole bound cluster anions up to 350 meV above threshold seems reasonable.

The persistence of the autodetachment signal *below* the direct detachment threshold is more puzzling. Based on the *ab initio* results, the minimum energy required to access the neutral conformer N3 is 3.72 eV but the indirect detachment signal starts to appear at 3.45 eV. Hotbands in the van der Waals modes will only account for small decrease in the threshold energy for detachment. The role of anion conformer A2 was ruled out before on account of lack of any signal corresponding to the calculated vertical

detachment energy (3.11 eV) for this conformer. In addition, the dipole moment of the corresponding neutral cluster is only 1.85 D which is below the minimum for binding an electron by the dipole field. Therefore no indirect detachment signal is expected from this conformer. Photodissociation of the pyrrole molecule followed by electron loss can also be ruled out on energetic grounds. The lowest spin-allowed electronic transition (which is symmetry forbidden) for the pyrrole molecule ($\pi \rightarrow \sigma^*$) has an energetic onset of 4.96 eV[128].

Until now, the indirect detachment process has been discussed in terms of initial C_{2v} anion geometries. However, the van der Waals modes associated with cluster species typically correspond to wide amplitude motion. Motion associated with the ν_1 and ν_2 modes allows the cluster anion to sample a wide range of the potential surface without being limited to the region associated with C_{2v} symmetry. Excitation from any of the wide range of initial geometries can therefore sample a wide range of excited state geometries. The energy of the neutral cluster varies considerably with geometry (as seen in the differences for the stable conformers N1-N4 in Figure 3.6). Likewise, the closely associated dipole bound state will vary in a similar manner, assuming that the dipole moment remains above the critical value. Let us consider an extreme case in which conformer N1 is accessed due to the van der Waals modes (ν_1 and ν_2) sampling that geometry in the anion. The calculated dipole moment for N1 (3.45 D) is above the minimum necessary to bind an electron. Thus dipole bound anions are not limited to the C_{2v} initial geometry. Under this argument the reduction of the photon energy required for production of a dipole bound intermediate in the indirect detachment channel is at least feasible. The requirement would be significant overlap between the vibrational wave functions associated with the van der Waals modes allowing the I atom to move in a plane perpendicular to the plane of the pyrrole molecule. It must be borne in mind that the energy required for excitation of any dipole bound state in this picture lies approximately within a meV of the energy required for direct detachment. Franck-Condon considerations suggest that both the direct and indirect detachment yields due to these excitations will be a weak contribution. Nevertheless, since these excitations lead to formation of a dipole bound state, directly detached photoelectrons should also be produced. Taking photodetachment at 320 nm as an example, conservation of energy suggests that eKEs up to 0.48 eV might be observed (using the energy of the N1 conformer as an approximate limit). The spectrum shown

in Figure 3.4B has a weak but clear tail in the distribution extending up to >0.4 eV, lending plausibility to the arguments advanced above.

3.4.3   Photoelectron angular distributions

The evolution of I^- $\beta_{3/2}$(eKE) and $I^- \cdot Y$ β_I(eKE) was described in Section 3.3.2 on page 38. The similarity of β_I to $\beta_{3/2}$ values for both clusters far from Channel II threshold also supports the view that in $I^- \cdot C_4H_5N$ and $I^- \cdot CO_2$, the electron is best described as a localized p-orbital of iodine. This trend shows the familiar Bethe-Cooper-Zare behavior[40, 129, 130] expected for detachment from an atomic p orbital. This trend shall be explained more fully in Chapter 4. The deviation of β_I from I^- $\beta_{3/2}$ in the vicinity of Channel II is interesting for two reasons; (i) In both clusters, the deviation clearly peaks near or at the threshold of Channel II, and (ii) The relative magnitude of the deviation is cluster dependent. The discussion of these observations is deferred until Chapter 4, which is entirely devoted to cluster anion photoelectron angular distributions near the Channel II threshold. In that Chapter, this effect shall be quantified and more solvents studied for comparison. For now suffice it to say that this near Channel II threshold behavior of β_I results from spin-orbit relaxation of the iodine moiety in the dipole supported state $[I(^2P_{1/2}) \cdot Y]^-$ (transient or bound) to $[I(^2P_{3/2}) \cdot Y]^-$ accompanied by electron ejection[122, 131–133].

3.5   Summary

Photoelectron spectra and angular distributions for $I^- \cdot C_4H_5N$ and $I^- \cdot CO_2$ have been studied using velocity mapped photoelectron imaging. In general the photoelectron spectra of $I^- \cdot C_4H_5N$ and $I^- \cdot CO_2$ resemble those of I^- but there are also some differences. The differences highlight the effect of solvation on atomic anion photodetachment. The vibrational struture in $I^- \cdot CO_2$ indicates that the I^- anion distorts the CO_2 molecule from its linear geometry to a bent O–C–O bond angle. The structure in the Channel I band of $I^- \cdot C_4H_5N$ photodetachment is of a different origin, being the anisotropic interaction of 5p orbitals of the I atom with C_4H_5N in $I(^2P_{3/2}) \cdot C_4H_5N$. The larger than expected stabilization energy for I^- in $I^- \cdot C_4H_5N$ is attributed to

favorable charge-dipole, charge-quadrupole and hydrogen bonding interactions. Excitation of $I^- \cdot C_4H_5N$ near channel thresholds accesses a weakly bound dipole bound anionic state of the form $[I \cdot C_4H_5N]^-$. This state autodetaches resulting in electrons with a near zero kinetic energy. The persistence of autodetachment over an unexpectedly large energy window above the vertical detachment energy is due to good overlap between the continuum nuclear wave functions of the dipole bound state and the bound nuclear wave functions of the cluster anion ground state over a wide range of photon energies. The autodetachment also persists over a wide energy window below the vertical detachment energy as well. This is evidence that the photoexcitation also samples not only the global minimum of the $I^- \cdot C_4H_5N$ cluster but also other geometries which may also be excited to the dipole bound surface subsequently autodetaching.

Chapter 4

Photodetachment in monosolvated I⁻: Photoelectron angular distributions and branching ratios

4.1 Introduction

In 1977, Fox and Hayon studied the absorption spectra of atomic bromide[134] and iodide[135] in a number of solvents and found that in each case the first two strongest bands (which they called A_1 and A_2) were separated by about the same energy as the separation of the ^2P spin orbit states ($^2P_{3/2}$ and $^2P_{1/2}$) of atomic bromine and iodine. Absorption of a photon by I⁻ and Br⁻ in excess of the electron affinities of the neutral atom (3.059 eV and 3.364 eV respectively[99]) leads to unstructured absorption spectra because of electron loss into the continuum[30]. Thus, excited states of these anions are unbound. The bands observed in the solutions of atomic iodide and bromide were thus designated charge-transfer-to-solvent (CTTS) bands. In the case of aqueous solutions for example, this may be represented schematically as:

$$X^-_{aq} \xrightarrow{h\nu_1} X^{-*}_{aq} \qquad\qquad A_1 \qquad\qquad (4.1)$$

$$X^-_{aq} \xrightarrow{h\nu_2} X^{-**}_{aq} \qquad\qquad A_2 \qquad\qquad (4.2)$$

Gas phase studies of solvated halide clusters were initially based on mass spectrometric methods to extract thermodynamic properties of ion-molecule solvation[136–138].

Early experiments utilizing photoelectron spectroscopy were performed by Markovich et al.[101, 139–143] who studied the solvation of I^-, Cl^- and Br^- by water, acetonitrile, ammonia and carbon dioxide. These experiments mainly probed the solvent molecule arrangement in finite size clusters by studying the effect of increasing the number of solvent molecules around the ion on the electron binding energies. The photoelectron spectra of these clusters were found to show two bands separated by the spin-orbit splitting of the halogen as in the photodeatchment of free halides but shifted to higher energies. The bands in the $X^-\cdot Y$(X = Cl, Br, or I and Y = solvent molecule) spectra are therefore due to transitions correlating asymptotically to the production of $[X(^2P_{3/2}) + Y + e^-]$ and $[X(^2P_{1/2}) + Y + e^-]$ respectively i.e;

$$X^-\cdot Y \longrightarrow X(^2P_{3/2}) + Y + e^- \qquad (4.3)$$

$$X^-\cdot Y \longrightarrow X(^2P_{1/2}) + Y + e^- \qquad (4.4)$$
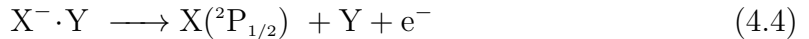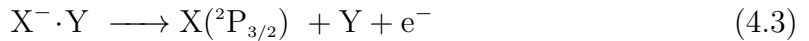
(4.3) will be referred to as Channel I and (4.4) as Channel II. In an interesting study that linked directly the finite size cluster properties to the bulk system of Fox and Hayon[135] the photoabsorption cross sections for $I^-\cdot(H_2O)_n$(n = 0-4) were measured[30]. These experiments showed that even singly solvated atomic halide clusters show similarities to CTTS behavior. In these smaller clusters, the transitions have been attributed to vertical excitations from the highest occupied orbital in the ground state with an electron mainly localized in an iodine 5p orbital, to a diffuse orbital supported by the dipole moment of the neutral cluster framework, forming a dipole bound anion provided the dipole moment is within or greater than the critical range of 2-2.5 D. Thus cluster dipole bound states are usually considered precursors of the CTTS states[30]. The dynamics involved in the excitation to CTTS and DB states have been studied using time resolved photoelectron spectroscopy[132, 133, 144–148] and coincidence imaging[149]. Also a number of *ab initio* calculations have been performed to determine the structures of the clusters in the gas phase and the excitation dynamics[127, 150–154]. The role of the atomic halogen upon excitation of the clusters to the excited DB states has been a subject of much debate both theoretically and experimentally[127, 144, 149, 155–157].

Most of the studies so far have focused on excitations near the Channel I threshold. An exception is the time-resolved photoelectron spectroscopic study of $I^-\cdot Xe_n$(n=11,20,38)[132, 133]. Results show that the lifetime of a CTTS state near

the Channel II threshold is much shorter than that of the first CTTS state near the Channel I threshold. The authors concluded that the neutral core of the second CTTS state (which lies near the Channel II threshold) relaxes to the ground state and consequently an electron is ejected to remove the excess energy.

Recently in our group, a series of studies involving I^- solvated by methyl halides showed that photoelectron angular distributions are sensitive to the interaction of the electron and the neutral framework upon photodetachment, in the vicinity of molecular scattering resonances and I^- channel thresholds[42, 106, 131]. An anomaly in the angular distributions near threshold for the opening of Channel II of $I^- \cdot CH_3I$ photodetachment was attributed to the formation of a dipole bound state but interpretation was complicated by the presence of a σ^* resonance for this cluster. In Chapter 3 Photoelectron angular distributions of $I^- \cdot C_4H_5N$ and $I^- \cdot CO_2$ were presented. These showed similar anomalies near the Channel II threshold. These cluster anions have no low lying σ^* resonances that can be accessed in our experiments. Interestingly $I^- \cdot CO_2$ showed this anomaly despite CO_2 having no net dipole moment. Considering the magnitude of this anomaly, the change in $\beta_I(C_4H_5N)$ is bigger than that of $\beta_I(CO_2)$ near the vicinity of the Channel II threshold. Thus, the magnitude of the anomaly depends on the solvent. In this Chapter a detailed investigation the dependence of this effect on the dipole moment using a series of solvents of different polarities in $I^- \cdot Y$ photodetachment (Y = acetonitrile(CH_3CN), water (H_2O), nitromethane (CH_3NO_2) and acetone (($CH_3)_2CO$)) is presented.

4.2   Experimental

Details of the velocity mapped photoelectron imaging spectrometer were presented in Chapter 2. Here only specific details for anion production are presented. $I^- \cdot CO_2$ and $I^- \cdot C_4H_5N$ were produced as reported in Chapter 3. All other anions were produced upon supersonic expansion by electron impact. In this case a mixture of Argon (~ 400 psig) and methyl iodide (ambient pressure) was regulated to the desired pre-nozzle stagnation pressure (30-80 psig) and bubbled through the solvent Y.

The laser dyes DCM, pyromethene 597, pyromethene 580, coumarin 307 and coumarin 153 were used to obtain different photodetachment wavelengths. For each of the

cluster anions above, photoelectron images were collected at intervals ranging from <0.02 eV to 0.1 eV. Photoelectron spectra and angular distributions were extracted at each wavelength according to the methods described in Chapter 2. To obtain further insight into the structure and dynamics of these anions, *ab initio* calculations were performed using the Q-CHEM[113] and Gaussian 03[114] suites of programs as described in Chapter 3.

4.3 Results and analysis

4.3.1 Photoelectron spectra

A series of velocity mapped photoelectron images for I^-, $I^- \cdot CO_2$, $I^- \cdot H_2O$, $I^- \cdot C_4H_5N$, $I^- \cdot CH_3COCH_3$, $I^- \cdot CH_3NO_2$ and $I^- \cdot CH_3CN$ were obtained over a range of photon energies covering the two lowest detachment channels. Photoelectron spectra and angular distributions were extracted from these images in the manner described in Chapter 2. Representative BASEX[95] transformed photoelectron images of I^- and $I^- \cdot Y$ are shown in Figure 4.1. Each dark ring in the transformed images corresponds to a photodetachment transition and the degree of darkness is proportional to photoelectron intensity. Selected photoelectron spectra at sufficiently short wavelengths to clearly show both spectral bands are also shown in Figure 4.2. Photodetachment from I^- produces I atoms in either the $I(^2P_{3/2})$ or $I(^2P_{1/2})$ spin orbit states. The miniumum energy required to detach an electron from I^- is 3.059 eV[99] producing $I(^2P_{3/2})$. 0.943 eV[100] in excess of this energy (4.002 eV) is required to access $I(^2P_{1/2})$. Thus the outer and inner rings in the I^- images correspond to $I(^2P_{3/2})$ or $I(^2P_{1/2})$ transitions respectively. Photoelectron spectra for $I^- \cdot Y$ were calibrated against the I^- transitions. Except for the spectrum of $I^- \cdot CO_2$, the $I^- \cdot Y$ images and spectra look very similar to those of I^-. Each spectrum is characterized by two bands separated by ~ 0.94 eV which corresponds to the spin orbit splitting in iodine. In each case both bands are however shifted to higher binding energies.

Near the threshold of Channel I the photoelectron spectra of $I^- \cdot H_2O$ and $I^- \cdot CH_3CN$ show relatively weak features at higher binding energies than the band origins. The peak separation between the main band and the weak feature in $I^- \cdot H_2O$ is $\sim$1600
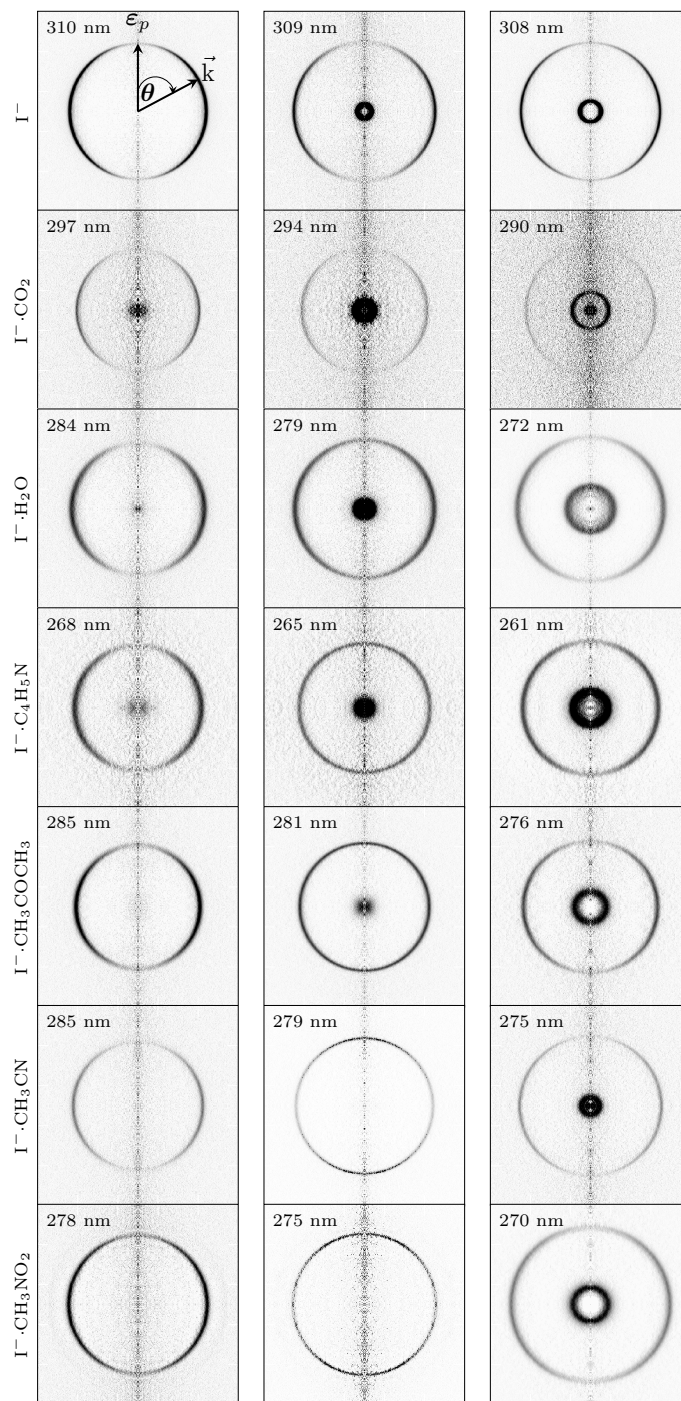
Figure 4.1: Transformed photoelectron images near the Channel II threshold. As shown on the 310 nm image of I^-, θ is the angle between the photon electric field vector, ε_p, and the direction of the photoelectron momentum, $\vec{k}$.
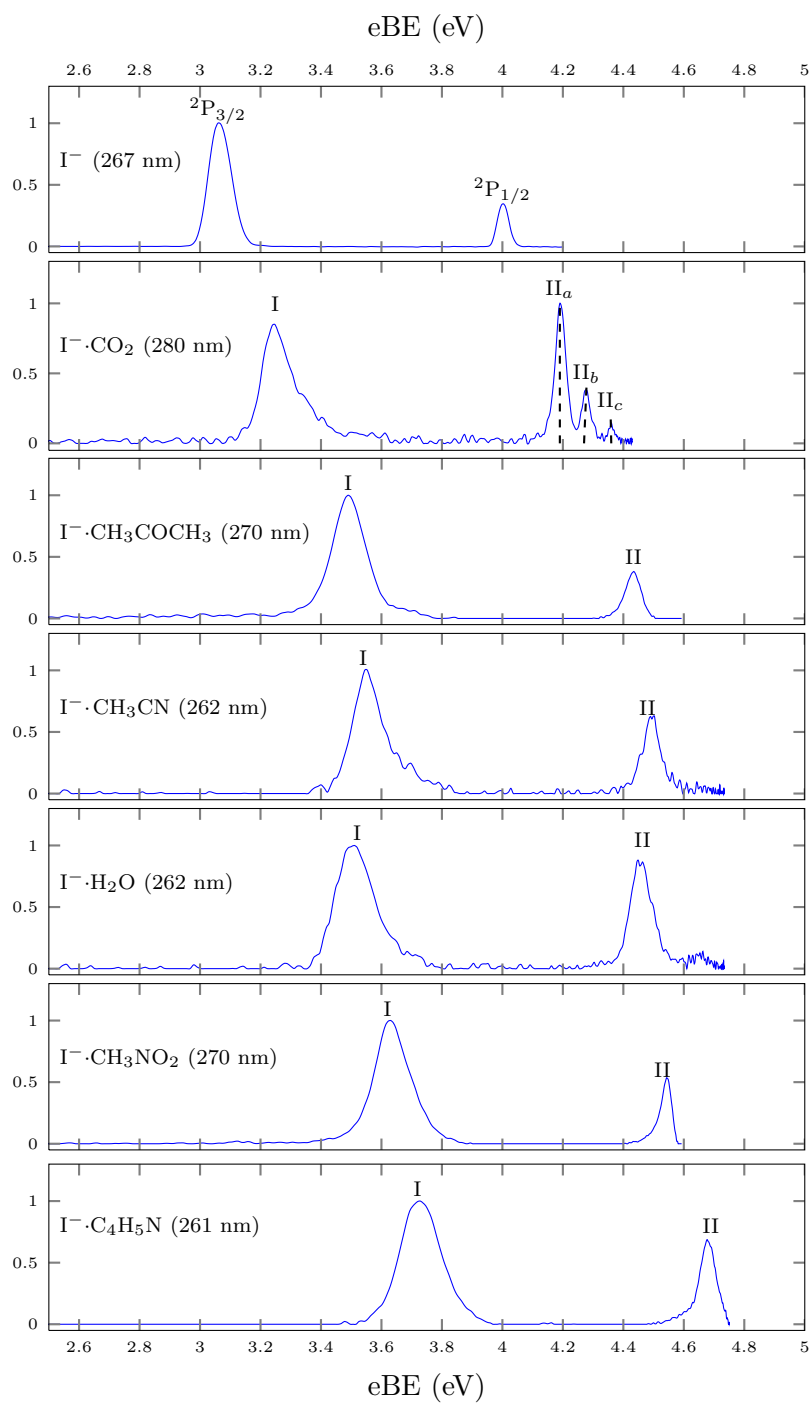
Figure 4.2: Selected photoelectron Spectra of monosolvated I⁻

cm^{-1} and ~1500 cm^{-1} in $I^- \cdot CH_3CN$. The spacing in $I^- \cdot H_2O$ is very close to the bending vibrational mode of H_2O at 1595 cm^{-1}[158]. In $I^- \cdot CH_3CN$ the separation is quite close to the CH_3 antisymmetric deformation mode at 1448 cm^{-1}[158].

To investigate the origin of the structure, Franck-Condon analyses for photodetachment from $I^- \cdot H_2O$ and $I^- \cdot CH_3CN$ were performed. Polyatomic Franck-Condon factors can be calculated using Sharp and Rosenstock's method of multidimensional generating functions[159]. This method has proper treatment of the Duschinsky effect[160]. Chen's method which is based on the formulation of Sharp and Rosenstock but utilizes normal mode displacement Cartesian coordinates which are routinely output by *ab initio* programs, alongside the geometries and the frequencies of the normal modes[161] was used. As in $I^- \cdot C_4H_5N$ different conformers are possible depending on the position of the iodine atom with respect to the solvent molecule. Identification of the major anionic and neutral conformers contributing to the observed photodetachment signal is crucial for a reasonable understanding of experimental results. Minimum energy conformers for the anionic clusters have been calculated previously[104, 162–164]. The iodine atom in $I^- \cdot CH_3CN$ resides in the "methyl pocket" as shown in Figure 4.3A[164]. The basis sets described in Chapter 3 to optimize the geometry of this conformer were used. A detailed geometry search for $I \cdot CH_3CN$ resulted in structure similar to the one in Figure 4.3B. The geometry of $I^- \cdot H_2O$ is shown in Figure 4.4. Theoretical calculations show that there a three conformers of $I \cdot H_2O$[104, 162, 163]. Calculated vibrational frequencies of neutral conformer with geometry similar to $I^- \cdot H_2O$ have been found to be consistent with experimental zero-electron-kinetic energy spectra[104]. Starting from the geometries of $I^- \cdot H_2O$ and $I \cdot H_2O$ (Table 4.2) calculated by Schlicht et al.[104], the frequencies and normal mode displacement coordinates for both clusters were calculated as in reference [104] at the B3LYP level of theory using the 6-311++G(3df,3pd) basis set for both oxygen and hydrogen atoms. The LANL2DZ effective core potential and LANLDZspdf basis set was used for the iodine atom. Details of the bond angles and lengths for both clusters are presented in Tables 4.2 and 4.1.

The results of the Franck-Condon calculations are shown in Figures 4.5 as stick spectra. These were compared to the experimental spectra by convolution with a Gaussian lineshape. The experimental lineshape width used is that of I^- spectrum at the same eKE as the $I^- \cdot H_2O$ and $I^- \cdot CH_3CN$ transitions. Note that the 325 nm spectrum of $I^- \cdot H_2O$ and the 330 nm spectrum of $I^- \cdot CH_3CN$ were used in Figure 4.5 since these
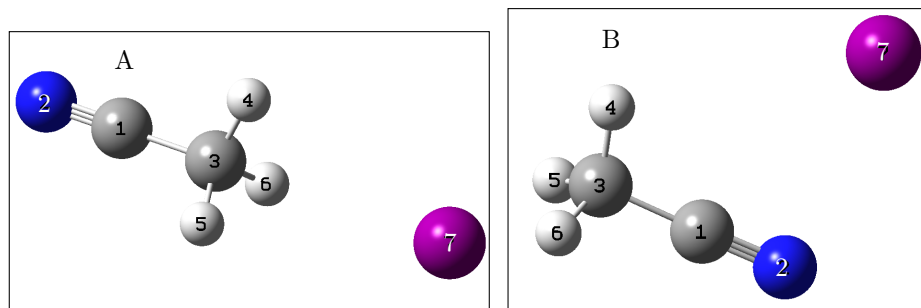
Figure 4.3: Calculated geometries of I$^-$·CH$_3$CN (A) and I·CH$_3$CN (B). Bond lengths and angles are shown in Table 4.1

Table 4.1: Calculated bond lengths (Å) and angles (degrees) for I$^-$·CH$_3$CN and I·CH$_3$CN. See text for details of calculations.

	I$^-$·CH$_3$CN	I·CH$_3$CN
C(1)–C(3)	1.471	1.469
C(1)–N(2)	1.187	1.187
C(3)–H(4)	1.098	1.100
H(4)–C(3)–H(6)	107.6	109.4
I(7)···C(3)	3.589	- -
I(7)···H(6)–C(3)	93.5	- -
C(1)···I(7)–N(2)	- -	20.3
C(1)···I(7)	- -	3.416
N(2)···I(7)	- -	3.248
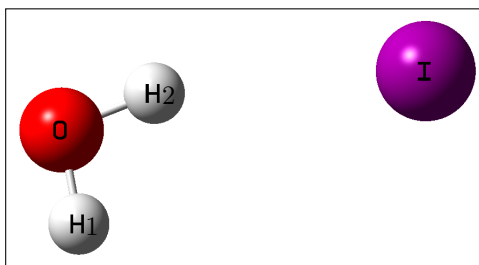
Figure 4.4: Calculated geometry of I$^-$·H$_2$O. See Table 4.2 for details of the geometry

63

Table 4.2: Calculated bond lengths (Å) and angles (degrees) for $I^-\cdot H_2O$ and $I\cdot H_2O$. See text for details of calculations.

	H1–O	H2–O	O$\cdots$I	I$\cdots$H2–O	H–O–H
$I^-\cdot H_2O$	0.961	0.979	3.619	162.6	101.7
$I\cdot H_2O$	0.961	0.965	3.926	178.1	105.3
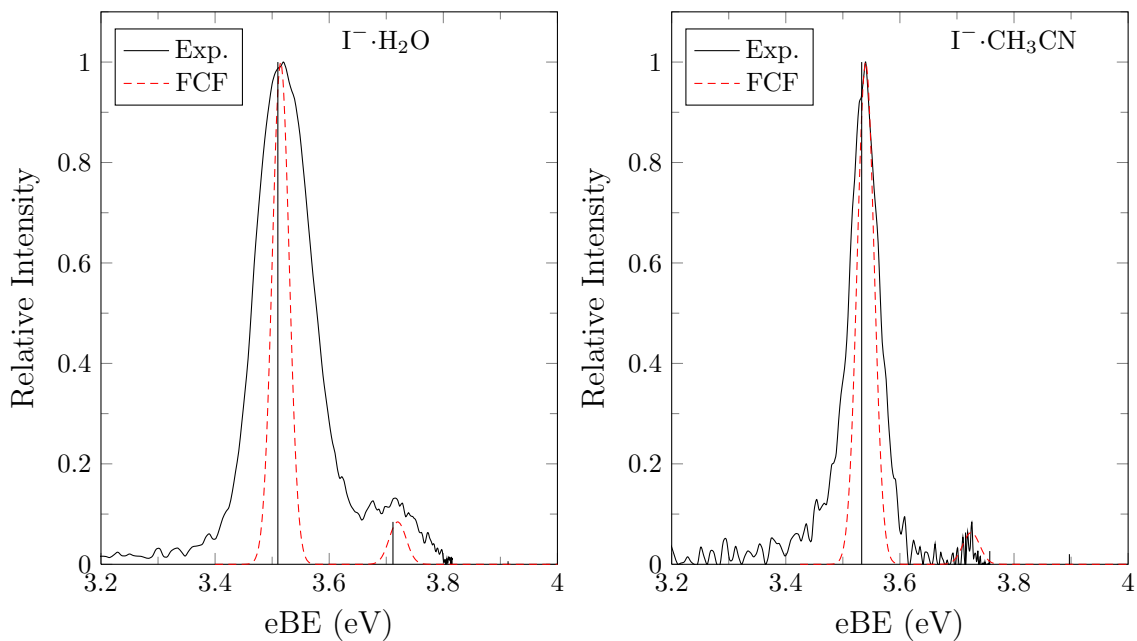
Figure 4.5: Experimental and Franck-Condon simulated photoelectron spectra of $I^-\cdot H_2O$ (325 nm) and $I^-\cdot CH_3CN$ (330 nm). The Franck-Condon factors are shown as the vertical solid lines. See text for details

show better resolution of the features than the spectra in Figure 4.2. There is good agreement between the experimental spectra and simulated spectra indicating that the weak features in both spectra are due to Franck-Condon effects. However, the simulated spectra are narrower than experimental spectra possibly due to hot bands, lifetime broadening due to the cluster dissociation following photodetachment and Channel I splitting due to anisotropic interaction of I with H_2O and CH_3CN similar to the more pronounced splitting discussed in Chapter 3 for $I^- \cdot C_4H_5N$.

4.3.2 Photoelectron angular distributions and cross sections

The photoelectron angular distributions of I^- and all the cluster anions are quantified as $I(\theta)$. Since linearly polarized photons were used for photodetachment, an anisotropy parameter β (Chapter 1) for Channel I photoelectrons was extracted according to the method described in chapter 2 (this is the outer ring in the images and the band marked "I" in the photoelectron spectra of Figure 4.2). As before, specifically this value will be referred to as $\beta_{3/2}$ for I^- and β_I for the clusters. The distributions for I^- and $I^- \cdot Y$ show dependence on the kinetic energy of the departing electron as evidenced by the photoelectron images in Figure 4.1. The evolution of $\beta_{3/2}(eKE)$ and $\beta_I(eKE)$ is shown in Figure 4.6. Also included are β_I data for $I^- \cdot CH_3Cl$ and $I^- \cdot CH_3Br$[106]. Each data point represents $\beta_{3/2}$ or β_I averaged over the FWHM of the channel I transition. Each point arises from a different detachment wavelength, and solid lines are extended through these as a guide to the eye. The $\beta_{3/2}(eKE)$ evolution for I^- was described in the previous Chapter. The evolution of the asymmetry parameter with eKE ($\beta_I(eKE)$) for photodetachment from $I^- \cdot Y$ is somewhat different. Far from the Channel II threshold, β_I is essentially similar to $\beta_{3/2}$ for I^-. As the Channel II threshold is approached, β_I begins to deviate from the I^- trend, gradually becoming less negative until a maximum value is reached, whereupon it decreases and gradually returns close to the I^- value. For $I^- \cdot CH_3CN$ and $I^- \cdot CH_3NO_2$, β_I even changes sign from negative to positive. On average, this behavior spans an eKE range of ~ 0.15 eV. For each cluster anion image in Figure 4.1, the left and right images show a predominantly perpendicular distribution for the Channel I transition. The central images however have quantitatively different PADs. In many cases this is noticeable by eye.

Channel branching ratios (Channel II:Channel I) have also been measured by integrating under each channel's spectral profile. These are plotted in Figure 4.7 for I^- and $I^- \cdot Y$. Upon opening of Channel II, the branching ratio for I^- rises rapidly to the statistical value of 0.5. The behavior of the branching ratios for $I^- \cdot Y$ can be grouped broadly into two categories: $I^- \cdot CO_2$, $I^- \cdot H_2O$, $I^- \cdot CH_3Cl$ and $I^- \cdot CH_3Br$ are in the first category, for which the branching ratios increase significantly beyond the statistical limit. $I^- \cdot CH_3COCH_3$, $I^- \cdot CH_3CN$ and $I^- \cdot CH_3NO_2$ are in category 2 with branching ratios remaining at the statistical value. In some ways $I^- \cdot C_4H_5N$ is intermediate between these two extremes.

The $I^- \cdot CH_3CN$ relative photodetachment cross sections near the Channel II threshold were measured by comparison with I^- using the event counting mode of the photoelectron imaging software. Here, the number of electron impacts on the MCP are simply summed together for a predefined number of laser shots. At the photon energies involved, the cross section for I^- photodeatchment is fairly constant[22, 30] and therefore any change in the electron count ratio is due to the change in the number of electrons from $I^- \cdot CH_3CN$ excitation. The results in Figure 4.8 show a strong enhancement of the photodetachment cross section near the Channel II threshold.

4.4 Discussion

The results presented above show some interesting features especially in the photoelectron angular distributions and branching ratios. The rapid change in $\beta_I(eKE)$ for photodetachment from clusters $I^- \cdot Y$ as the Channel II threshold is approached suggests that the channels are coupled. In addition the degree of deviation of $\beta_I(eKE)$ seems to be dependent on the solvent molecule Y. In this section, the origin of the $\beta_I(eKE)$ behavior and why it varies with solvent Y will be discussed. It will be argued that the channel branching ratios presented above can be attributed to similar origins. First, however, a brief discussion of the photoelectron spectra obtained for these clusters follows.
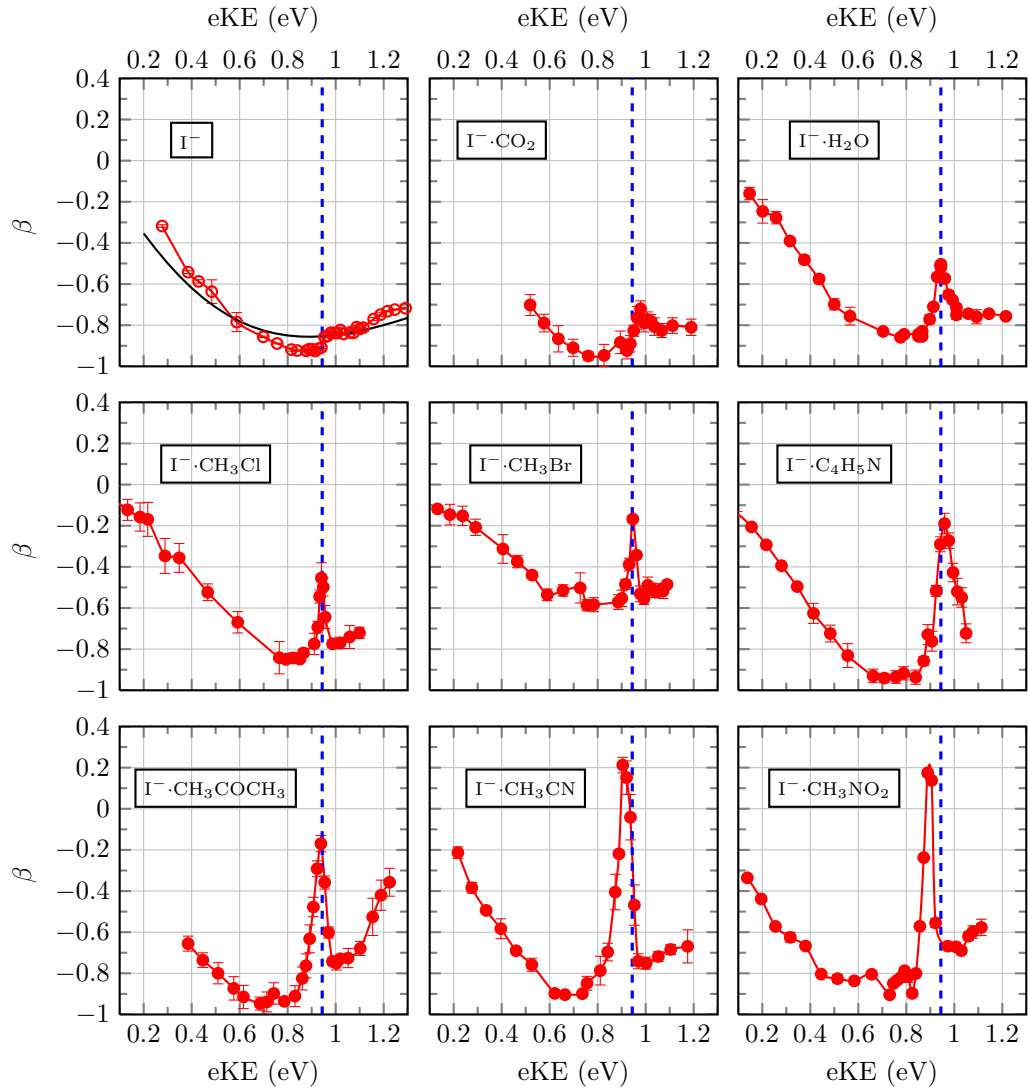
Figure 4.6: Anisotropy parameters for photodetachment from $I^-(\beta_{3/2})$ and $I^- \cdot Y(\beta_I)$. The dashed line on each plot marks the kinetic energy of $I(^2P_{3/2})$ channel electrons at the opening of $I(^2P_{1/2})$. The black solid line in I^- plot is a fit of the data to equation 4.5. See text for details.
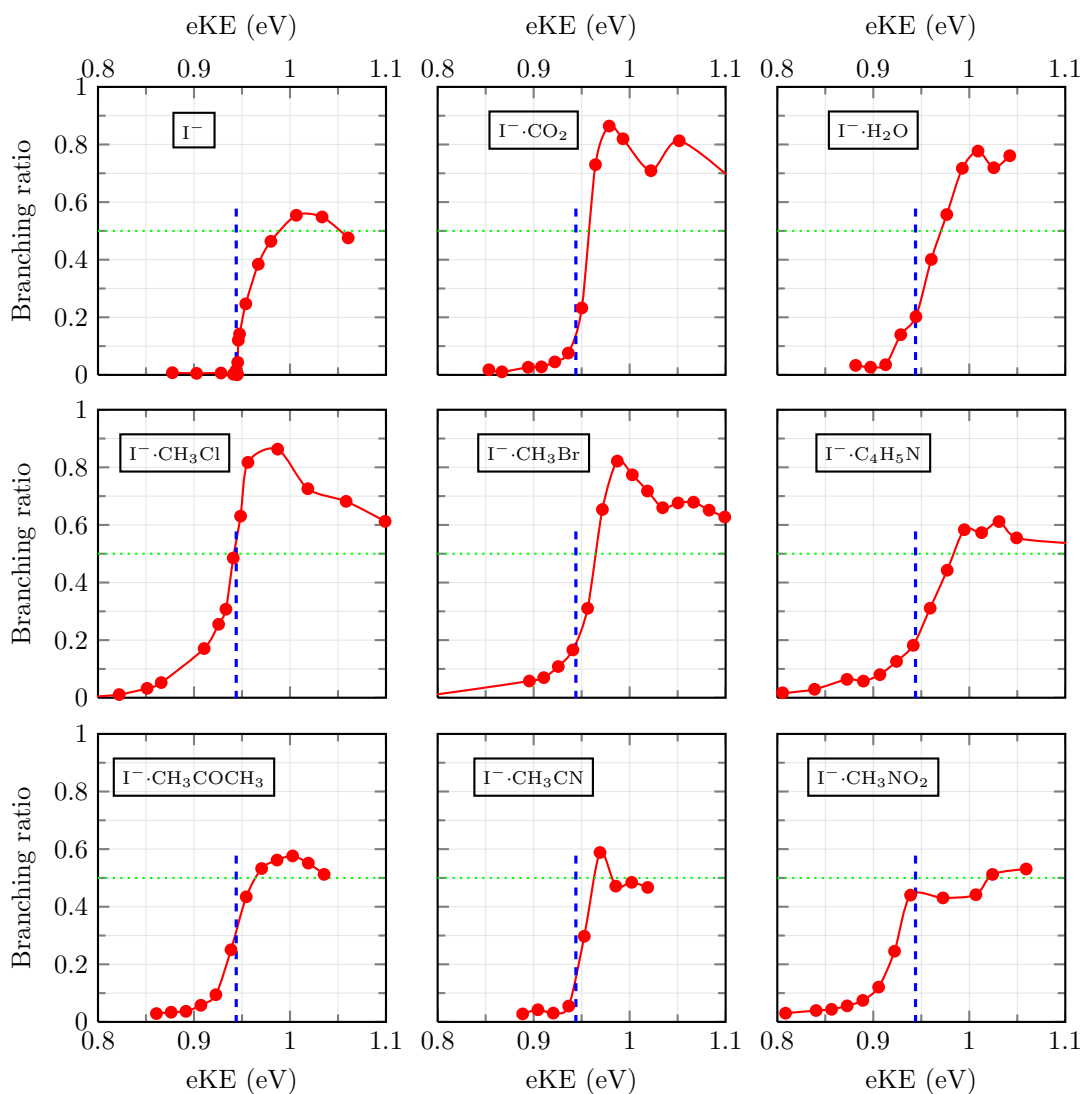
Figure 4.7: Channel branching ratios $[\mathrm{I}(^2\mathrm{P}_{1/2}) \cdot \mathrm{Y} \colon \mathrm{I}(^2\mathrm{P}_{3/2}) \cdot \mathrm{Y}]$ for photodetachment from I^- and $\mathrm{I}^- \cdot \mathrm{Y}$. The dashed vertical lines on each plot mark the kinetic energy of $\mathrm{I}(^2\mathrm{P}_{3/2})$ channel electrons at the opening of $\mathrm{I}(^2\mathrm{P}_{1/2})$ channel. The dotted horizontal lines mark the $[\mathrm{I}(^2\mathrm{P}_{1/2}) \colon \mathrm{I}(^2\mathrm{P}_{3/2})]$ statistical branching ratio
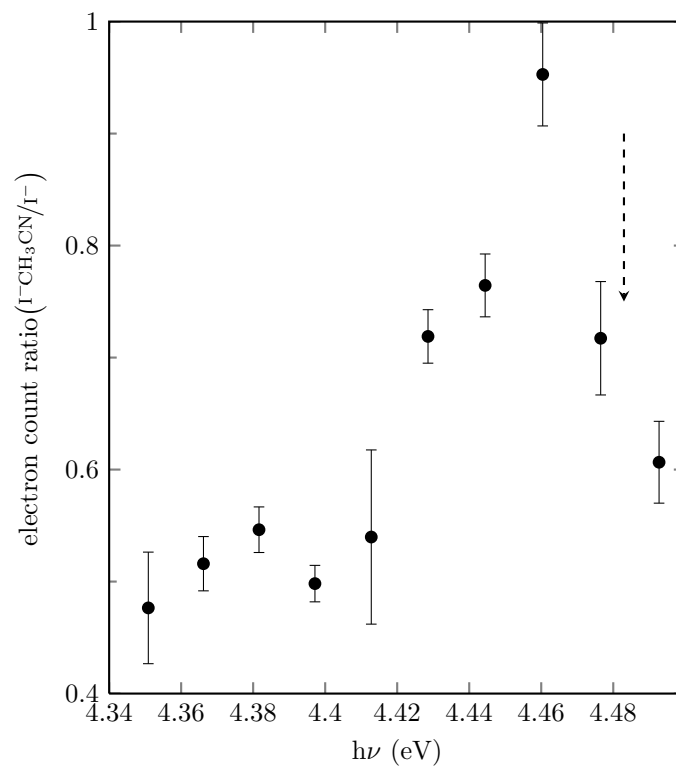
Figure 4.8: Relative photodetachment cross section $[\mathrm{I}^- \cdot \mathrm{CH_3CN}\colon \mathrm{I}^-]$ near the Channel II threshold. The arrow marks the photon energy at the vertical detachment energy for Channel II.

4.4.1 Photoelectron spectra of $I^- \cdot Y$

The similarity of the $I^- \cdot Y$ photoelectron spectra to I^- spectra is a result of the excess electron localization on the iodine atom[42, 102, 106, 122, 165, 166]. Except for minor perturbations due to the presence of the solvent molecule, the highest occupied molecular orbitals are approximately those of free I^-[42, 102, 157, 164, 166–168]. The shift to higher binding energies for the transitions was explained in Chapter 3. Therefore bands labeled I in the spectra of Figure 4.2 (and the outer rings in Figure 4.1) correspond to transitions described schematically by equation 4.3. Band II is due to transitions described by equation 4.4. Due to the atomic-like nature of the transitions in $I^- \cdot Y$, here, and for the rest of the dissertation the notation $I(^2P_{3/2}) \cdot Y$ and $I(^2P_{1/2}) \cdot Y$ to refer to the instantaneous neutral cluster produced by vertical excitation will be used. The vibrational structure in the Channel II band of $I^- \cdot CO_2$ was discussed in Chapter 3. The Franck-Condon analysis suggests that the features in $I^- \cdot CH_3CN$ and $I^- \cdot H_2O$ spectra are due to vibrational excitations of the normal modes in CH_3CN or H_2O moieties of $I \cdot CH_3CN$ and $I \cdot H_2O$. Aside from the vibrational bands in $I^- \cdot CO_2$, the weak (or absence of) vibrational excitation of the solvent normal modes suggest very small difference between the geometries of Y in $I^- \cdot Y$ and $I \cdot Y$.

4.4.2 I^- Photoelectron angular distributions

The trend in $\beta_{3/2}$ has been rationalized within the one electron dipole approximation, where the allowed photoelectron wavefunction is expressed as a superposition of angular momentum waves[122]. As already mentioned in Chapter 1 the selection rule for photodetachment is $\Delta\ell = \pm 1$. Under this selection rule, partial waves $(\ell' = \ell \pm 1)$ represent possible orbital angular momenta associated with the outgoing electron. For I^- $\ell = 1$ (p orbital) and therefore possible partial waves are $\ell' = 0$ and $\ell' = 2$. Interference between these partial waves leads to the observed $\beta(eKE)$ evolution. The interference effect on the value of β is captured by the Cooper-Zare equation (Chapter 1)[40, 130].

$$\beta = \frac{\ell\,(\ell-1)\,\sigma_{\ell-1}^2 + (\ell+1)\,(\ell+2)\,\sigma_{\ell+1}^2 - 6\ell\,(\ell+1)\,\sigma_{\ell+1}\sigma_{\ell-1}\cos\left(\delta_{\ell+1} - \delta_{\ell-1}\right)}{(2\ell+1)\left[\ell\sigma_{\ell-1}^2 + (\ell+1)\,\sigma_{\ell+1}^2\right]}$$

β therefore depends on the phase shifts(δ_0, δ_2) and partial wave cross sections(σ_0, σ_2). It was shown in Chapter 1 that the partial cross section σ_0 and σ_2 are dependent on the linear momentum k of the departing electron:

$$\sigma_{\ell'} \propto k^{2\ell'+1}$$

or, in terms of eKE,

$$\sigma_{\ell'} \propto eKE^{\ell'+1/2}$$

As the eKE changes, the relative magnitudes of σ_0 and σ_2 change and hence affect the value of β. It is clear from the partial cross section dependence on eKE that at threshold, when the eKE is low, $\ell' = 0$ will dominate the angular distributions. As eKE increases $\ell' = 2$ becomes more important.

A quick approximate quantitative guide to the expected variation in $\beta_{3/2}$ can be determined using the approximation of Hanstorp et al.[50] to the Cooper-Zare equation to obtain a quantitative evaluation of the variation of $\beta_{3/2}$ with eKE. The assumption that $\sigma_{\ell'}$ is proportional to $eKE^{\ell'+1/2}$ does not hold over the range of the the experiment. However Hanstorp et al. suggested that $\frac{\sigma_2}{\sigma_0} = A \cdot eKE$ (A is a proportionality constant) might be valid over a longer range as higher order terms might cancel. Substituting into the Cooper-Zare equation, for $\ell = 1$[50],

$$\beta = \frac{2A^2 eKE^2 - 4AeKE \cos(\delta_2 - \delta_0)}{1 + 2A^2 eKE^2} \tag{4.5}$$

A fit of the above equation to the experimental β values using A = 0.54 eKE^{-1} and $(\delta_2 - \delta_0) = 26.9$ degrees reproduces the I$^-$ β(eKE) trend fairly well as shown in Figure 4.6.

4.4.3   I$^-$·Y Photoelectron angular distributions

4.4.3.1   Origin of rapid change in the β_I(eKE) near the Channel II threshold

In section 4.4.2 it was shown that $\beta_{3/2}$ for I$^-$ photodetachment can be modeled by using the approximation of Hanstorp et al.[50] through equation 4.5. In doing so it

is assumed that the phase shift between the two partial waves ($\ell = 0$ and $\ell = 2$) is independent of the electron kinetic energy. In the case of clusters in the Channel II threshold region $\beta_I(\text{eKE})$ *cannot* be fit to this equation under this assumption. It might be argued that production of a long lived metastable state may lead to a change in the angular distribution due to reduction of laboratory and molecular frame correlation prior to electron ejection. Such a process would decrease the anisotropy, but not lead to a change in the sign of β_I as seen for $I^- \cdot CH_3CN$ and $I^- \cdot CH_3NO_2$.

Although this change in β_I occurs near the Channel II threshold, it is instructive to consider previous experiments near the threshold of Channel I. Johnson et al.[27–30] have shown, using photoneutral action spectroscopy, that the absorption cross section (σ_p) is enhanced in the vicinity of photodetachment thresholds in $I^- \cdot Y$. An example of this effect is shown in Figure 4.9 for $I^- \cdot CH_3CN$[28] where the maximum in σ_p occurs before the vertical detachment energy. The authors attributed this enhancement to the production of a dipole supported state of the form $[I(^2P_{3/2}) \cdot CH_3CN]^-$ in which the dipole moment of the neutral framework $[I(^2P_{3/2}) \cdot CH_3CN]$ is strong enough to bind an excess electron. The photoneutral action spectrum in Figure 4.9 resembles the
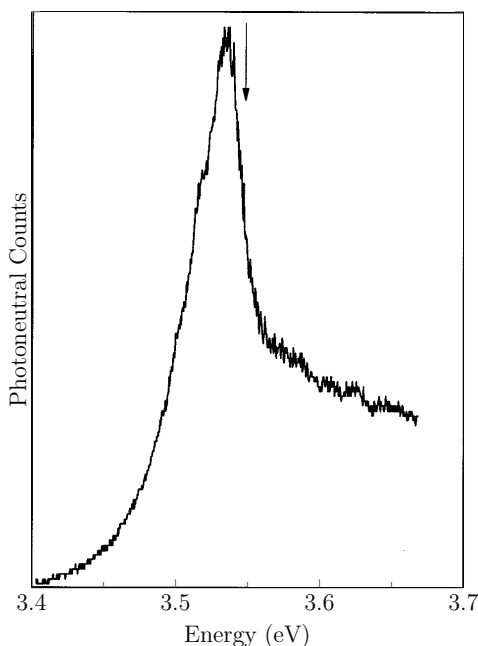
Figure 4.9: The fast photoneutral action spectrum of $I^- \cdot CH_3CN$. The arrow marks the VDE of the complex[28]. Reprinted with permission from: Dissent, C. E. H., Bailey, C. G. and Johnson, M. A., *J. Chem. Phy.* **103**, 2006, (1995). Copyright 1995, American Institute of Physics.
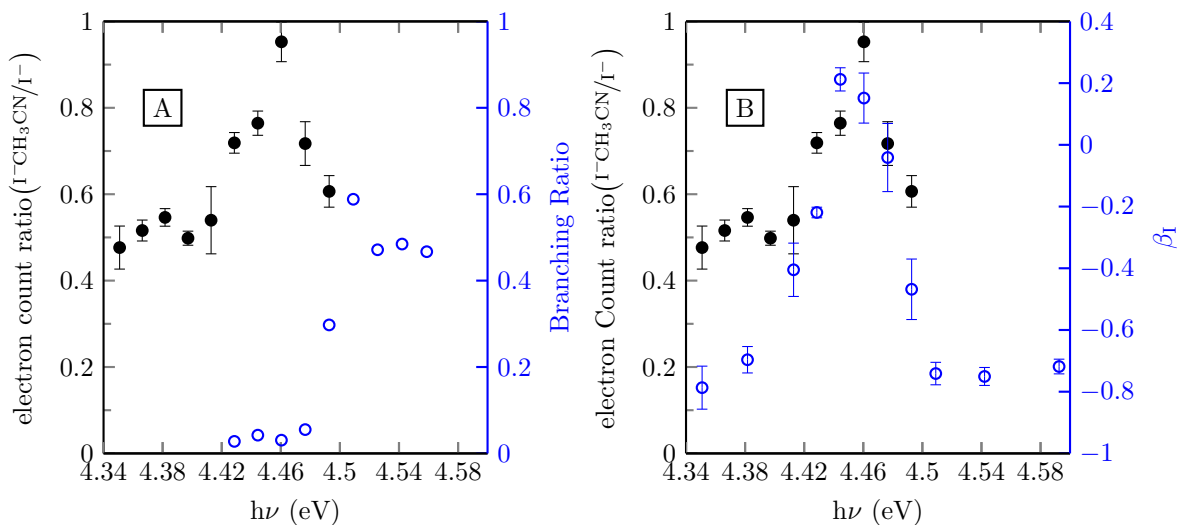
Figure 4.10: Relative photodetachment cross section $[I^- \cdot CH_3CN\colon I^-]$ (closed circles, left ordinate) and channel branching ratios (open circles, right ordinate)$[I(^2P_{3/2}) \cdot CH_3CN\colon I(^2P_{1/2}) \cdot CH_3CN]$ for photodetachment from I^- and $I^- \cdot Y$. B:Relative photodetachment cross section$[I^- \cdot CH_3CN\colon I^-]$ (closed circles, left ordinate) and $\beta_I(h\nu)$ (open circles, right ordinate)

photodetachment cross section data presented in Figure 4.8 for photodetachment near the the threshold of Channel II. This clearly suggests that there is a corresponding dipole bound state, $[I(^2P_{1/2}) \cdot CH_3CN]^-$, associated with this Channel. The maximum in the photodetachment cross section occurs before Channel II opens as shown in Figure 4.10A. Figure 4.10B shows that the maximum value of β_I in $I^- \cdot CH_3CN$ correlates with the maximum enhancement of the $I^- \cdot CH_3CN$ photodetachment cross section in this region within experimental error. It is posited therefore that the observed enhancement of β_I near the threshold of Channel II is due to the $[I(^2P_{1/2}) \cdot CH_3CN]^-$ dipole bound state.

Generalizing the results of $I^- \cdot CH_3CN$ to any cluster $I^- \cdot Y$, consider the excitation of $I^- \cdot Y$ near the opening of Channel II;

$$I^- \cdot Y \ \longrightarrow I(^2P_{3/2}) \ + Y + e^- \tag{4.6a}$$

$$\longrightarrow I(^2P_{1/2}) \ + Y + e^- \tag{4.6b}$$

$$\longrightarrow [I(^2P_{1/2}) \cdot Y]^- \longrightarrow I(^2P_{1/2}) \ + Y^- \tag{4.6c}$$

$$\longrightarrow [I(^2P_{1/2}) \cdot Y]^- \longrightarrow I(^2P_{3/2}) \ + Y + e^- \tag{4.6d}$$

73
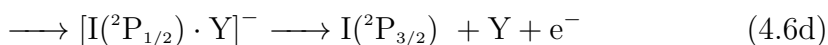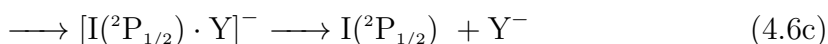
Equations 4.6a and 4.6b, equivalent to 4.3 and 4.4, represent the direct detachment processes. Near the threshold of Channel II, excitation of $I^- \cdot Y$ to the dipole supported state, $[I(^2P_{1/2}) \cdot Y]^-$, becomes increasingly important. This state can decay by formation of a dipole bound anion Y^- according to 4.6c if the dipole moment of Y is strong enough to support a dipole bound state. This method of production of the dipole bound anion Y^- was used by Bailey et al.[169] to produce CH_3CN^- near the Channel I threshold. An alternative decay route for $[I(^2P_{1/2}) \cdot Y]^-$ is relaxation of the neutral core to $[I(^2P_{3/2}) \cdot Y]^-$ accompanied by autodetachment of the excess electron (Equation 4.6d). Such a decay mechanism is not available near the threshold of Channel I. The kinetic energy of the ejected electron is equal to the difference in energy between $[I(^2P_{3/2}) \cdot Y]$ and $[I(^2P_{1/2}) \cdot Y]$ and is isoenergetic with the electron from direct detachment process 4.6a. Interference between these two channels is likely to be the reason for change in β_I measured by the experiment. Hereafter this mechanism is referred to as electronic autodetachment. Note that this mechanism of autodetachment is quite different from the one discussed in chapter 3 for $I^- \cdot C_4H_5N$ where the kinetic energy of the autodetached electron is independent of the photon energy. Based on β_I evolution, branching ratios and relative cross section data for $I^- \cdot CH_3CN$ (Figure 4.10), it is reasonable to ascribe the behavior to the decay of a dipole bound state. The results presented so far however suggest that formation of a molecular dipole bound state is not necessary for relaxation to have an effect. The calculated dipole moment of $[I \cdot CO_2]$ (see next section) at the $I^- \cdot CO_2$ equilibrium geometry is 0.39 D, far too small to support a dipole bound anion, but it is clear from Figure 4.6 that this cluster does show rapid change of β_I near Channel II threshold. The presence of the attractive dipole potential decelerates the electron's departure from $[I(^2P_{1/2}) \cdot Y]^-$ facilitating relaxation of $[I(^2P_{1/2}) \cdot Y]$ to $[I(^2P_{3/2}) \cdot Y]$ and acting as an energy bath for the excess energy.

A complimentary view is that the dipole potential facilitates the mixing of electron ejection into the continuum (via equation 4.6a). In this picture, at the instant of absorption of a photon by $I^- \cdot Y$, a complex $[e + I(^2P_{1/2}) \cdot Y]$ is formed[170]. The possibility of angular momentum exchange couples the $e + I(^2P_{3/2}) \cdot Y$ and $[e + I(^2P_{1/2}) \cdot Y]$ channels. In the language of R-matrix theory, this might represent the "inner sphere" region where angular momentum exchange with other electrons may occur[171]. The attractive dipole potential presumably results in the electron spending more time in

the inner sphere region. The complex may dissociate to $I(^2P_{3/2}) \cdot Y + e^-$ as the electron enters the continuum or "outer sphere" region, or form a molecular dipole bound state Y^- $(+ I(^2P_{3/2}))$.

In the next section, the effect of the dipole moment of Y or $[I \cdot Y]$ on the β_I anomaly near Channel II threshold will be explored quantitatively.

4.4.3.2 Correlation of dipole moments with β_I behavior

It was mentioned in Chapter 1 that dynamical parameters such as the angular distributions and total cross sections in photodetachment depend on the electron molecule long range interaction potentials. Comparison of β for $I^-(\beta_{3/2})$ and the clusters $I^- \cdot Y(\beta_I)$ suggests that the effect of the dipole potential far from the Channel II threshold is minor. $I^- \cdot CH_3I$ and $I^- \cdot CH_3Br$ are the only examples studied so far that show significantly different PADs from I^- for eKE $<$0.8 eV[42, 106, 167]. Even then, the deviation in those clusters arises from a different effect, namely, a low lying anionic σ^* resonance in the methyl halides.

The behavior of β_I near the Channel II threshold deviates from that of I^- for all the cluster anions reported here. In order to quantify this deviation, a baseline (hypothetical) may be defined by extrapolating β_I(eKE) from one side of the peak to the other. $\Delta\beta_{max}$ is then defined as the difference between the maximum value of β_I and the extrapolated β_I at the same eKE. For each $I^- \cdot Y$, $\Delta\beta_{max}$ is plotted as a function of the solvent dipole moment (μ_Y) in Figure 4.11A. Also plotted in Figure 4.11B is $\Delta\beta_{max}$ against the calculated dipole moment of $[I \cdot Y](\mu_{I \cdot Y})$ at the equilibrium geometry of $I^- \cdot Y$. These dipole moments were calculated using Gaussian 03 as described in experimental section of Chapter 3 and represent the dipole moment experienced by the electron as a result of a verical transition. μ_Y and $\mu_{I \cdot Y}$ are shown in Table 4.3.

Table 4.3: Experimental dipole moments of the solvents Y (μ_Y)[108] and those calculated for $[I \cdot Y](\mu_{I \cdot Y})$ at the equilibrium geometry of $I^- \cdot Y$.

Y	CO_2	C_4H_5N	CH_3Br	H_2O	CH_3Cl	$(CH_3)_2CO$	CH_3NO_2	CH_3CN
μ_Y (D)	0	1.77	1.82	1.85	1.89	2.88	3.46	3.92
$\mu_{I \cdot Y}$ (D)	0.39	2.69	2.49	2.46	2.47	3.85	4.58	4.54
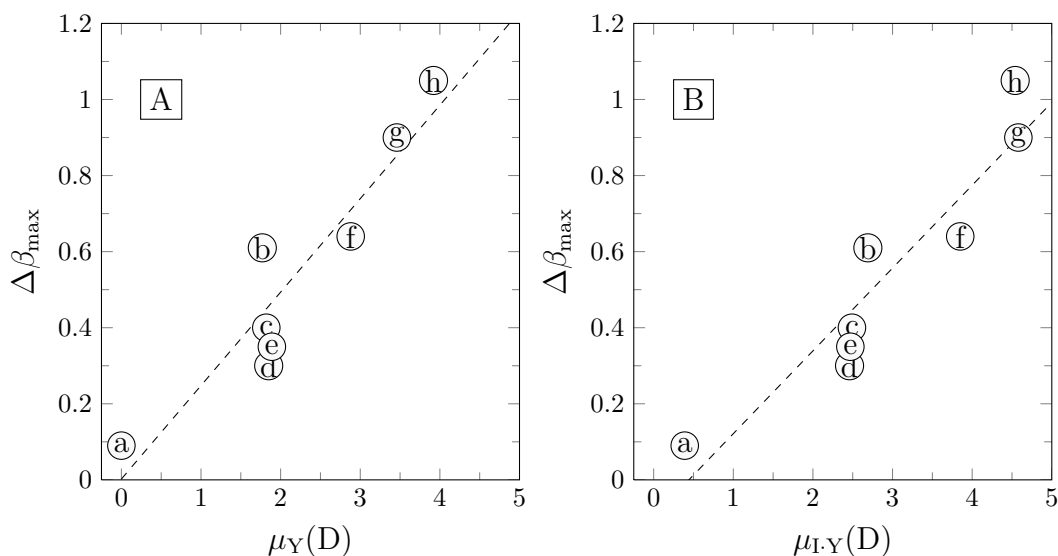
Figure 4.11: Correlation between dipole moment and $\Delta\beta_{max}$ in $I^- \cdot Y$ photodetachment($Y=CO_2$(a), C_4H_5N(b), CH_3Br(c), H_2O(d), CH_3Cl(e), $(CH_3)_2CO$(f), CH_3NO_2(g) and CH_3CN(h)). In A the experimental dipole moments values[108] of the solvents (μ_Y) are used. In B dipole moment value of $I \cdot Y$ ($\mu_{I\cdot Y}$) at the equilibrium geometry of $I^- \cdot Y$ is used.

As can be seen from Figure 4.11A, there is a linear correlation between μ_Y and $\Delta\beta_{max}$ (correlation coefficient=0.93) and $\mu_{I\cdot Y}$ and $\Delta\beta_{max}$ (correlation coefficient=0.94). Since it is the dipole moment of the neutral cluster [I·Y] that affects overall dynamics, only $\mu_{I\cdot Y}$ should be crucial here. The strong correlation between μ_Y and $\Delta\beta_{max}$ results from a similarly strong correlation between μ_Y and $\mu_{I\cdot Y}$. Due to the limits of the value of β ($2 \geq \beta \geq -1$) this degree of correlation presumably will not be maintained at much higher values of $\mu_{I\cdot Y}$, but the relationship is remarkably linear for the cluster anions studied here.

With the exception of [I·CO$_2$], all the neutral clusters [I·Y] studied have dipole moment values that can support a dipole bound anion. The increase in $\Delta\beta_{max}$ with $\mu_{I\cdot Y}$ is therefore a result of stronger interaction between the electron and [I·Y]. Stronger interaction results in a longer lived [I·Y]$^-$ which results in enhanced autodetachment via 4.6d. This interpretation is further supported by the measured branching ratios (Channel II:Channel I) in Figure 4.7. The molecular moieties of the cluster anions in category 2 ($I^- \cdot CH_3CN$, $I^- \cdot CH_3COCH_3$ and $I^- \cdot CH_3NO_2$) form stable dipole bound states. Furthermore the dipole bound states associated with the cluster framework

lie below the Channel II threshold. Relaxation accompanied by electronic autode-tachment (4.6d) is still possible. However, production of free $I(^2P_{1/2})$ by 4.6b is not energetically possible due to energy conservation. For category 1 cluster anions, the dipole bound states lie energetically close to Channel II threshold and competition between 4.6d and $[I(^2P_{1/2}) + Y + e^-]$ becomes important, leading to enhanced $I(^2P_{1/2})$ production relative to the category 2 cluster case. $I^- \cdot C_4H_5N$ is intermediate between these two extremes perhaps due to its relatively large $\mu_{I \cdot Y}$ compared to category 1.

It is concluded that for photodetachment near the Channel II threshold, an increase in dipole moment favors electronic autodetachment via relaxation (equation 4.6d) while the channel branching ratio enhancement is favored by lower values of the cluster dipole moment. The presence of the dipole moment enhances the absorption cross section which for category cluster anions produces a temporary excited state that may decay by either pathway.

4.4.3.3   Parallels with Rydberg atom autoionization

Dipole bound anions have been likened to Rydberg states in neutral atoms[144, 172]. Xenon, which is isoelectronic with I^-, has five interacting Rydberg series, two of which arise from the excitation of an electron in a 5p orbital to an $ns_{1/2}$ or $nd_{1/2}$ state and converge to the $Xe^+ \left(5^2P_{1/2}\right)$ state[173–175]. These two series lie in the contin-uum above the threshold of ionization to the $5^2P_{3/2}$ state. Relaxation (mediated by the Rydberg states) of $5^2P_{1/2}$ to $5^2P_{3/2}$ followed by electron ejection is possible[175]. Such autoionization resonances enhance the photoionization cross section near the $Xe^+ \left(5^2P_{1/2}\right)$ threshold and also manifest themselves as rapid changes in the pho-toionization angular distributions[173–175]. There are no Rydberg states in anions due to the absence of a Coulombic electron-cation interaction as in the case of pho-toionization. The dipole moment seems to play a similar role in photodetachment of $I^- \cdot Y$. However the effect is more complicated in $[I \cdot Y]^-$ because of the presence of more degrees of freedom, possible fragmentation of the cluster upon photoexci-tation, anisotropic electron-molecule interaction potentials etc. Autoionization has been studied theoretically using close coupling R-matrix methods[171, 176, 177] and the relativistic random phase approximation[175, 178, 179]. It would be interesting to apply these methods to cluster anions of the type studied here in order to study

channel coupling in the presence of dipole potentials. Note that the $\beta_{3/2}(\text{eKE})$ for I^- also seems to show a small step at photon energies corresponding to the $I(^2P_{1/2})$ channel opening perhaps showing the onset of channel mixing even in I^- detachment. Experiments to quantify this effect and extend the study to Br^- and Cl^- are currently underway in our laboratory.

4.5   Summary

A detailed study of the photoelectron spectra and angular distributions for $I^- \cdot Y$ photodetachment near the threshold of Channel II transitions has been performed. Weak vibrational excitation of the internal bending mode of H_2O in $I^- \cdot H_2O$ and the CH_3 rocking mode of CH_3CN in $I^- \cdot CH_3CN$ are observed. The excitations are consistent with Franck-Condon expectations. Near the Channel II threshold, β_I is strongly correlated with dipole moment of the neutral cluster $[I(^2P_{1/2}) \cdot Y]$ accessed by vertical excitation from $I^- \cdot Y$. The effect is explained in terms of autodetachment from a dipole supported state $[I(^2P_{1/2}) \cdot Y]^-$ as the neutral core relaxes to $[I(^2P_{3/2}) \cdot Y]$. Direct detachment via channels I and II compete with this autodetachment. For lower cluster dipole moment values $\mu_{I \cdot Y}$, the proximity of the weakly bound $[I(^2P_{1/2}) \cdot Y]^-$ state to the channel II threshold enhances absorption, leading to bias in favor of electron loss into channel II. For such cluster anions an enhanced channel branching ratio is observed. As $\mu_{I \cdot Y}$ increases the dipole bound state shifts below the threshold and production of $I(^2P_{1/2}) + Y + e^-$ becomes energetically inaccessible. Consequently enhancement of the absorption cross section in the vicinity of the excited state cannot translate to the channel II cross section and the branching ratio consequently decreases.

Chapter 5

Photodetachment from di- and tri-solvated iodide clusters: $\mathrm{I^- \cdot (H_2O)_{\mathit{n}}}$ ($\mathit{n} = 2, 3$) and $\mathrm{I^- \cdot (CH_3CN)_2}$
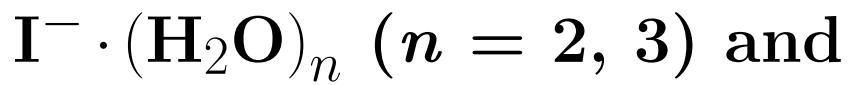
5.1 Introduction

In Chapter 4, the effect of the dipole potential on photodetachment from monosolvated $\mathrm{I^-}$ cluster anions was studied. The results showed that in the vicinity of Channel II, the behavior of the photoelectron angular distributions is strongly influenced by the dipole moment of the neutral cluster formed by vertical detachment ($\mu_{\mathrm{I \cdot Y}}$). In this chapter the investigation will be extended to study the effect of the dipole moment on photodetachment dynamics to doubly and triply solvated clusters containing acetonitrile ($\mathrm{I^- \cdot (CH_3CN)_2}$) and water ($\mathrm{I^- \cdot (H_2O)_2}$ and $\mathrm{I^- \cdot (H_2O)_3}$). The different channels available following photoexcitation of $\mathrm{I^- \cdot Y}$ were presented in Chapter 4. Generalizing

to multisolvated iodide cluster anions, these may be represented schematically as;

$$I^-\cdot(Y)_n \longrightarrow I(^2P_{3/2}) + (Y)_n + e^- \tag{5.1a}$$

$$\longrightarrow I(^2P_{1/2}) + (Y)_n + e^- \tag{5.1b}$$

$$\longrightarrow [I(^2P_{1/2})\cdot(Y)_n]^- \longrightarrow I(^2P_{1/2}) + (Y)_n^- \tag{5.1c}$$

$$\longrightarrow [I(^2P_{1/2})\cdot(Y)_n]^- \longrightarrow I(^2P_{3/2}) + (Y)_n + e^- \tag{5.1d}$$

$$\longrightarrow [I(^2P_{1/2})\cdot(Y)_n]^- \longrightarrow I(^2P_{1/2}) + (Y)_n + e^- \tag{5.1e}$$
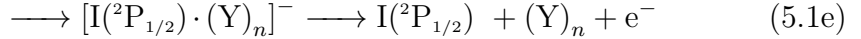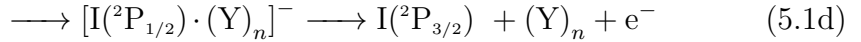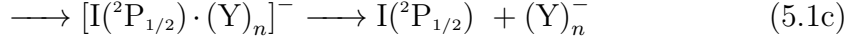
The intrinsic relationship between the PAD and the dipole moment of the neutral cluster ($\mu_{I\cdot Y}$) may be exploited in studying photodetachment from multisolvated iodide clusters. Since the overall cluster dipole moment depends on how solvent molecules arrange themselves in a cluster, different conformers are expected to show different trends in the PAD evolution with the electron kinetic energy.

For multi-solvated iodide cluster anions, the loosely bound electron can also be trapped within the solvent network (solvated electron) rather than bound by the dipole field of a single molecule[180]. Thus the presence of both dipole bound and solvated electron states adds another layer of complication.

There has been considerable theoretical and experimental interest[30, 141, 147, 150, 157, 181] in $I^-\cdot(H_2O)_n$ clusters. The dipole moment of the neutral clusters, $I\cdot(H_2O)_n$ ($n = 1$–4), at the equilibrium geometry of $I^-\cdot(H_2O)_n$ increases with n[30]. Therefore it is interesting to see if the correlation between $\Delta\beta_{max}$ and $\mu_{I\cdot Y}n$ holds for these clusters as well. Femtosecond time resolved studies for $I^-\cdot(H_2O)_n$ ($n = 3$–10) have shown that the excited states of cluster anions, $[I(^2P_{3/2})\cdot(H_2O)_n]^-$, undergo a simple exponential decay ($n = 3, 4$) or rearrange to stabilize the cluster before decaying ($n = 5$-10)[144, 147]. This rearrangement may also affect the magnitude of $\Delta\beta_{max}$ if the timescale of rearrangement is comparable to the electronic autodetachment timescale. Although all these studies have been concerned with photoexcitation near the Channel I threshold, it is reasonable to believe that the dynamics are similar for Channel II except the autodetachment induced by spin-orbit relaxation as discussed in chapter 4.

5.2 Experimental

In general, preparation of the multi-solvated cluster anions is similar to that of the corresponding monomers (Chapters 3 and 4). The discharge source was used for all the multisolvated clusters. Dilute CH_3I ($\sim 5\%$ in Ar) at 10-80 psi stagnation pressure is bubbled through liquid acetonitrile or water. Details of the supersonic expansion, discharge unit, anion separation and detection were given in Chapter 2. Molecular geometries of the cluster anions were calculated using the basis sets described in Chapter 3. The geometries of $I^- \cdot (CH_3CN)_2$ are based on those initially calculated by Timerghazin et al.[182].

5.3 Results

5.3.1 Photoelectron spectra

Photoelectron images were collected for $I^- \cdot (CH_3CN)_2$ and $I^- \cdot (H_2O)_n$ ($n = 2, 3$) for wavelength ranges covering Channel I and II transitions. Wavelength steps of 1 nm in the vicinity of the Channel II threshold and 2-5 nm away from thresholds were used. Representative raw photoelectron images (no BASEX[95] transformation performed) and spectra obtained from transformed images are shown in Figures 5.1 and 5.2. Although photoelectron spectra of these anions have been reported before[28, 30, 140, 141, 147], they are repeated here since source conditions can influence spectra. The spectra are reminiscent of the monosolvated iodide spectra discussed in the previous chapter. At 247 nm Channels I and II are accessible for $I^- \cdot (CH_3CN)_2$ and $I^- \cdot (H_2O)_2$, while energy considerations restrict us to Channel I for $I^- \cdot (H_2O)_3$. The two channels are separated by ~ 0.94 eV the spin orbit splitting of atomic iodine. The transitions occur at higher binding energies than the monosolvated clusters as expected due to increased solvent stabilization. The experimental vertical detachment energies for $I^- \cdot CH_3CN$ and $I^- \cdot (CH_3CN)_2$ are 3.54 and 3.99 eV respectively. The solvation energies (with respect to free I^-) are 0.48 and 0.93 eV respectively for $I^- \cdot CH_3CN$ and $I^- \cdot (CH_3CN)_2$. For $I^- \cdot H_2O$, $I^- \cdot (H_2O)_2$, and $I^- \cdot (H_2O)_3$, the vertical detachment energies are 3.55, 3.92 and 4.23 eV respectively, representing
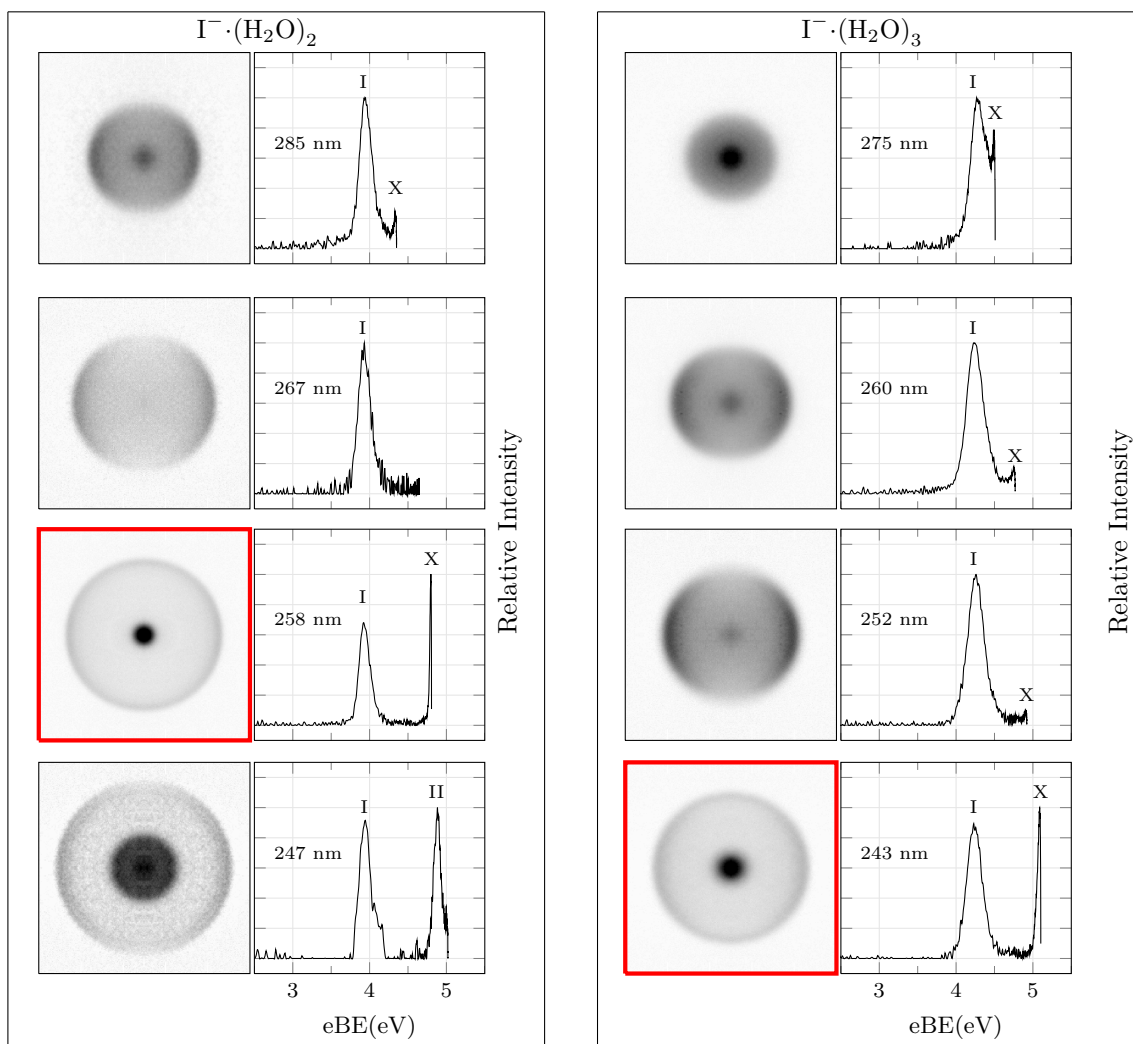
Figure 5.1: Selected photoelectron spectra of $I^- \cdot (H_2O)_n$ ($n = 2\text{--}3$) at different wavelengths. Images marked with a red boundary correspond to the maximum value of β_I.
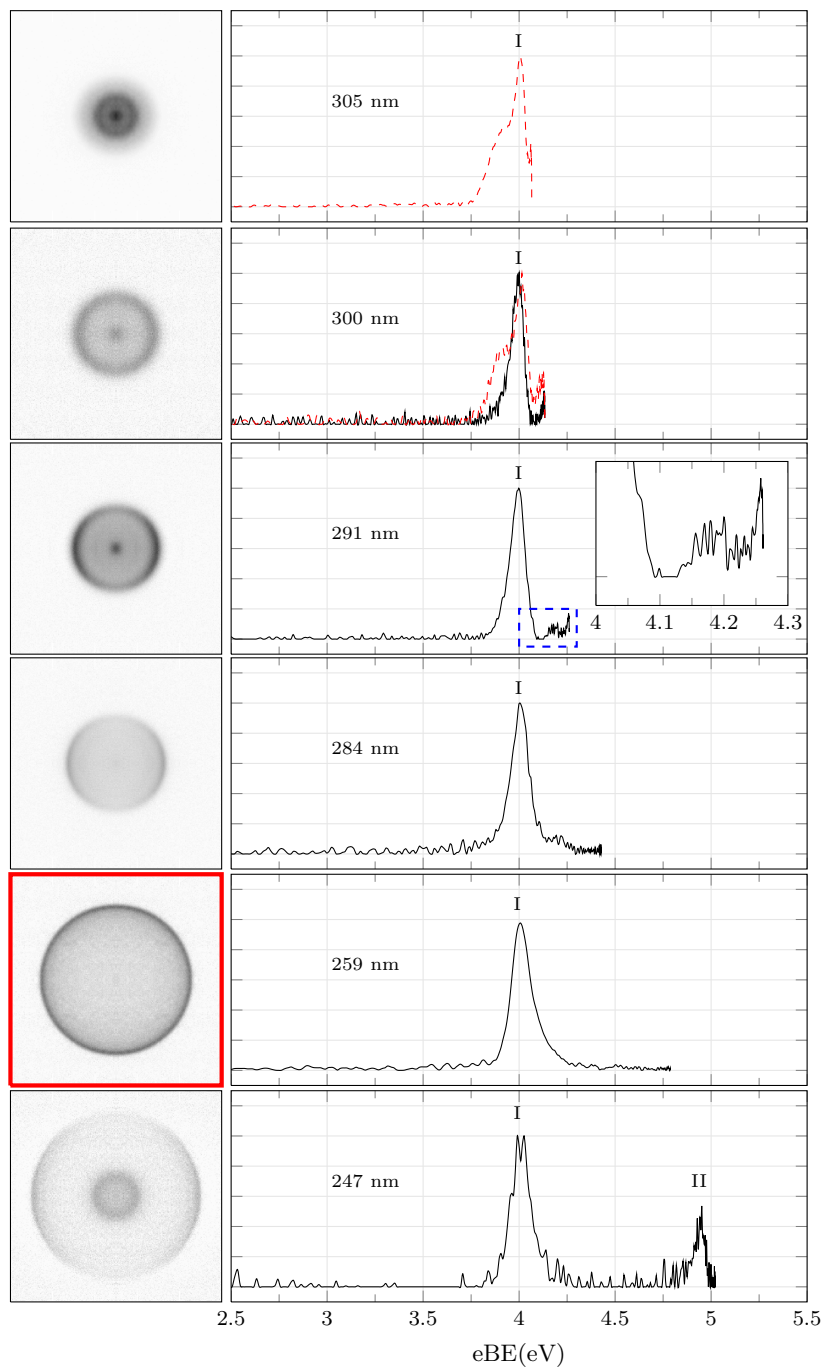
Figure 5.2: Selected photoelectron spectra of $I^- \cdot (CH_3CN)_2$ at different wavelengths. The 259 nm image corresponds to the maximum value of β_I. The insert on the 291 nm image is a zoom in of the marked region of the main spectrum.

solvation energies of 0.49, 0.86 and 1.17 eV.

Beside the direct detachment channels, $I^- \cdot (H_2O)_2$ and $I^- \cdot (H_2O)_3$ show another transition labeled X with a vertical detachment energy that is dependent on the photon energy. This signifies an indirect detachment process (low eKE autodetachment) from an intermediate excited state. In $I^- \cdot (H_2O)_2$, this feature is strongest at photon energies similar to the vertical detachment energy for Channel I and becomes weaker as the photon energy is increased. The 267 nm image of this cluster shows no evidence of this feature but it reappears at 264 nm and becomes stronger as the Channel II threshold is approached. The $I^- \cdot (H_2O)_2$ spectrum at 247 nm shows evidence of low eKE autodetachment beyond the Channel II vertical detachment energy. Autodetachment persists at all wavelengths for $I^- \cdot (H_2O)_3$ down to 242 nm. In this case the persistence of autodetachment beyond Channel II could not be ascertained because wavelengths shorter than 242 nm are beyond the current capability of our laser system.

The photoelectron spectra of $I^- \cdot (CH_3CN)_2$ (Figure 5.2) also show the autodetachment feature but only in the vicinity of the Channel I threshold. On closer inspection, the 291 nm spectrum (insert) shows another feature lying $\sim$180 meV above the band I origin. Based on this separation, this peak is tentatively assigned to the CH_3 deformation mode of CH_3CN discussed in the previous Chapter.

In Figure 5.2, the spectra plotted using solid lines were obtained at relatively low stagnation pressures for the ion source (10-20 psig). At higher stagnation pressures (40-80 psig) a new feature emerges at lower electron binding energies than the major band I origin as shown in the spectra of the cluster anion at 305 and 300 nm (spectra plotted using dashed lines). Due to the dependence of this feature on the anion source conditions, it is suggested that its origin is due to a different conformer of $I^- \cdot (CH_3CN)_2$.

5.3.2   Calculated molecular geometries of the cluster anions

To examine the correlation between $\Delta\beta_{max}$ and the dipole moment as in Chapter 4, equilibrium geometries of the cluster anions were calculated. Molecular geometries of $I^- \cdot (CH_3CN)_n$ and $I^- \cdot (H_2O)_n$ are shown in Figure 5.3. The dipole moments of the corresponding neutral clusters at the anion equilibrium geometry are shown in

Table 5.1. The three $I^-\cdot(CH_3CN)_2$ conformers, initially identified by Timerghazin et al.[182], are the symmetric conformer (I), the head-to-tail conformer (II) and the asymmetric conformer (III). III is the global minimum with I and II lying 94 meV and 276 meV higher in energy respectively.
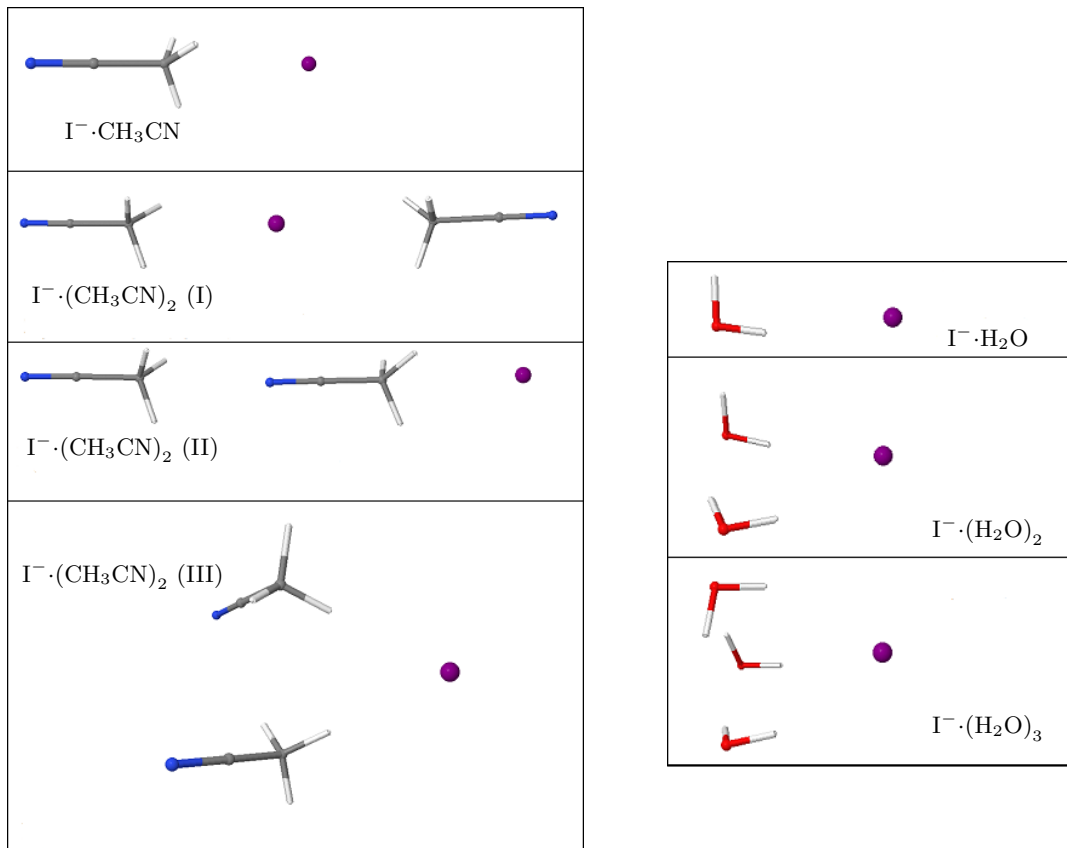
Figure 5.3: *Ab initio* geometries of $I^-\cdot(CH_3CN)_n$ and $I^-\cdot(H_2O)_n$ calculated at the MP2 level of theory.

5.3.3 Photoelectron angular distributions

Photoelectron angular distributions were also extracted as described in Chapter 2. As in Chapters 3 and 4 the β values reported here are for electrons associated with the Channel I transition at a given photon energy. Thus the label β_I is used as in chapter 4. $\beta_I(eKE)$ evolution for $I^-\cdot(CH_3CN)_n$ ($n = 1,2$) and $I^-\cdot(H_2O)_n$ ($n = 1–3$)

Table 5.1: Anisotropy data, calculated dipole moments for $I^-\cdot(CH_3CN)_n$ and $I^-\cdot(H_2O)_n$ clusters.

	n	Cluster μ D	$\beta_{\max}$	$\Delta\beta_{max}$	eKE[$\beta_{\max}$] eV
$I^-\cdot(CH_3CN)_n$	1	4.54	0.17	0.95	0.91
	2	0.3(I)	-0.03	0.89	0.79
		9.7(II)			
		5.7(III)			
$I^-\cdot(H_2O)_n$	1	2.5	-0.50	0.36	0.94
	2	4.1	-0.25	0.57	0.90
	3	4.4	-0.40	0.41	0.86
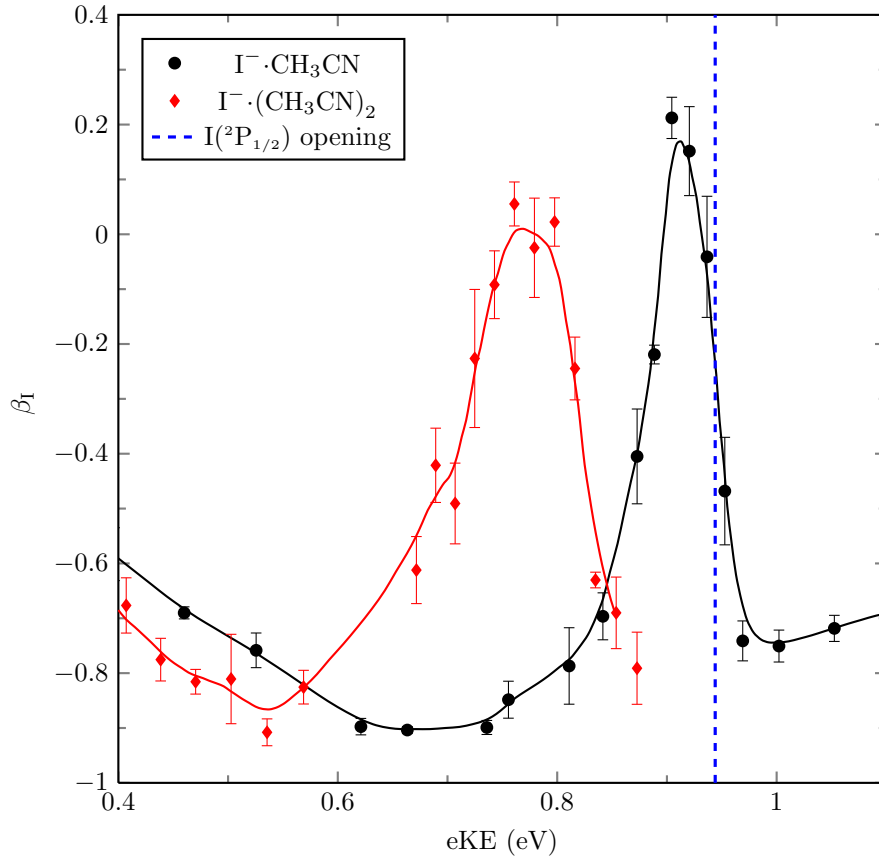
Figure 5.4: The evolution of β_I with eKE near Channel II threshold for $I^-\cdot(CH_3CN)_n$ (n=1-2). Solid lines provided as a guide to the eye.
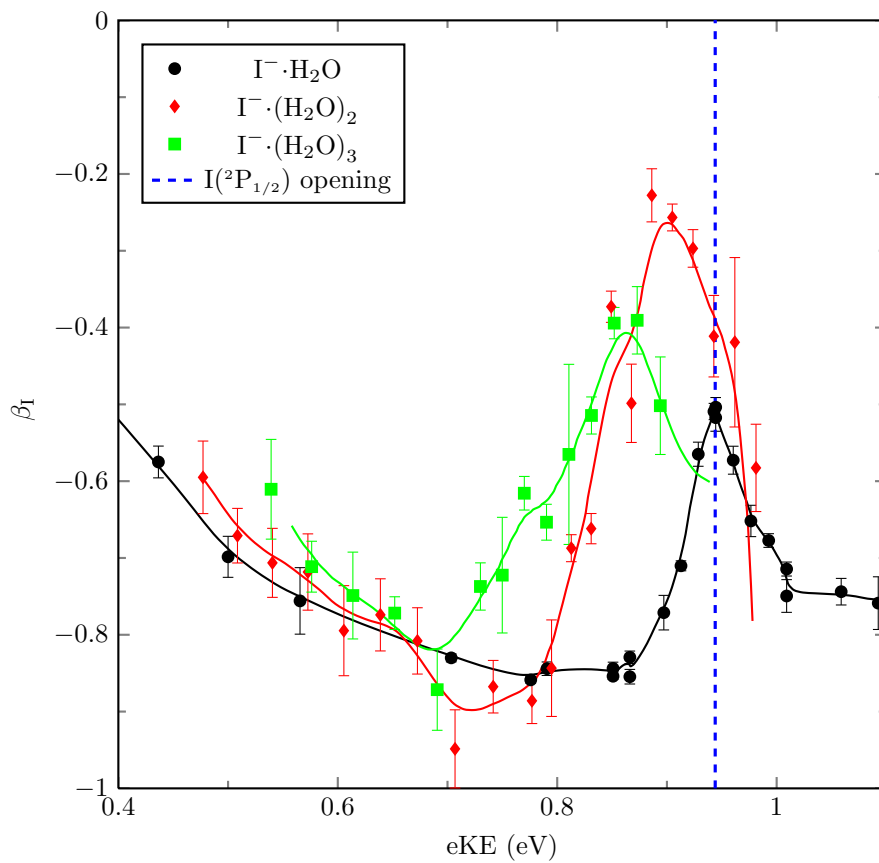
Figure 5.5: The evolution of β_I with eKE near Channel II threshold for $I^- \cdot (H_2O)_n$ (n=1-3). Solid lines provided as a guide to the eye.

are shown in Figures 5.4 and 5.5 respectively. The trend for the angular distributions for the multisolvated cluster anions is generally similar to the monosolvated iodide cluster anions. A few hundred meV below the Channel II vertical detachment energy, the value of β_I starts increasing and reaches a maximum before going down again. Table 5.1 summarizes the eKE and values of maximal β_I (β_{max}) and $\Delta\beta_{max}$ (as defined in Chapter 4) for the multisolvated iodide clusters together with those of the monosolvated iodide cluster anions presented in Chapter 4. Clearly the peaks in β_{max} for the doubly solvated cluster anions in both systems are shifted to lower electron kinetic energies than the monomers. $\Delta\beta_{max}$ for $I^- \cdot (H_2O)_2$ is also higher than that for $I^- \cdot H_2O$. In the case of $I^- \cdot (CH_3CN)_2$ there is a slight decrease in the value of $\Delta\beta_{max}$ compared to $I^- \cdot CH_3CN$. For $I^- \cdot (H_2O)_3$, despite β_I beginning to rise much earlier than that of $I^- \cdot (H_2O)_2$, the $\Delta\beta_{max}$ value is lower and appears at a slightly lower eKE.

5.4 Discussion

5.4.1 Photoelectron spectra

With the exception of band X, the photoelectron spectra of $I^- \cdot (H_2O)_n$ are very similar to the I^- spectra. Our calculated anion geometries and dipole moments for the neutral clusters agree with those previously calculated by Lee and Kim[163].

There are two potential sources of the low eKE autodetachment signal X. Photoexcitation of $I^- \cdot (H_2O)_n$ cluster anions may lead to formation of $[I \cdot (H_2O)_n]^-$ which may fragment, resulting in autodetachment to yield the X band. Alternatively, $[I \cdot (H_2O)_n]^-$ may fragment before autodetachment resulting in formation of metastable states based on solvent network only, $(H_2O)_n^-$. These may undergo further fragmentation, but on a longer timescale, subsequently leading to autodetachment. Although bound states based on the solvent network, $(H_2O)_2^-$ and $(H_2O)_3^-$ have been reported[183–185], previous experiments have shown that autodetachment from $[I(^2P_{3/2}) \cdot (H_2O)_3]^-$ occurs before the iodine atom leaves the cluster[147]. Therefore it is unlikely that band X is due to rearrangements which lead to $(H_2O)_2^-$ or $(H_2O)_3^-$. The conclusion is that band X is due to autodetachment from a dipole-supported state of the type $[I \cdot (H_2O)_n]^-$[147]. This autodetachment signal is similar to the one discussed for $I^- \cdot C_4H_5N$ in Chapter 3. The autodetachment is probably due to the binding energy

becoming too small as low dipole moment geometries are sampled along the dissociation coordinate. Time evolution of dipole moments of $[I \cdot (H_2O)_n]$ ($n = 2$–5) following photodetachment from $I^- \cdot (H_2O)_n$ was recently predicted by Kołaski et al.[150] using *ab initio* molecular dynamics calculations. Their results (Figure 5.6) show that following photoexcitation of $I^- \cdot (H_2O)_3$, the dipole moment of the corresponding neutral core, $I \cdot (H_2O)_3$, drops to ~3 D (which brings it to below that of $I \cdot (H_2O)_2$) within 100 femtoseconds before rising and staying above that of $I \cdot (H_2O)_2$. However, their calculations do not predict a such a fluctuation in the dipole moment of $I \cdot (H_2O)_2$ for the first 800 femtoseconds.

The possible existence of different conformers of $I^- \cdot (CH_3CN)_2$ complicates the in-
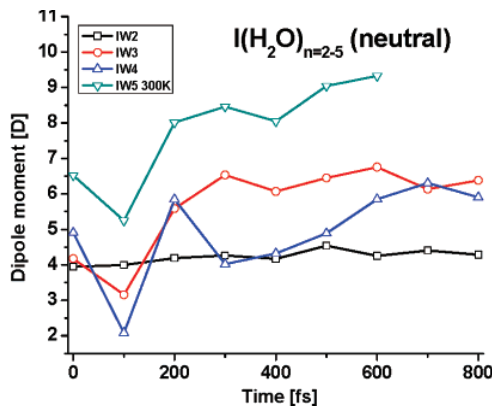
Figure 5.6: Time evolution of the dipole moment for $[I \cdot (H_2O)_n]$ ($n = 2$–5) clusters. Reprinted with permission from: Kołaski, M., Lee, H. M., Pak, C. and Kim, K. S., *J. Am. Chem. Soc.* **130**, 103, (2008). Copyright 2008, American Chemical Society.

terpretation of the spectra of this cluster anion. With the exception of the dashed spectra in Figure 5.2, all our spectra are consistent with the presence of only one conformer. The appearance of a second spectral band only at higher stagnation pressure suggests existence of two conformers, the presence of which depends on the ion source conditions. Due to possibility of these different conformers, the assignment of spectral features in the photoelectron spectrum of this cluster anion has been a subject of debate, particularly concerning the role of conformer II (the head-to-tail conformer) on the photochemistry of $I^- \cdot (CH_3CN)_2$[28, 182]. This issue will be discussed in Section5.4.2.1.

The low energy autodetachment feature near the Channel I threshold for $I^- \cdot (CH_3CN)_2$ photodetachment and its absence near the Channel II threshold is rather surprising. Since CH_3CN can bind an electron by its dipole field, it was expected that no low eKE autodetachment should be observed for this cluster. One reason for the absence of this feature near the Channel II threshold is competition with spin-orbit induced relaxation (Channel 5.1e), discussed in the previous chapter. However, the cluster environment may also give rise to a plausible explanation. An important difference between Channel I and Channel II is that associated with Channel I are two neutral states which both asymptotically correlate to $I(^2P_{3/2}) + (CH_3CN)_2 + e^-$ following photodetachment. These are similar to the states discussed in Chapter 3 for $I^- \cdot C_4H_5N$ photodetachment arising from the anisotropic interaction of the iodine 5p orbitals with the pyrrole molecule. Of the neutral clusters formed via detachment of the three $I^- \cdot (CH_3CN)_2$ conformers, *ab initio* calculations[182] suggest that the degeneracy of the I p orbitals which lie perpendicular to the van der Waals bond axis is only significantly lifted in the asymmetric conformer III. Each resultant neutral state has a corresponding dipole-bound anion state. Figure 5.7 represents a sketch of the potential energy along the dissociation coordinate for both the dipole bound states and the neutral cluster states. Based on available literature for a number of dipole-bound anions and solvated iodine clusters, typical separations between the neutral states (I_A and I_B in Figure 5.7)[21, 105, 166, 186] are of the order of the binding energies of dipole-bound anions ($DBS(I_A)$ and $DBS(I_B)$)[66]. Assuming such a case for the present cluster anion, electron loss from the dipole bound states due to interaction with the neutral surfaces is possible. Particularly important is the interaction between the states labelled I_A and $DBS(I_B)$. Such an interaction will not be available near Channel II threshold because there is only a single neutral surface. Our photoelectron spectra do not show the splitting of the lower energy neutral state presumably due to our spectral resolution.

5.4.2 Photoelectron angular distributions

The results presented above reveal interesting differences and similarities in the photoelectron angular distributions of mono and multisolvated iodide cluster anions. The
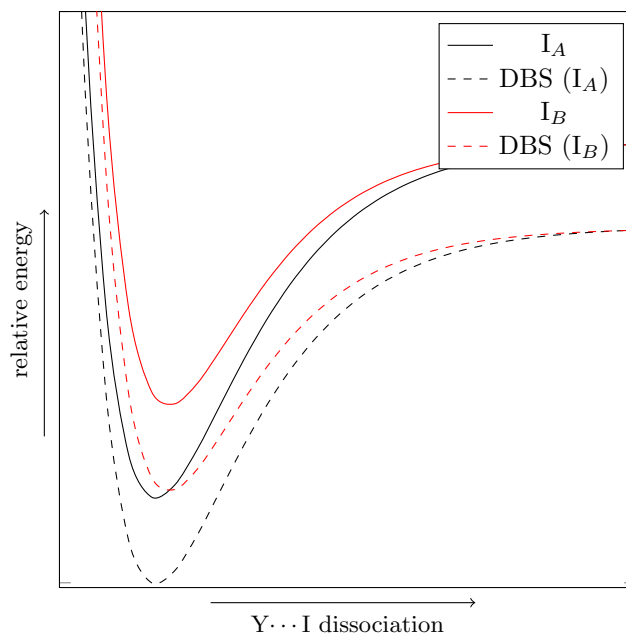
Figure 5.7: Sketches of the possible potential energy curves for $[\text{I}\cdot(\text{CH}_3\text{CN})_2]^-$ and $\text{I}\cdot$ $(\text{CH}_3\text{CN})_2$ near Channel I. The solid lines (I_A and I_B) are the neutral states and the dashed lines(DBS(I_A) and DBS(I_B)) are the dipole bound states associated with each neutral state.
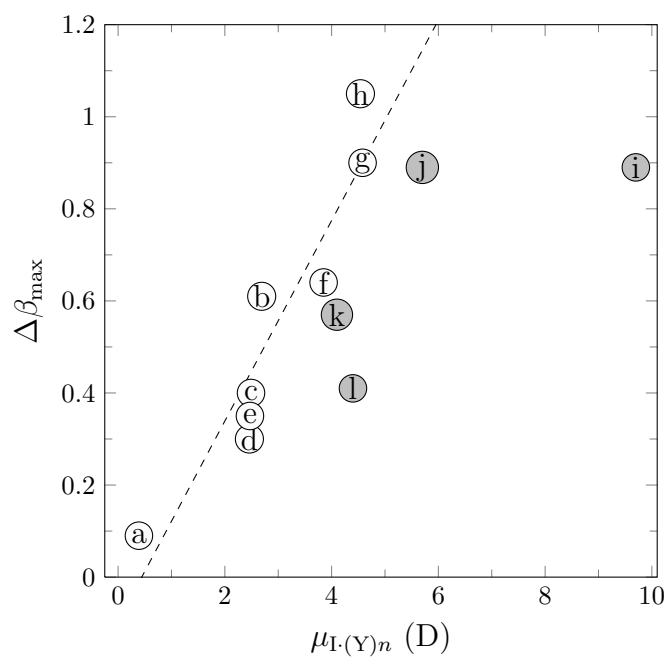
Figure 5.8: Correlation between dipole moment and $\Delta\beta_{max}$. Open circles represent values for I·Y (Y =CO_2 (a), C_4H_5N (b), CH_3Br (c), H_2O (d), CH_3Cl (e), $(CH_3)_2$ CO (f), CH_3NO_2 (g) and CH_3CN (h)). Closed circles represent multisolvated iodide clusters $[I·(CH_3CN)_2]$(head-to-tail) (i),$[I·(CH_3CN)_2]$(asymmetric) (j), $[I·(H_2O)_2]$ (k) and $[I·(H_2O)_3]$ (l). The dashed line is a linear fit to I·Y data only

behavior of the PADs near the threshold of the excited spin-orbit state of the neutral cluster, $I(^2P_{1/2}) \cdot (Y)_n$, can be explained (as in Chapter 4) in terms of iodine atom relaxation based electronic autodetachment from a dipole bound state, $[I(^2P_{1/2}) \cdot (Y)_n]^-$, which lies just below the excited neutral surface. The change in the anisotropy is due to interference between electrons from the direct detachment mechanism via Channel I and the electronic autodetachment mechanism following spin-orbit relaxation of the iodine atom in the neutral core. Such behavior leads to an increase in the Channel I total cross section and changes in the differential cross section. For monosolvated iodide cluster anions the differences in the photoelectron angular distributions between solvent molecules Y were attributed to differences in dipole moments of $I(^2P_{1/2}) \cdot Y$. $\Delta\beta_{max}$ for monosolvated iodide cluster anions was shown to be linearly correlated to $\mu_{I \cdot Y}$, the dipole moment of the neutral cluster at the equilibrium geometry of $I^- \cdot Y$. To check if this correlation is maintained for multisolvated iodide cluster anions, $\Delta\beta_{max}$ is plotted against $\mu_{I \cdot (Y)_n}$ (see Table 5.1) in Figure 5.8. The data includes all the solvents studied in Chapter 4. Note that for $I^- \cdot (CH_3CN)_2$, two data points are plotted, corresponding to the head-to-tail and the asymmetric conformers. The dashed line in the figure is a linear fit to the data for monosolvated iodide cluster anions only. The $\Delta\beta_{max}$ values for multisolvated iodide clusters are a little lower than for monosolvated cluster anions at comparable dipole moments. This may be evidence that the dynamics following photodetachment from cluster anions of different cluster size affects the magnitude of $\Delta\beta_{max}$. However the correlation between $\mu_{I \cdot (Y)_n}$ and $\Delta\beta_{max}$ is still reasonably strong. Below the PADs for the di- and tri-solvated iodide clusters in terms of dynamics that may affect $\Delta\beta_{max}$ are discussed in detail.

5.4.2.1 $I^- \cdot (CH_3CN)_n$ $(n = 1\text{--}2)$ clusters

In comparison with $I^- \cdot CH_3CN$, the eKE evolution of β_I for $I^- \cdot (CH_3CN)_2$ as shown in Figure 5.4 is somewhat unexpected. Based on the magnitude of the dipole moment of conformer III of $I \cdot (CH_3CN)_2$, the measured $\Delta\beta_{max}$ and β_{max} are contrary to the expectation of larger values than for monosolvated cluster anion. The kinetic energy of the electrons corresponding to β_{max} however is in agreement with an increased dipole moment. It was argued previously that for $I^- \cdot CH_3CN$, the anomaly in β_I near the threshold of Channel II has the same origin as the enhancement of the photoneutral action yield near the Channel I threshold studied by Dessent et al.[28].

The $I^- \cdot (CH_3CN)_2$ 266 nm photoelectron spectrum of Dessent et al. (Figure 5.9a) is similar to our 300 and 305 nm spectra (dashed spectrain Figure 5.2). In this case, their photoneutral action spectrum shows two bands A and B as shown in Figure 5.9b. Based on ion-dipole electrostatic modeling, which predicts the existence of the symmetric and head-to-tail conformers only, the stronger band in the photoelectron spectrum was assigned to the symmetric conformer and the weaker band to the head-to-tail conformer. This assignment was due in part to the fact that the symmetric conformer should barely enhance the photoneutral signal due to a net dipole moment of zero while the head-to-tail conformer's large dipole moment leads to more enhancement in the photoneutral signal despite being present in smaller amounts[28]. To support their assignment Dessent et al. were able to mass spectrometrically detect the $(CH_3CN)_2^-$ photofragment, after excitation of $I^- \cdot (CH_3CN)_2$ to energies near band A in the photoneutral spectrum[187]. Electric field detachment of the excess electron proved that $(CH_3CN)_2^-$ is a dipole-bound anion $[CH_3CN \cdots CH_3CN]^-$. Of the two conformers (head-to-tail and symmetric conformer) only the head-to-tail is expected to result in such a dipole-bound anion.
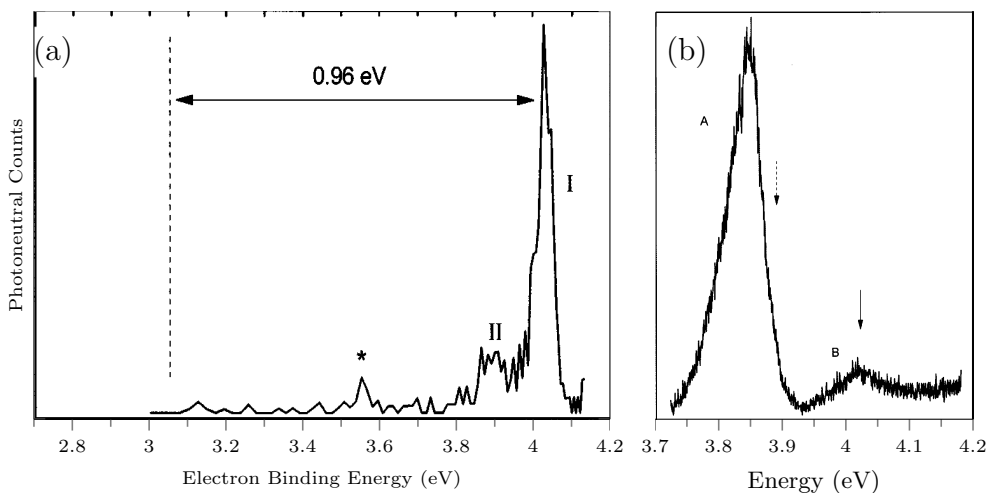
Figure 5.9: (a) Photoelectron spectrum of $I^- \cdot (CH_3CN)_2$ at 266 nm. (b) The fast photoneutral spectrum of $I^- \cdot (CH_3CN)_2$, The solid arrow marks the VDE of feature I in the spectrum on the left, while the dashed arrow marks the VDE of feature II. Reprinted with permission from: Dessent, C. E. H., Bailey, C. G. and Johnson, M. A., *J. Chem. Phy.* **103**, 2006, (1995). Copyright 1995, American Institute of Physics.

However, Timerghazin et al.[182] calculated *ab initio* cluster anion geometries of $I^- \cdot (CH_3CN)_2$ at MP2 level of theory. Three conformers were predicted as presented in Figure 5.3. Thus, in addition to the head-to-tail and symmetric conformers predicted by Dessent et al., *ab initio* results predict the existence of an asymmetric conformer. The order of stabilities of the conformers calculated using coupled cluster theory with single, double and perturbative triple excitations (CCSD(T)) is asymmetric≈symmetric>head-to-tail. The stability of the asymmetric conformer was ascribed to hydrogen bonding between I and C⋯H segments[182].

Furthermore, Timerghazin et al. calculated the excitation energies for $I^- \cdot (CH_3CN)_2$ conformers using time dependent density functional theory (TD-DFT). Excitation energies for the first excited states are 2.8, 3.57 and 3.64 eV for the head-to-tail, symmetric and asymmetric conformer respectively. Based on these results the authors concluded that the features in the photoelectron spectra of Dessent et al. are due to the asymmetric and symmetric conformer and not the asymmetric and head-to-tail conformers as originally assigned.

The photoelectron angular distributions offer confirmation that the head-to-tail conformer is not responsible for the enhancement in the photoneutral spectrum. The observed $\Delta\beta_{max}$ is not consistent with the large dipole moment of the head-to-tail conformer (data point i in Figure 5.8).

The high pressure spectra (dashed spectra in Figure 5.2) are similar to the 266 nm spectrum of $I^- \cdot (CH_3CN)_2$ obtained by Dessent et al. This suggests that at these conditions our anion source produces two conformers as in their experiment. Our calculated vertical detachment energies for the symmetric and asymmetric conformers are very close to each other (3.99 and 3.96 eV respectively) and to the experimental VDE. The calculated VDE for the head-to-tail conformer is however significantly lower than the other two and significantly lower than the experimental value. These VDE values are consistent with the relative values of the excitation energies of $I^- \cdot (CH_3CN)_2$ calculated by Timerghazin et al. Therefore the two features in our high pressure spectra and the 266 nm spectrum of Dessent and co-workers must be assigned to the asymmetric and symmetric conformers.

The 259 nm photoelectron spectrum of Figure 5.2 (corresponding to $\Delta\beta_{max}$ and β_{max}) only shows evidence of a single conformer with a binding energy close to that of our

calculations for the symmetric or asymmetric conformer. Thus the presence of the lower binding energy head to tail structure in our experiment may be ruled out. The PAD for photodetachment from the conformer that is present shows rapid change of β_I near the Channel II threshold as shown in Figure 5.4. A symmetric conformer is not expected to show this behavior due to its lack of net dipole moment. The main band in our spectra and in the 266 nm spectrum of Dessent and co-workers is therefore assigned to the asymmetric conformer.

This assignment is consistent with the occurrence of β_{max} *below* ($\sim$160 meV) the vertical detachment energy for $I^- \cdot (CH_3CN)_2$ as expected from the behavior in $I^- \cdot (H_2O)_n$ and the monosolvated cluster anions. It is also consistent with the rationalization used above for the origin of low eKE autodetachment feature near the threshold of Channel I and its absence near the Channel II threshold. As the calculations of Timerghazin showed, only the asymmetric conformer is expected to significantly change the degeneracy of the perpendicular iodine p orbitals

With this assignment the $\Delta\beta_{max}$ values of $I^- \cdot CH_3CN$ and $I^- \cdot (CH_3CN)_2$ can be compared. The calculated dipole moment of the neutral asymmetric conformer (5.7 D) at the equilibrium geometry of the cluster anion is larger than that of $I \cdot CH_3CN$ (4.54 D) but its $\Delta\beta_{max}$ value is smaller than that of $(I \cdot CH_3CN)$. Formation of $(CH_3CN)_2^-$ (channel 5.1c) and slow electron ejection (channel 5.1e) are two possible processes that might compete with electronic autodetachment. However, the absence of the near zero eKE feature in $I^- \cdot CH_3CN$ and $I^- \cdot (CH_3CN)_2$ photoelectron spectra near the Channel II threshold rules out effects due to 5.1e. Formation of $(CH_3CN)_2^-$ is possible but should not account for a reduction in $\Delta\beta_{max}$ since separation of $I(^2P_{1/2})$ and $(CH_3CN)_2^-$ would need to be faster than separation of $I(^2P_{1/2})$ and CH_3CN^- in order to reduce $\Delta\beta_{max}$ to a value lower than that of $I^- \cdot CH_3CN$.

One plausible reason is that the size of the cluster has an effect on $\Delta\beta_{max}$. For spin-orbit relaxation to occur ($[I(^2P_{1/2}) \cdot (Y)_n]^- \longrightarrow [I(^2P_{3/2}) \cdot (Y)_n] + e^-$), the electron should be in the vicinity of the iodine atom. For large systems the presence of the solvent molecules around I may exclude the electron from the "effective volume". A similar explanation was given for increase in lifetime of $[I(^2P_{1/2}) \cdot Xe_n]^-$ (n=10–38) with n with respect to electronic autodetachment[132, 133].

5.4.2.2 $I^- \cdot (H_2O)_n$ $(n = 1\text{--}3)$ clusters

The evolution of β_I with the electron kinetic energy for the multi-solvated iodide cluster anions has an overall trend that is similar to that of the monosolvated cluster. The shift of β_{max} to lower eKE values with increase in n is in agreement with the increase in dipole moment with n for the resulting neutral cluster anion. $\Delta\beta_{max}$ for the $I^- \cdot (H_2O)_2$ cluster, shown in 5.1, is in line with expectation given the higher dipole moment for $I \cdot (H_2O)_2$. Comparison of the β_I trend in $I^- \cdot (H_2O)_3$ with its predecessor is more interesting. Both $\Delta\beta_{max}$ and the eKE corresponding to β_{max} here are marginally lower for $I^- \cdot (H_2O)_3$. The small differences in the eKE$[\beta_{max}]$ between $I^- \cdot (H_2O)_2$ and $I^- \cdot (H_2O)_3$ is consistent with a small increase in dipole moment moving from $I \cdot (H_2O)_2$ ($\mu = 4.07$ D) to $I \cdot (H_2O)_3$ ($\mu = 4.39$ D). However, on these grounds $\Delta\beta_{max}$ for $I^- \cdot (H_2O)_3$ is expected to be larger than that of $I^- \cdot (H_2O)_2$. One explanation for this discrepancy is that, as above for the $\beta_I(eKE)$ evolution in $I^- \cdot (CH_3CN)_2$ photodetachment, cluster size becomes important. Additionally, for $I^- \cdot (H_2O)_n$ cluster anions, electron loss from the dipole-bound anion by fragmentational autodetachment (Equation 5.1e), is an important process as shown by the low eKE feature in the photoelectron spectra of $I^- \cdot (H_2O)_n$ cluster anions. This process might compete with electronic autodetachment. Femtosecond time resolved studies for $I^- \cdot (H_2O)_n$ $(n = 3\text{--}10)$ near Channel I thresholds have shown that the lifetime of the dipole-bound anion, $[I(^2P_{3/2}) \cdot (H_2O)_n]^-$, with respect to fragmentational autodetachment increases with n[147]. This is expected to also hold for $[I(^2P_{1/2}) \cdot (H_2O)_n]^-$. However the increase in lifetime of $[I(^2P_{1/2}) \cdot (H_2O)_n]^-$ cannot explain the $\Delta\beta_{max}$ behavior because a longer lifetime should favor electronic autodetachment and lead to an increase in $\Delta\beta_{max}$. Since there is no experimental measurement of the lifetime of $[I(^2P_{3/2}) \cdot (H_2O)_2]^-$ one might assume, based on the observed trends that its lifetime will be shorter than that of $[I(^2P_{3/2}) \cdot (H_2O)_3]^-$. To the contrary, a factor that might affect the lifetimes of the these states is the evolution of the dipole moment of the neutral core as the cluster rearranges. Calculations of the evolution of the dipole moment of $[I \cdot (H_2O)_n]$ core mentioned earlier (Figure 5.6) predict that for $[I \cdot (H_2O)_3]^-$, the core dipole moment goes below that of $[I \cdot (H_2O)_2]^-$ after about 100 fs[150] before increasing beyond that of $I \cdot (H_2O)_2$. Since the dipole moment of $I \cdot (H_2O)_2$ is almost invariant during the first 800 fs, the dipole bound state $[I \cdot (H_2O)_2]^-$ might survive longer than $[I \cdot (H_2O)_3]^-$

resulting in higher value of $\Delta\beta_{max}$ for $[\text{I}\cdot(\text{H}_2\text{O})_2]^-$ despite having a lower initial dipole moment for the corresponding neutral core.

5.5   Summary

In this chapter photoelectron spectra and angular distributions for photodetachment from multisolvated iodide clusters have been presented. For $\text{I}^-\cdot(\text{CH}_3\text{CN})_2$, for which assignment of spectral features has been a subject of debate, our results show strong support for assignment of the transitions and dynamics to the asymmetric conformer. This conclusion is based on the observed trend in $\beta_\text{I}(\text{eKE})$ near the Channel II threshold and calculated *ab initio* geometries for the possible conformers.

The results also show the increasing complexity of the dynamics as the number of solvent molecules increases. Due to increased $\mu_{\text{I(Y)}_n}$ with n, the stability of the dipole bound states formed upon photoexcitation of $\text{I}^-\cdot(\text{Y})_n$ ($n = 1, 2, 3$) also increases with n. Unlike monosolvated iodide cluster anions, the increase in the dipole moment does not necessarily translate into an increase in $\Delta\beta_{max}$. A factor that may be affecting the electronic autodetachment is the cluster size which, for larger clusters, the electron might be kept away from the iodine atom. It could also be because competition between spin-induced relaxation induced autodetachment and other processes become important. Possible competition includes cluster anion rearrangement and fragmentation. In that regard, this suggests that the timescale of electronic autodetachment is comparable to these competing processes.

Chapter 6

Angular distributions from acetonitrile dipole-bound anion

6.1 Introduction

In Chapters 3–5, dipole-bound anions of the type $[I \cdot (Y)_n]^-$ were shown to play an important role in $I^- \cdot (Y)_n$ photodetachment in the vicinity of direct detachment thresholds. It was mentioned that excitation of $I^- \cdot (Y)_n$ to a dipole bound state results in weakening of the interaction between I and Y in $[I \cdot (Y)_n]^-$ which ultimately leads to fragmentation of the dipole bound cluster. The asymptotic products of this fragmentation may include a dipole-bound anion Y^- provided that the dipole moment of Y is within or larger than the critical range of 2-2.5 D. Of the clusters studied so far in this dissertation, solvents in this category are acetonitrile, nitromethane and acetone. Due to the high dipole moment of acetonitrile, CH_3CN^- has a relatively high electron affinity of 18.2 meV[66] and is therefore probably more stable with respect to collisional electron loss and hence easier to study than most dipole-bound anions.

Theoretically, in terms of Gaussian-type basis sets, to model a diffuse orbital with a large spatial extent the Gaussian orbital exponents have to be small[188]. Small Gaussian orbital exponents present a challenge due to convergence problems in *ab initio* energy minimizations[189]. The diffuseness of dipole bound orbitals depends on the electron affinity of the neutral molecule. The electron affinity increases with the dipole moment. Due to its relatively high dipole moment of 3.92[108], the Gaussian orbital exponents required to model the dipole bound orbital of CH_3CN^- are large compared to those required for dipole-bound anions with smaller dipole moments[189].

Beside the large dipole moment, CH_3CN possesses a number of electron-scattering shape resonances[190–192]. The lowest in energy of these is a broad π^*_{CN} shape resonance centered at 2.84 eV[192]. One might expect that photodetachment from CH_3CN^- will be affected by this resonance if the electron kinetic energy of the detached electrons is close to the electron-scattering resonance energy. Photodetachment from CH_3CN^- was originally studied by Bailey et al.[169]. Their 1064 nm (1.165 eV) spectrum showed vibrational excitation of the CH_3CN ν_1, ν_3–ν_7 normal modes but not the ν_2 (CN stretch). However, spectra in the wings of the resonance, at 532 nm (2.33 eV) and 355 nm (3.50 eV), show the ν_2 mode as well, and the other modes (ν_1, ν_3–ν_7) are mildly enhanced. The enhancement of these modes and the appearance of the ν_2 mode was ascribed to the presence of the π^*_{CN} resonance. However, the overall detachment cross sections do not show large enhancements at these photon energies.

In this Chapter differential cross sections for the photodetachment of CH_3CN^- at various photon energies in the range 1.165 to 3.49 eV will be presented and discussed. The range of electron kinetic energies from the photodetachment include those sufficient to access the electron scattering resonance in CH_3CN[193]. The dependence of β on the kinetic energy of the detached electron will be monitored. To help with the interpretation of the observed trend in angular distributions calculations based on the zero-core contribution method[194], which is described briefly in Section 6.4.1, are performed.

6.2 Experimental

CH_3CN^- was produced according to the method of Bailey et al.[169] in which $I^- \cdot CH_3CN$ is photoexcited to a dipole bound state $[I(^2P_{3/2}) \cdot CH_3CN]^-$ just below the threshold of vertical detachment. The cluster dipole-bound anion fragments to give CH_3CN^- which can be probed *in situ* by photodetaching the excess electron with another delayed laser pulse of the same or different energy[169]. The 3rd (355 nm) harmonic of the Nd-YAG laser was used for the initial excitation. $I^- \cdot CH_3CN$ was produced as in Chapter 4. The dipole-bound anion was probed at various wavelengths including 1064 nm (Nd-YAG fundamental), 532 nm, 355 nm (Nd-YAG harmonics)

and 640 nm, 448 nm and 382 nm (dye laser with styryl 8 and coumarin 450). Both the pump and probe lasers were linearly and parallel polarized.

For practical experimental considerations, due to weaker output from the dye laser at 448 nm and 382 nm, high fluences of the pump laser were used at these wavelengths to increase the dipole-bound anion yield. This also results in increased (one color two photon) detachment from the anion. Because of the proximity of the 355 and 382 nm transitions a subtraction scheme is employed for the 382 nm collection. One color pump (355 nm) and probe (382 nm) spectra are subtracted from the two color spectrum.

6.3 Results

The electron kinetic energy spectra obtained at different wavelengths are shown in Figure 6.1. All the bands in the spectra are due to photodetachment from CH_3CN^-. The higher electron kinetic energy feature in the 448 nm spectrum is due to one color two photon detachment from CH_3CN^- at 355 nm. The spectra at 532 nm, 448 nm, 382 nm and 355 nm lie somewhere within the range of the π^*_{CN} resonance and display weak unresolved features on the low energy side which appear as shoulders, making the main bands appear asymmetrical. These features are due to the weak vibrational excitations reported by Bailey et al.[169].

Photoelectron angular distribution anisotropy parameters β are plotted in Figure 6.2 for the photon energies used. The values reported here are for the main peak in each spectrum (the ν_{0-0} vibrational transition) across its FWHM and therefore exclude any of the weak features on the low energy side. The distributions display a preference for polarization of the PAD parallel to the laser electric field (β is positive) but becomes less polarized as the eKE increases.
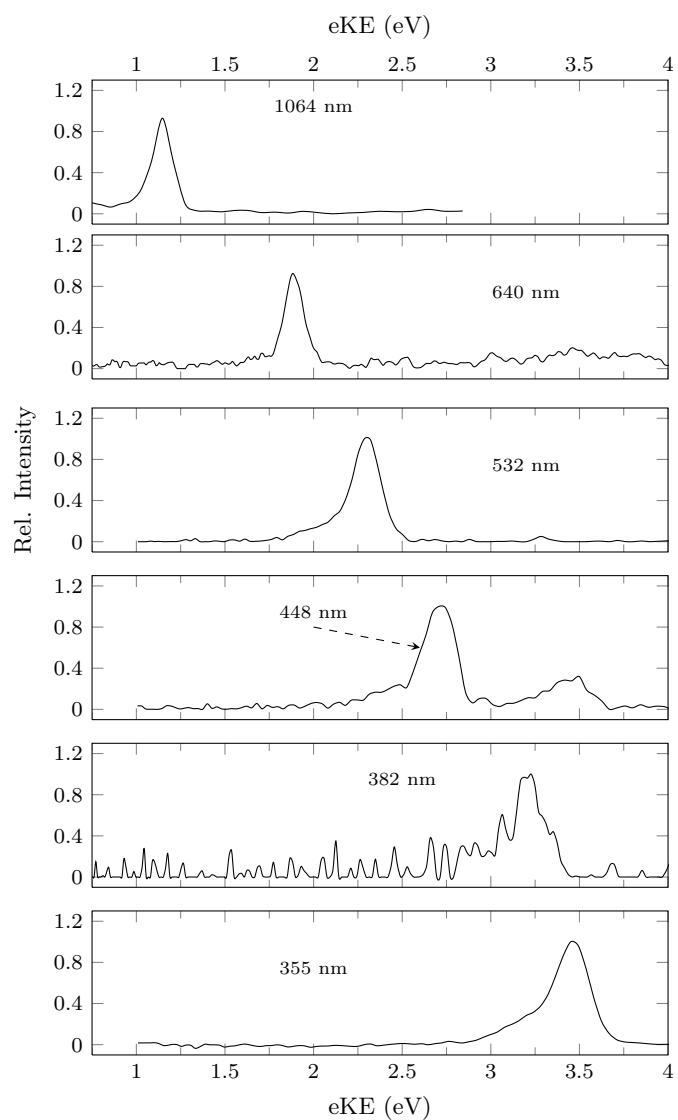
Figure 6.1: Photoelectron spectra of CH_3CN^- at different photon energies. The higher energy feature in the 448 nm spectrum is due to detachment from CH_3CN^- at 355 nm.
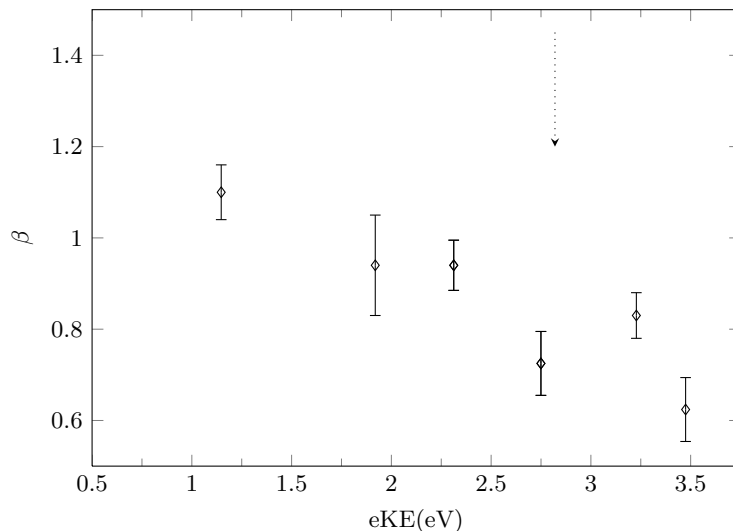
Figure 6.2: Photoelectron angular distributions for CH_3CN^-. The arrow marks the energy corresponding to the center of the π^*_{CN} scattering resonance in CH_3CN

6.4   Discussion

Despite the resolution of our experiment being lower than that of Bailey et al.[169], the vibrational excitation of the CH_3CN normal modes (ν_1–ν_7) is still evident in our spectra. The spectrum at 448 nm reported here is the closest measurement in energy to the resonance peak. Comparison of this spectrum with the 532 nm and 355 nm spectra in Figure 6.1 shows evidence of similar vibrational excitation as in the 532 nm and 355 nm. The vibrational excitation at 448 nm does not seem to be significantly enhanced compared with the 532 nm and 355 nm which probe the wings of the resonance. This is a little surprising given the antibonding nature of the π^*_{CN} orbital associated with the resonance[195]. Presumably the difference between the effects at the peaks and wings are too small to be noticeable in these experiments due to the breadth of the resonance (>1 eV).

The anisotropy parameter evolution with eKE does not seem to show any sharp changes near the peak of the resonance. Photoelectron angular distributions (characterized by β) usually mirror the behavior of total cross sections at resonances[196]. The cross section for direct photodetachment from dipole-bound anions is expected

103

to fall as $\sigma \propto (h\nu)^{-2}$[197]. The cross sections for photodetachment from CH_3CN^- measured by Bailey et al.[169] are consistent with this behavior even in the wings of the resonance (at 2.33 and 3.50 eV), although no measurements were taken at the resonance peak. This suggests that the resonance is fairly weak and direct detachment seems to dominate even in the vicinity of the resonance. However, before conclusions can be drawn concerning the effect on the resonance on β, it is important to establish the expected behavior of β in the absence of a resonance. This is because it is possible for a resonance to show a smooth evolution of the β parameter. An example is photodetachment from $I^- \cdot CH_3I$[42]. The deviation of β_I values for photodetachment from this cluster anion from those of I^- at electron kinetic energies less than 0.8 eV is pronounced. However the $\beta_I(eKE)$ evolution is fairly smooth over about 0.8 eV[42].

In Chapter 1, it was mentioned that photoelectron angular distributions are sensitive to the nature of the detachment orbital. Within the dipole approximation and ignoring relativistic effects, photoelectron angular distributions for electrons detached from a pure s orbital are kinetic energy independent and $\beta = 2$ for all photon energies. Dipole bound orbitals are usually described as largely s character with minor p contribution[67, 198]. To account for this, *ab initio* methods routinely add diffuse sp functions to the standard basis sets to model the dipole-bound anion[189]. Therefore β for photodetachment from CH_3CN^- is expected to be energy dependent even in the absence of a resonance.

In the previous chapters, in order to understand the evolution of $\beta_I(eKE)$ in $I^- \cdot (Y)_n$ photodetachment, $\beta_I(eKE)$ was compared with $\beta_{3/2}(eKE)$ for I^-. Such a comparison is not possible in the present case. In the absence of a resonance, the evolution of the β with energy may be approximated using theoretical methods that ignore electron-molecule interactions post photodetachment. One such approximation is the zero core contribution (ZCC) method of Stehman and Woo[194, 199].

The ZCC method is based on the assumption that the excess electron wave function can be approximated as lying outside a "core" (containing all the other electrons) of radius r_0. The core does not contribute to photodetachment cross section. The properties of the detachment can be obtained within the one electron approximation using this wavefunction. This method has been applied to several covalently bound monoatomic anions with some success. It has also been extended to both

homonuclear[200] and heteronuclear diatomics[201]. In this section, this method will be applied to study photodetachment from CH_3CN^-. Although this is the first time it has been applied to a dipole-bound anion, in many ways dipole-bound anions are ideal applications for this method given the diffuse nature of the orbital involved and the distance that the electron is from the molecular framework. The treatment presented is not meant to be a rigorous theoretical study of the photodetachment from a dipole bound state, but is sufficient to show the expected trend for the β(eKE) from a dipole-bound anion.

6.4.1 Photodetachment from a dipole bound orbital-β(eKE) behavior using the zero-core-contribution method

Details of the zero-core-contribution method can be found in references [194] and [199]. Here a brief outline of the approach and show details relevant to the application of the method to dipole-bound anions is presented.

In terms of the dipole-length matrix elements the photodetachment differential cross section is written as[194]

$$\frac{\mathrm{d}\sigma}{\mathrm{d}\Omega} = (2\pi)^2 \frac{e^2}{\hbar c} \frac{m_e \kappa \omega}{\hbar} \int |M_{fi}(\hat{m})|^2 \frac{\mathrm{d}\Omega}{4\pi} \tag{6.1}$$

Where the symbols are defined as in Chapter 1 and $M_{fi}(\hat{m})$ is the orientation dependent electronic dipole matrix element connecting the initial, $i\rangle$, and final state, $f\rangle$.

$$M_{fi}(\hat{m}) = \langle \psi_f | \boldsymbol{\varepsilon}_p \cdot \vec{r} | \psi_i \rangle \tag{6.2}$$

In the ZCC model, the calculation of $M_{fi}(\hat{m})$ is simplified by assuming that the excess electron has a unity probability of being outside a core "neutral atom" of radius r_0. Within any $r < r_0$, $M_{fi}(\hat{m})$=0. In addition $|\psi_i\rangle$ and $|\psi_f\rangle$ are expressed as products of unperturbed atomic wavefunctions and the wavefunction of the excess electron.
In this model ψ_f is a plane wave;

$$\psi_f(\hat{r}) = \frac{1}{\left(\sqrt{2\pi}\right)^3} \exp i\vec{\kappa} \cdot \vec{r} \tag{6.3}$$

105

In line with the approximations for a dipole bound orbital, the detachment orbital ψ_i is constructed from a linear combination of s and p_z atomic orbitals.

$$\psi_i(\hat{r}) = \exp(\pm i\phi) f(r, \theta) \tag{6.4}$$

where

$$f(r, \theta) = c_0 \psi_s(r) + c_1 \psi_{p_z}(r, \theta) \tag{6.5}$$

c_0 and c_1 are the relative contributions of the s and p_z atomic orbitals to the dipole bound orbital respectively. $\psi_s(r)$ and $\psi_{p_z}(r, \theta)$ are products of radial wavefunctions and spherical harmonic functions.

$$\psi_\ell(\vec{r}) = R_\ell(r) Y_{\ell,m}(\theta, \phi) \tag{6.6}$$

The radial wavefunction, $R_\ell(r)$, is defined only for r>r_0 such that;

$$\frac{1}{r^2}\frac{d}{dr}r^2\frac{dR_\ell}{dr} - \frac{\ell(\ell+1)R_\ell}{r^2} = \gamma^2 R_\ell \tag{6.7}$$

where $\gamma = \sqrt{2m\mathrm{E_A}}/\hbar$ and $\mathrm{E_A}$ is the electron affinity. Under the ZCC approximation, the radial functions are only normalized outside the core region

$$\int_{r_0}^{\infty} |R_\ell(r)|^2\, dr = 1 \tag{6.8}$$

For $\ell = 0$, the solution for R_0 is

$$R_0 = N_0\frac{\exp(-\gamma r)}{r} \tag{6.9}$$

where the normalization constant N_0 is

$$N_0 = \sqrt{2\gamma \exp(2\gamma r_0)} \tag{6.10}$$

For $\ell = 1$,

$$R_1 = N_1\frac{\exp(-\gamma r)}{r}\left(1 + \frac{1}{\gamma r}\right) \tag{6.11}$$

and

$$N_1 = \sqrt{\frac{2\gamma \exp(2\gamma r_0)}{1 + \frac{1}{\gamma r_0}}} \tag{6.12}$$

106

The spherical harmonic functions $Y_{\ell,m}$ are

$$Y_{00} = \frac{1}{\sqrt{4\pi}} \tag{6.13}$$

$$Y_{10} = \sqrt{\frac{3}{4\pi}} \cos\theta \tag{6.14}$$

To carry out the computations, an orientation averaged electronic transition dipole matrix element is calculated;

$$D^2(\kappa) = \frac{1}{4\pi} \int |M_{fi}(\hat{m})|^2 \, d\Omega \tag{6.15}$$

For convenience, a coordinate system in which the z-axis lies along the dipole axis of the molecular anion is used. The orientation of the spherical coordinates r, θ and φ relative to the space fixed coordinates is specified by the Euler angles α, β and δ. In this coordinate system, ψ_f is given by;

$$\psi_f = \frac{1}{\left(\sqrt{2\pi}\right)^3} \exp\left[i\kappa r \left(\sin\alpha \sin\left(\varphi + \delta\right)\sin\theta + \cos\alpha\cos\theta\right)\right] \tag{6.16}$$

and the dipole operator is

$$\varepsilon_p \cdot \vec{r} = \sin\chi \left[\cos\beta\sin\theta\cos\left(\varphi + \delta\right) - \cos\alpha\sin\beta\sin\theta\sin\left(\varphi + \delta\right) + sin\alpha\sin\beta\cos\theta\right]$$
$$+ r\cos\chi \left[\sin\alpha\sin\left(\varphi + \delta\right) + \cos\alpha\cos\theta\right] \tag{6.17}$$

Where χ is the angle between the laser electric field and the direction of the photoelectron. The dipole matrix element $M_{fi}(\hat{m})$ is

$$M_{fi}(\hat{m}) = \int\int\int \psi_f^* \, \varepsilon_p \cdot \vec{r} \, \psi_i \, r^2 \sin\theta \, d\varphi \, d\theta \, dr \tag{6.18}$$

The integrals are performed for values of r greater than r_0. Integrating over φ using ψ_i and ψ_f as defined above, the quantity $D^2(\kappa)$ is given by

$$
\begin{aligned}
D^2(\kappa) = \frac{1}{4\pi} \int_0^\pi \frac{1}{2} \Big[& \sin^2\chi \left(\left(I_2^2 + I_1^2\right)\cos^2\alpha + \left(I_3^2 + I_4^2\right)\sin^2\alpha + 2\left(I_2 I_4 - I_1 I_3\right)\cos\alpha\sin\alpha \right) \\
& + \cos^2\chi \left(\left(I_1^2 + I_2^2\right)\sin^2\alpha + \left(I_3^2 + I_4^2\right)\cos^2\alpha + 2\left(I_1 I_3 - I_2 I_4\right)\sin\alpha\cos\alpha \right) \Big] \\
& \sin\alpha \, \mathrm{d}\alpha
\end{aligned}
$$

(6.19)

Where

$$
I_1 = \int_{r_0}^\infty \int_0^\pi \cos\left(\kappa r\cos\alpha\cos\theta\right) c_0 R_0 Y_{00} J_1\left(\kappa r\sin\alpha\sin\theta\right) \sin^2\theta \; r^3 \; \mathrm{d}\theta \; \mathrm{d}r \tag{6.20}
$$

$$
I_2 = \int_{r_0}^\infty \int_0^\pi \sin\left(\kappa r\cos\alpha\cos\theta\right) c_1 R_1 Y_{10} J_1\left(\kappa r\sin\alpha\sin\theta\right) \sin^2\theta \; r^3 \; \mathrm{d}\theta \; \mathrm{d}r \tag{6.21}
$$

$$
I_3 = \int_{r_0}^\infty \int_0^\pi \sin\left(\kappa r\cos\alpha\cos\theta\right) c_0 R_0 Y_{00} J_0\left(\kappa r\sin\alpha\sin\theta\right) \sin\theta\cos\theta \; r^3 \; \mathrm{d}\theta \; \mathrm{d}r \tag{6.22}
$$

$$
I_4 = \int_{r_0}^\infty \int_0^\pi \cos\left(\kappa r\cos\alpha\cos\theta\right) c_1 R_1 Y_{10} J_0\left(\kappa r\sin\alpha\sin\theta\right) \sin\theta\cos\theta \; r^3 \; \mathrm{d}\theta \; \mathrm{d}r \tag{6.23}
$$

J_0 and J_1 are Bessel functions of the first kind. The differential cross section is then calculated as

$$
\frac{\mathrm{d}\sigma}{\mathrm{d}\Omega} = (2\pi)^2 \frac{m_e \kappa \omega}{\hbar} D^2(\kappa) \tag{6.24}
$$

The anisotropy parameter β is calculated from the differential cross section as[202]

$$
\beta = \frac{2\left(\sigma_\parallel - \sigma_\perp\right)}{\sigma_\parallel + 2\sigma_\perp} \tag{6.25}
$$

where $\sigma_\parallel$ and $\sigma_\perp$ are the differential cross sections calculated at $\chi=0$ and $\chi=\pi/2$ respectively. The above integrals are computed numerically. Simpson's method was used for the integration of equation 6.19. For Equations 6.20–6.23 the adaptive Gauss-Konrod quadrature method as implemented in GNU Octave high level programming language was used. The only input parameters required are the core radius r_0, the electron affinity of CH_3CN (18.2 meV)[66] and the scaling factors c_0 and c_1. r_0 was arbitrarily chosen to be 1.0 a.u. Because of the large spatial extent of the dipole bound orbital, this choice of r_0 is reasonable. Using the above expressions and parameters,

the β parameter was calculated at different energies for CH_3CN^- photodetachment. To test the reasonableness of the model, β was calculated using values of c_0 and c_1 corresponding to a pure s and pure p_z-orbital respectively. In Figure 6.3, the calculated values of $\beta(eKE)$ are plotted. The model correctly predicts the energy independence of anisotropy ($\beta = 2$) for photodetachment from a pure s-orbital ($c_0 = 1$). For $c_0 = 0$ (photodetachment from a pure p_z-orbital) the $\beta(eKE)$ also behaves as expected. The shape of the trend is similar to that of I^- discussed in Chapter 3, except that the minimum in the β values occurs at very low eKE because of low electron affinity of acetonitrile.

In Figure 6.4 experimental β values for CH_3CN^- photodetachment and the ZCC calculated $\beta(eKE)$ values using $c_0 = 0.85$ and $c_1 = 0.15$ are plotted. Also plotted are calculated and experimental β values for a number of other dipole-bound anions. The ZCC calculation reproduces the experimental observation fairly well. These results suggest that in general the PADs for photodetachment from dipole bound orbital become less polarized as the kinetic energy of the photoelectrons increases.

Based on the above results from the ZCC calculation, it is concluded that the observed trends in β primarily arise from the nature of the detachment orbital and not the resonance. This points to the weakness of the resonance in agreement with the total cross section measurements of Bailey et al.[169]. In the previous chapters the effect of various resonances on the photoelectron angular distribution parameter β was noted and detailed. It was remarked concerning the effect of resonances on photodetachment from $I^- \cdot CH_3I$ and autoionizing resonances in $I^- \cdot Y$. Anisotropy differentials for detachment from $NO^- \cdot (N_2O)_n$ (n = 0–4) and $O^- \cdot (N_2O)_n$ (n = 4–9) show similar behavior at electron kinetic energies corresponding to an N_2O $^2\Pi$ shape resonance[207]. It was expected that significant deviations from the predicted β trend would be observed at kinetic energies of the electron accessing the resonance in CH_3CN^- photodetachment. The absence of any noticeable effect on β could be due to symmetry considerations. Within the dipole approximation the selection rule $\ell' = \ell \pm 1$ restricts the angular momentum values for the detached electron. Therefore the most probable value of ℓ' may not be consistent with the π^*_{CN} orbital symmetry[208, 209]. In particular it is expected that for a π^* shape resonance, the $\ell' = 2$ partial waves will interact most significantly[210]. However, this can only be due to the p component of the dipole bound orbital, which is already a weaker contribution to the overall orbital. Therefore the d-waves represent a small component of the overall outgoing
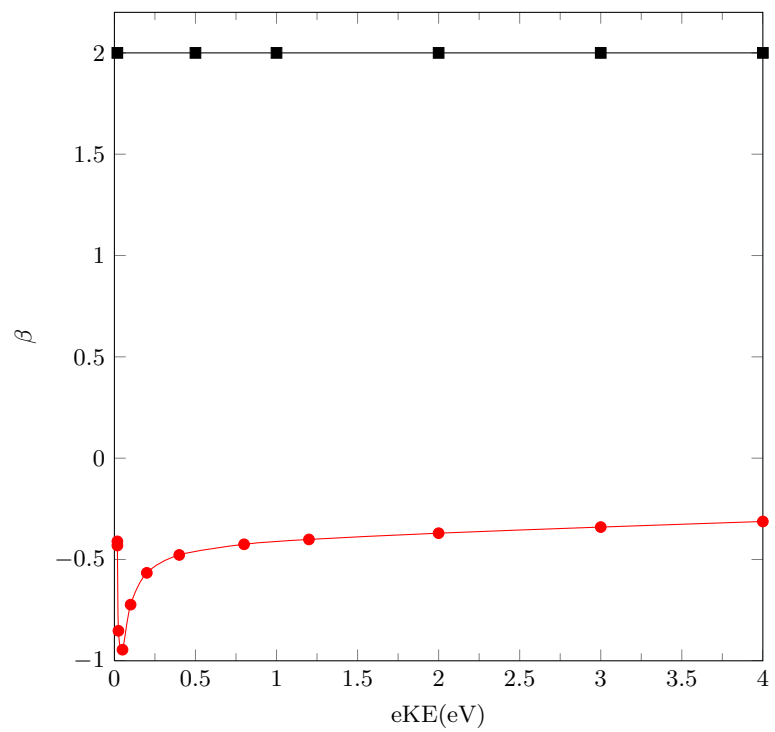
Figure 6.3: Photoelectron angular distributions for CH_3CN^- photodetachment assuming the detachment is from a pure s orbital (filled squares) and pure p_z orbital (filled circles)
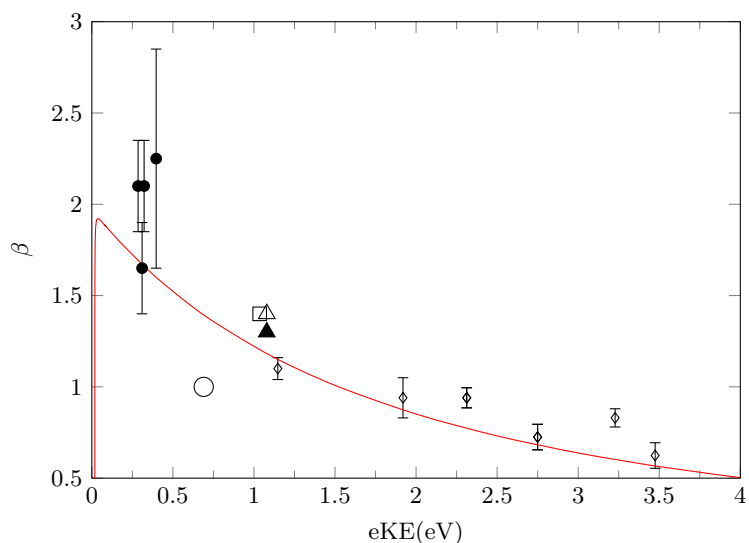
Figure 6.4: Photoelectron angular distributions of various dipole-bound anions: Experimental CH_3CN^- (diamonds), uracil DBA experiment (open triangle)[198], uracil DBA theory (filled triangle)[203], $CH_3NO_2^-$ (filled circles)[204], $(H_2O)_6^-$ (open circle)[205] and (pyridine)$_4^-$ (square)[206]. The solid line represents ZCC calculated β values for CH_3CN^- using $c_0 = 0.85$, $c_1 = 0.15$ and $r_0 = 1.0$ a.u.

wave. The dominant effect is due to the p and s partial wave contributions which are the main components in the low eKE behavior of the predicted beta behavior of Figure 6.4

6.5 Summary

Photoelectron spectra and angular distributions for CH_3CN^- photodetachment have been measured at different photon energies. The 2.77 eV spectrum, near the peak of the π_{CN}^* resonance (2.84 eV) shows about the same level of vibrational excitation of CH_3CN modes (ν_1–ν_7) as spectra at the wings of the resonance (2.33 eV and 3.49 eV). This is probably due to the broadness of the resonance itself which makes the difference in spectra at different energies too weak to detect.

The angular distributions characterized by β show a predominantly parallel transition for the detachment which becomes less anisotropic as eKE increases. This behavior

is consistent with photodetachment from a dipole bound orbital as demonstrated using the zero-core contribution method. There are no appreciable effects of the resonance on β. It is concluded that the resonance effect is weak compared to the direct detachment channel. This is because higher angular momentum partial wave (in particular the d partial wave) cross sections are weak due to small p contribution to the overall dipole bound orbital.

Chapter 7

Summary and conclusions

In this dissertation dipole moment effects on photodetachment have been studied experimentally. Photodetachment from $I^- \cdot (Y)_n$ accesses two neutral states each associated with the spin-orbit states of I, $I(^2P_{3/2}) \cdot (Y)_n$ and $I(^2P_{1/2}) \cdot (Y)_n$, labeled Channels I and II, respectively. Associated with each neutral state are dipole-supported states $[I(^2P_{3/2}) \cdot (Y)_n]^-$ and $[I(^2P_{1/2}) \cdot (Y)_n]^-$ mainly due to the dipole moment of the neutral $[I(^2P_{3/2}) \cdot (Y)_n]$ and $[I(^2P_{1/2}) \cdot (Y)_n]$ frameworks. Beside the direct detachment channels, in which the electron kinetic energy is dependent on the photon energy, in some cases electrons whose (typically low) kinetic energies are independent of photon energies are observed. These are typically found close to but below the Channels I and II thresholds and arise due to autodetachment from metastable dipole-bound states. As the neutral core fragments the dipole moment becomes too weak to bind an electron leading to electron ejection. In $I^- \cdot C_4H_5N$ photodetachment, this low eKE autodetachment channel covers an unusually wide range of photon energies below and above the Channel I direct detachment peak. This is in part because of the existence of two neutral states which asymptotically correlate to $[I(^2P_{3/2}) + C_4H_5N]$ and are due to the lifting of the iodine p orbital degeneracy.

Direct Channel I detachment below the Channel II threshold, shows very little dipole moment related effect on photodetachment from $I^- \cdot (Y)_n$. However, excitation into the vicinity of the Channel II thresholds leads to mixing between the free electron from Channel I detachment and the dipole-bound state, $[I(^2P_{1/2}) \cdot (Y)_n]^-$. Although this phenomenon occurs in the threshold of Channel II, it is manifests as rapid change in the photoelectron angular distributions for Channel I. In simple terms the neutral core in $[I(^2P_{1/2}) \cdot (Y)_n]^-$ relaxes to $[I(^2P_{3/2}) \cdot (Y)_n]$ leading to the ejection of the excess

electron with a kinetic energy that is equal to that of electrons directly detached via Channel I. Interference between these two outcomes leads to the rapid change in the angular distribution as the photon energy is increased. This change has been quantified by the parameter $\Delta\beta_{max}$, which measures the maximum change of the anisotropy parameter β. For monosolvated iodide cluster anions, $\Delta\beta_{max}$ shows a strong linear correlation with the dipole moment of the neutral core, [I·Y]. As the dipole moment increases, the excess electron is kept in the vicinity of the neutral framework for longer and channel mixing is enhanced.

For multisolvated cluster anions, effects related to cluster size, rearrangement and fragmentation have been identified as some of the factors that weaken or compete with channel mixing. However, the correlation between $\Delta\beta_{max}$ and the dipole moment of the $[I \cdot (Y)_n]$ still exists, albeit to a lesser degree. In conclusion, dipole moments most strongly affect photodetachment from $I^- \cdot (Y)_n$ at energies corresponding to excitation to dipole supported states or resonances. These conditions are most usually met near the opening of excited state channels.

Taking a somewhat different approach, in the last Chapter, photodetachment from a stable CH_3CN^- dipole-bound anion was studied. The existence of an electron scattering shape resonance at 2.84 eV motivated us to study this anion. Contrary to expectation, no striking effect of this resonance on the photoelectron angular distributions at photon energies leading to production of electrons with 2.84 eV kinetic energy was observed. Instead, the distributions gradually become less polarized along the laser electric field direction as the electron kinetic energy increases. Calculations based on the zero-core contribution method, which is applied to dipole-bound anions for the first time, suggest that the observed behavior of angular distributions is due predominantly to the nature of the detachment orbital. Although the resonance clearly affects conventional electron scattering, in the photodetachment experiment, the cross section for excitation of the shape resonance is probably low due angular momentum conservation restriction.

7.1 Possible Future Experiments

The results presented above, particularly in Chapters 4 and 5 warrant further investigation. For example, iodide might be replaced with a different atomic anion. In $I^-\cdot(Y)_n$ photodetachment, the two states that are coupled to effect the observed rapid change in angular distributions are related by the spin-orbit interaction. Using anions for which two nearby states in the corresponding neutral cluster are not related by the spin-orbit interaction will shed further insight in coupling of the electronic states in solvated environments. For example, there are two low lying neutral states of O the atom (^3P and ^1D) that can be accessed by photodetachment from O^-.

Understanding the nature of the partial wave dependence of the observed phenomenon near Channel II thresholds can also be studied by using anions in which only one partial wave is allowed. In $I^-\cdot(Y)_n$ photodetachment, the excess electron is primarily localized on the iodine atom. Therefore, two partial waves are possible from the p orbital (s and d) based on selection rules. Anions for which the excess electron orbital is an s orbital, such as Cu^-, might be good candidates for such studies because for these only a p partial wave is possible. On the other hand the angular momenta dependence of the resonance in CH_3CN studied in Chapter 6 could be investigated further by solvating different atomic anions with CH_3CN.

Finally, the electronic autodetachment observed here that accompanies relaxation of the core $[I(^2P_{1/2})\cdot(Y)_n]$ to $[I(^2P_{3/2})\cdot(Y)_n]$ suggests that the excess electron not only induces relaxation but also acts as an energy bath for the excess energy. This raises the question as to whether internal modes of freedom will facilitate autodetachment in such systems. It is known, for example, that the rate constant for quenching of $I(^2P_{1/2})$ by alcohols is linearly correlated with the number of C–H bonds[211]. It is believed that more C–H bonds result in more efficient electronic-vibrational energy transfer. Assuming that a vibrational mode of Y could act as a bath, in the case of $I^-\cdot Y$, due to the large spin-orbit splitting of I, more than one quantum of any vibrational mode may be needed. The spin-orbit splittings in Br and Cl are smaller and only one quantum of vibrational excitation may be required.

References

[1] D. M. Neumark, *Phys. Chem. Chem. Phys.*, **7**, 433 (2005).

[2] A. Weaver and D. M. Neumark, *Faraday Discuss. Chem. Soc.*, **91**, 5 (1991).

[3] R. B. Metz, T. Kitsopoulos, A. Weaver and D. M. Neumark, *J. Chem. Phys.*, **88**, 1463 (1988).

[4] D. H. Zhang, M. Yang, M. A. Collins and S.-Y. Lee, *Proc. Nat. Ac. Sci.*, **99**, 11579 (2002).

[5] B. K. Janousek and J. I. Brauman, *J. Chem. Phys.*, **72**, 694 (1980).

[6] H. Hotop, T. A. Patterson and W. C. Lineberger, *J. Chem. Phys.*, **60**, 1806 (1974).

[7] J. R. Smith, J. B. Kim and W. C. Lineberger, *Phys. Rev. A*, **55**, 2036 (1997).

[8] M. Gailitis and R. Damburg, *Proc. Phys. Soc.*, **82**, 192 (1963).

[9] T. F. O'Malley, *Phys. Rev.*, **137**, A1668 (1965).

[10] P. C. Engelking, *Phys. Rev. A*, **26**, 740 (1982).

[11] E. Fermi and E. Teller, *Phys. Rev.*, **72**, 399 (1947).

[12] B. Boudaïffa, P. Cloutier, D. Hunting, M. A. Huels and L. Sanche, *Science*, **287**, 1658 (2000).

[13] L. Sanche, *Eur. Phys. J. D*, **35**, 367 (2005).

[14] J. H. Hendricks, S. A. Lyapustina, H. L. de Clercq, J. T. Snodgrass and K. H. Bowen, *J. Chem. Phys.*, **104**, 7788 (1996).

[15] T. Sommerfeld, *J. Phys. Conf. Ser.*, **4**, 245 (2005).

[16] R. N. Compton, H. S. Carman, C. Desfrançois, H. Abdoul-Carime, J. P. Schermann, J. H. Hendricks, S. A. Lyapustina and K. H. Bowen, *J. Chem. Phys.*, **105**, 3472 (1996).

[17] A. M. Scheer, K. Aflatooni, G. A. Gallup and P. D. Burrow, *Phys. Rev. Lett.*, **92**, 068102 (2004).

[18] G. H. Herbig, *Astrophys. J.*, **196**, 129 (1975).

[19] P. J. Sarre, *Mon. Not. R. Astron. Soc*, **313**, L14 (2000).

[20] P. A. Schulz, R. D. Mead, P. L. Jones and W. C. Lineberger, *J. Chem. Phys.*, **77**, 1153 (1982).

[21] D. W. Arnold, S. E. Bradforth, E. H. Kim and D. M. Neumark, *J. Chem. Phys.*, **102**, 3493 (1995).

[22] A. Mandl and H. A. Hyman, *Phys. Rev. Lett.*, **31**, 417 (1973).

[23] V. Radojević, H. P. Kelly and W. R. Johnson, *Phys. Rev. A*, **35**, 2117 (1987).

[24] M. Kutzner, J. T. Brown and J. Thorarinson, *Phys. Rev. A*, **68**, 042713 (2003).

[25] M. Y. Amusia, A. S. Baltenkov, L. V. Chernysheva, Z. Felfli and A. Z. Msezane, *Phys. Rev. A*, **72**, 032727 (2005).

[26] J. Wu and J. Yuan, *Phys. Rev. A*, **76**, 024702 (2007).

[27] C. E. H. Dessent, C. G. Bailey and M. A. Johnson, *J. Chem. Phys.*, **102**, 6335 (1995).

[28] C. E. H. Dessent, C. G. Bailey and M. A. Johnson, *J. Chem. Phys.*, **103**, 2006 (1995).

[29] C. E. H. Dessent, J. Kim and M. A. Johnson, *Faraday Discuss.*, **115**, 395 (2000).

[30] D. Serxner, C. E. H. Dessent and M. A. Johnson, *J. Chem. Phys.*, **105**, 7231 (1996).

[31] D. H. Parker, *Velocity Mapping Studies of Molecular Photodissociation and Photoionization dynamics; In Photoionization and Photodetachment Part 1* (Cheuk-Yiu Ng, ed.), World Scientific Publishing Co., Pte., Ltd., Singapore, chapter 1, 317–422 (2000).

[32] G. J. Schulz, *Rev. Mod. Phys.*, **45**, 378 (1973).

[33] G. J. Schulz, *Rev. Mod. Phys.*, **45**, 423 (1973).

[34] H. Hotop, M. -W. Ruf, M. Allan and I. I. Fabrikant, *Adv. At. Mol. Opt. Phys.*, **49**, 85 (2003).

[35] E. Leber, S. Barsotti, J. Bömmels, J. M. Weber, I. I. Fabrikant, M. -W. Ruf and H. Hotop, *Chem. Phys. Let.*, **325**, 345 (2000).

[36] T. A. Patterson, H. Hotop, A. Kasdan, D. W. Norcross and W. C. Lineberger, *Phys. Rev. Lett.*, **32**, 189 (1974).

[37] C. M. Lee, *Phys. Rev. A*, **11**, 1692 (1975).

[38] K. J. Reed, A. H. Zimmerman, H. C. Andersen and J. I. Brauman, *J. Chem. Phys.*, **64**, 1368 (1976).

[39] J. Cooper and R. N. Zare, *Photoelectron Angular Distributions; in Volume XI of Lectures in Theoretical Physics*, Gordon and Breach, Inc, New York, 317–337 (1969).

[40] J. Cooper and R. N. Zare, *J. Chem. Phys.*, **48**, 942 (1968).

[41] J. L. Hall and M. W. Siegel, *J. Chem. Phys.*, **48**, 943 (1968).

[42] M. Van Duzor, J. Wei, F. Mbaiwa and R. Mabbs, *J. Chem. Phys.*, **131**, 204306 (2009).

[43] G. Aravind, N. Bhargava Ram, A. K. Gupta and E. Krishnakumar, *Phys. Rev. A*, **79**, 043411 (2009).

[44] D. Calabrese, A. M. Covington, W. W. Williams, D. L. Carpenter, J. S. Thompson and T. J. Kvale, *Phys. Rev. A*, **71**, 042708 (2005).

[45] R. Mabbs, E. R. Grumbling, K. Pichugin and A. Sanov, *Chem. Soc. Rev.*, **38**, 2169 (2009).

[46] A. D. Buckingham, B. J. Orr and J. M. Sichel, *Phil. Trans. Royal Soc. London. Ser. A*, **268**, pp. 147 (1970).

[47] M. Van Duzor, F. Mbaiwa, J. Wei, T. Singh, R. Mabbs, A. Sanov, S. J. Cavanagh, S. T. Gibson, B. R. Lewis and J. R. Gascooke, *J. Chem. Phys.*, **133**, 174311 (2010).

[48] E. Surber, R. Mabbs and A. Sanov, *J. Phys. Chem. A*, **107**, 8215 (2003).

[49] E. P. Wigner, *Phys. Rev.*, **73**, 1002 (1948).

[50] D. Hanstorp, C. Bengtsson and D. J. Larson, *Phys. Rev. A*, **40**, 670 (1989).

[51] C.-N. Liu and A. F. Starace, *Phys. Rev. A*, **59**, 3643 (1999).

[52] J. Xi and C. F. Fischer, *J. Phys. B*, **32**, 387 (1999).

[53] T. A. Patterson, H. Hotop, A. Kasdan, D. W. Norcross and W. C. Lineberger, *Phys. Rev. Lett.*, **32**, 189 (1974).

[54] G. Haeffler, I. Y. Kiyan, D. Hanstorp, B. J. Davies and D. J. Pegg, *Phys. Rev. A*, **59**, 3655 (1999).

[55] J. W. Farley, *Phys. Rev. A*, **40**, 6286 (1989).

[56] J. Sandström, G. Haeffler, I. Kiyan, U. Berzinsh, D. Hanstorp, D. J. Pegg, J. C. Hunnell and S. J. Ward, *Phys. Rev. A*, **70**, 052707 (2004).

[57] T. F. O'Malley, *Phys. Rev.*, **137**, A1668 (1965).

[58] O. H. Crawford and W. R. Garrett, *J. Chem. Phys.*, **66**, 4968 (1977).

[59] O. H. Crawford, *Mol. Phys.*, **20**, 585 (1971).

[60] J. A. Stockdale, F. J. Davis, R. N. Compton and C. E. Klots, *J. Chem. Phys.*, **60**, 4279 (1974).

[61] G. H. Lee, S. T. Arnold, J. G. Eaton and K. H. Bowen, *Chem. Phys. Let.*, **321**, 333 (2000).

[62] A. H. Zimmerman and J. I. Brauman, *J. Chem. Phys.*, **66**, 5823 (1977).

[63] A. S. Mullin, K. K. Murray, C. P. Schulz and W. C. Lineberger, *J. Phys. Chem.*, **97**, 10281 (1993).

[64] R. Hashemi and E. Illenberger, *J. Phys. Chem.*, **95**, 6402 (1991).

[65] C. Desfrançois, B. Baillon, J. P. Schermann, S. T. Arnold, J. H. Hendricks and K. H. Bowen, *Phys. Rev. Lett.*, **72**, 48 (1994).

[66] H. Abdoul-Carime and C. Desfrançois, *Eur. Phys. J. D*, **2**, 149 (1998).

[67] C. Desfrançois, H. Abdoul-Carime and J.-P. Schermann, *Int. J. Mol. Phys. B*, **10**, 1339 (1996).

[68] M. Matsuzawa, *J. Chem. Phys.*, **55**, 2685 (1971).

[69] A. T. J. B. Eppink and D. H. Parker, *Rev. Sci. Instr.*, **68**, 3477 (1997).

[70] J. Schiedt and R. Weinkauf, *Rev. Sci. Instr.*, **70**, 2277 (1999).

[71] J. P. Bucher, D. C. Douglass, P. Xia and L. A. Bloomfield, *Rev. Sci. Instr.*, **61**, 2374 (1990).

[72] M. L. Mandich and V. E. Bondybey, *Main group clusters: A review; in Atomic and Molecular Clusters* (E. R. Benstein, ed.), Elsevier Science Publishing Company, Inc., New York, USA, chapter 2, 69–357 (1990).

[73] M. L. Alexander, N. E. Levinger, M. A. Johnson, D. Ray and W. C. Lineberger, *J. Chem. Phys.*, **88**, 6200 (1988).

[74] D. J. Lavrich, M. A. Buntine, D. Serxner and M. A. Johnson, *J. Phys. Chem.*, **99**, 8453 (1995).

[75] T. N. Kitsopoulos, I. M. Waller, J. G. Loeser and D. M. Neumark, *Chem. Phys. Let.*, **159**, 300 (1989).

[76] D. H. Paik, N. J. Kim and A. H. Zewail, *J. Chem. Phys.*, **118**, 6923 (2003).

[77] E. Roberts, S. Cavanagh, S. Gibson, B. Lewis, C. Dedman and G. Picker, *J. El. Spec. Rel. Phenom.*, **144-147**, 251 (2005).

[78] T. R. Dyke, G. R. Tomasevich, W. Klemperer and W. E. Falconer, *J. Chem. Phys.*, **57**, 2277 (1972).

[79] D. H. Levy, *Adv. Chem. Phys.*, **47**, 323 (1981).

[80] A. Kantrowitz and J. Grey, *Rev. Sci. Instr.*, **22**, 328 (1951).

[81] T. A. Miller, *Science*, **223**, pp. 545 (1984).

[82] C. E. Klots, *J. Chem. Phys.*, **83**, 5854 (1985).

[83] M. A. Johnson and W. C. Lineberger, *Pulsed methods for cluster ion spectroscopy; in Techniques for the Study of Gas-Phase Ion-Molecule Reactions,* (J. M. Farrar and W. H. Saunders, Eds.), John Wiley & Sons, New York, 591–636 (1988).

[84] D. L. Osborn, D. J. Leahy, D. R. Cyr and D. M. Neumark, *J. Chem. Phys.*, **104**, 5026 (1996).

[85] M. C. McCarthy, W. Chen, M. J. Travers and P. Thaddeus, *Astrophys. J. Supp. Ser.*, **129**, 611 (2000).

[86] W. C. Wiley and I. H. McLaren, *Rev. Sci. Instr.*, **26**, 1150 (1955).

[87] L. A. Posey, M. J. Deluca and M. A. Johnson, *Chem. Phys. Let.*, **131**, 170 (1986).

[88] Idaho National Engineering and Environmental laboratory, SIMION 3D VERSION 7.0 (SOFTWARE FOR ION OPTICS), Published by Bechtel BWXT Idaho, LLC (2000).

[89] D. W. Chandler and P. L. Houston, *J. Chem. Phys.*, **87**, 1445 (1987).

[90] C. R. Gebhardt, T. P. Rakitzis, P. C. Samartzis, V. Ladopoulos and T. N. Kitsopoulos, *Rev. Sci. Instr.*, **72**, 3848 (2001).

[91] D. Townsend, M. P. Minitti and A. G. Suits, *Rev. Sci. Instr.*, **74**, 2530 (2003).

[92] J. J. Lin, J. Zhou, W. Shiu and K. Liu, *Rev. Sci. Instr.*, **74**, 2495 (2003).

[93] V. Papadakis and T. N. Kitsopoulos, *Rev. Sci. Instr.*, **77**, 083101 (2006).

[94] R. N. Bracewell, *The Fourier Transform And Its Applications*, McGraw-Hill Companies, Inc, USA, 3rd edition (2000).

[95] V. Dribinski, A. Ossadtchi, V. A. Mandelshtam and H. Reisler, *Rev. Sci. Instr.*, **73**, 2634 (2002).

[96] E. W. Hansen and P.-L. Law, *J. Opt. Soc. Am. A*, **2**, 510 (1985).

[97] M. J. J. Vrakking, *Rev.. Sci. Inst.*, **72**, 4084 (2001).

[98] S. Manzhos and H. Loock, *Com. Phys. Comm.*, **2003**, 76 (154).

[99] T. Andersen, H. K. Haugen and H. Hotop, *J. Phys. Chem. Ref. Data*, **28**, 1511 (1999).

[100] C. E. Moore, *Natl. Stand. Ref. Data Ser. Natl. Bur. Stand.*, **35** (1971).

[101] G. Markovich, R. Giniger, M. Levin and O. Cheshnovsky, *J. Chem. Phys.*, **95**, 9416 (1991).

[102] R. Mabbs, E. Surber and A. Sanov, *J. Chem. Phys.*, **122**, 054308 (2005).

[103] M. S. Bowen, M. Becucci and R. E. Continetti, *J. Phys. Chem. A*, **109**, 11781 (2005).

[104] F. Schlicht, M. Entfellner and U. Boesl, *J. Phys. Chem. A*, **114**, 11125 (2010).

[105] Y. Zhao, C. C. Arnold and D. M. Neumark, *J. Chem. Soc., Faraday Trans.*, **89**, 1449 (1993).

[106] M. Van Duzor, J. Wei, F. Mbaiwa and R. Mabbs, *J. Chem. Phys.*, **133**, 144303 (2010).

[107] C. E. H. Dessent, C. G. Bailey and M. A. Johnson, *J. Chem. Phys.*, **105**, 10416 (1996).

[108] D. R. Lide (editor), *CRC Handbook of Chemistry and Physics*, CRC Press, Boca Raton (2010).

[109] P. A. Gale, J. L. Sessler and V. Kral, *Chem. Commun.*, 1–8 (1998).

[110] H. Miyaji, P. Anzenbacher Jr, J. L. Sessler, E. R. Bleasdale and P. A. Gale, *Chem. Commun.*, 1723–1724 (1999).

[111] P. A. Gale, P. A. Gale, L. J. Twyman, C. I. Handlin and J. L. Sessler, *Chem. Commun.*, 1851–1852 (1999).

[112] G. Cafeo, F. H. Kohnke, G. L. L. Torre, A. J. P. White and D. J. Williams, *Chem. Commun.*, 1207–1208 (2000).

[113] Y. Shao, L. Fusti-Molnar, Y. Jung, J. Kussman, C. Ochsenfeld, S. T. Brown, A. T. B. Gilbert, L. V. Slipchenko, S. V. Levchenko, D. P. O'Neill, R. A. DiStasio, Jr., R. C. Lochan, T. Wang, G. J. O. Beran, N. A. Besley, J. M. Herbert, C. Y. Lin, T. V. Voorhis, S. H. Chein, A. Sodt, R. P. Steele, V. A. Rassolov, P. E. Maslen, P. P. Korambath, R. D. Adamson, B. Austin, J. Baker, E. F. C. Byrd, H. Daschel, R. J. Doerksen, A. Dreuw, B. D. Dunietz, A. D. Dutoi, T. R. Furlani, S. R. Gwaltney, A. Heyden, S. Hirata, C. P. Hsu, G. Kedziora, R. Z. Khaliullin, P. Klunzinger, A. M. Lee, M. S. Lee, W. Liang, I. Lotan, N. Nair, B. Peters, E. I. Proynov, P. A. Pieniazek, Y. M. Rhee, J. Ritchie, E. Rosta, C. D. Sherrill, A. C. Simmonett, J. E. Subotnik, H. L. Woodcock III, W. Zhang, A. T. Bell, A. K. Chakraborty, D. M. Chipman, F. J. Keil, A. Warshel, W. J. Hehre, H. F. Schaefer III, J. Kong, A. I. Krylov, P. M. W. Gill, M. Head-Gordon, Z. Gan, Y. Zhao, D. Schultz, D. G. Truhlar, E. Epifanovsky, C. M. Oana, R. Baer, B. R. Brooks, D. Casanova, J. D. Chai, C. L. Cheng, C. Cramer, D. Crittenden, A. Ghysels, G. Hawkins, E. G. Hohenstein, C. Kelley, W. Kurlancheek, D. Liotard, E. Livshits, P. Manohar, A. Marenich, D. Neuhauser, R. Olson, M. A. Rohrdanz, K. S. Thanthiriwatte, A. J. W. Thom, V. Vanovschi, C. F. Williams, Q. Wu, and Z. Q. You, Q-CHEM, Qchem, Inc., Pittsburg, PA, 2007.

[114] M. J. Frisch, G. W. Trucks, H. B. Schlegel, G. E. Scuseria, M. A. Robb, J. R. Cheeseman, J. A. Montgomery, Jr., T. Vreven, K. N. Kudin, J. C. Burant, J. M. Millam, S. S. Iyengar, J. Tomasi, V. Barone, B. Mennucci, M. Cossi, G. Scalmani, N. Rega, G. A. Petersson, H. Nakatsuji, M. Hada, M. Ehara, K. Toyota, R. Fukuda, J. Hasegawa, M. Ishida, T. Nakajima, Y. Honda, O. Kitao, H. Nakai, M. Klene, X. Li, J. E. Knox, H. P. Hratchian, J. B. Cross, V. Bakken, C. Adamo, J. Jaramillo, R. Gomperts, R. E. Stratmann, O. Yazyev, A. J. Austin, R. Cammi, C. Pomelli, J. W. Ochterski, P. Y. Ayala, K. Morokuma, G. A. Voth, P. Salvador, J. J. Dannenberg, V. G. Zakrzewski, S. Dapprich, A. D. Daniels, M. C. Strain, O. Farkas, D. K. Malick, A. D. Rabuck, K. Raghavachari, J. B. Foresman, J. V. Ortiz, Q. Cui, A. G. Baboul, S. Clifford, J. Cioslowski, B. B. Stefanov, G. Liu, A. Liashenko, P. Piskorz, I. Komaromi, R. L. Martin, D. J. Fox, T. Keith, M. A. Al-Laham, C. Y. Peng, A. Nanayakkara, M. Challacombe, P. M. W. Gill, B. Johnson, W. Chen, M. W. Wong, C. Gonzalez and J. A. Pople, Gaussian 03, Revision C.02, Gaussian, Inc., Wallingford, CT, 2004.

[115] T. H. Dunning, *J. Chem. Phys.*, **90**, 1007 (1989).

[116] L. A. LaJohn, P. A. Christiansen, R. B. Ross, T. Atashroo and W. C. Ermler, *J. Chem. Phys.*, **87**, 2812 (1987).

[117] J. E. Combariza, N. R. Kestner and J. Jortner, *J. Chem. Phys.*, **100**, 2851 (1994).

[118] D. H. Evans, R. G. Keesee and A. W. Castleman, *J. Chem. Phys.*, **86**, 2927 (1987).

[119] E. Arunan, G. R. Desiraju, R. A. Klein, J. Sadlej, S. Scheiner, I. Alkorta, D. C. Clary, R. H. Crabtree, J. J. Dannenberg, P. Hobza, H. G. Kjaergaard, A. C. Legon, B. Mennucci and D. J. Nesbitt, *Pure Appl. Chem.*, **83**, 1619 (2011).

[120] D. H. Sutter and W. H. Flygare, *J. Am. Chem. Soc.*, **91**, 6895 (1969).

[121] S. Carles, F. Lecomte, J. P. Schermann and C. Desfrançois, *J. Phys. Chem. A*, **104**, 10662 (2000).

[122] F. Mbaiwa, J. Wei, M. Van Duzor and R. Mabbs, *J. Chem. Phys.*, **132**, 134304 (2010).

[123] V. A. Mozhayskiy and A. I. Krylov, Ezspectrum, http://Iopenshell.Usc.Edu/downloads/.

[124] A. Sanov, J. Faeder, R. Parson and W. Lineberger, *Chem. Phys. Let.*, **313**, 812 (1999).

[125] J. M. Younkin, L. J. Smith and R. N. Compton, *Theor. Chim. Acta*, **41**, 157 (1976).

[126] M. S. Bowen, M. Becucci and R. E. Continetti, *J. Chem. Phys.*, **125**, 133309 (2006).

[127] H.-Y. Chen and W.-S. Sheu, *J. Am. Chem. Soc.*, **122**, 7534 (2000).

[128] M. Bavia, F. Bertinelli, C. Taliani and C. Zauli, *Mol. Phys.*, **31**, 479 (1976).

[129] H. A. Bethe, In *Handbuch Der Physik* (Geiger, H., Scheel, W.; Eds.), Springer, Berlin, volume 24, 483 (1933).

[130] J. Cooper and R. N. Zare, *J. Chem. Phys.*, **49**, 4252 (1968).

[131] M. W. Van Duzor, *Methyl halide cluster anion photoelectron spectra and angular distributions as a probe of electron-molecule interactions*, Ph.D. thesis, Washington University in St. Louis (2011).

[132] A. V. Davis, M. T. Zanni, C. Frischkorn and D. M. Neumark, *J. Elec. Spec. Rel. Phenom.*, **108**, 203 (2000).

[133] M. T. Zanni, C. Frischkorn, A. V. Davis and D. M. Neumark, *J. Phys. Chem. A*, **104**, 2527 (2000).

[134] M. F. Fox and E. Hayon, *J. Chem. Soc., Faraday Trans. 1*, **73**, 872 (1977).

[135] M. F. Fox and E. Hayon, *J. Chem. Soc., Faraday Trans. 1*, **73**, 1003 (1977).

[136] A. French, M, S. Ikuta and P. Kebarle, *Can. J. Chem.*, **60**, 1907 (1982).

[137] R. Yamdagni and P. Kebarle, *Can. J. Chem.*, **52**, 2449 (1974).

[138] K. Hiraoka, S. Mizuse and S. Yamabe, *J. Phys. Chem.*, **92**, 3943 (1988).

[139] G. Markovich, R. Giniger, M. Levin and O. Cheshnovsky, *Z. Phy. D*, **20**, 69 (1991).

[140] G. Markovich, L. Perera, M. L. Berkowitz and O. Cheshnovsky, *J. Chem. Phys.*, **105**, 2675 (1996).

[141] G. Markovich, S. Pollack, R. Giniger and O. Cheshnovsky, *J. Chem. Phys.*, **101**, 9344 (1994).

[142] G. Markovich, S. Pollack, R. Giniger and O. Cheshnovsky, *Z. Phy. D*, **26**, 98 (1993).

[143] G. Markovich, O. Cheshnovsky and U. Kaldor, *J. Chem. Phys.*, **99**, 6201 (1993).

[144] L. Lehr, M. T. Zanni, C. Frischkorn, R. Weinkauf and D. M. Neumark, *Science*, **284**, 635 (1999).

[145] R. M. Young, M. A. Yandell and D. M. Neumark, *J. Chem. Phys.*, **134**, 124311 (2011).

[146] Y.-I. Suzuki, H. Shen, Y. Tang, N. Kurahashi, K. Sekiguchi, T. Mizuno and T. Suzuki, *Chem. Sci.*, **2**, 1094 (2011).

[147] A. Kammrath, J. R. R. Verlet, A. E. Bragg, G. B. Griffin and D. M. Neumark, *J. Phys. Chem. A*, **109**, 11475 (2005).

[148] J. A. Kloepfer, V. H. Vilchiz, V. A. Lenchenkov and S. E. Bradforth, *Chem. Phys. Let.*, **298**, 120 (1998).

[149] D. E. Szpunar, K. E. Kautzman, A. E. Faulhaber and D. M. Neumark, *J. Chem. Phys.*, **124**, 054318 (2006).

[150] M. Kołaski, H. M. Lee, C. Pak and K. S. Kim, *J. Am. Chem. Soc.*, **130**, 103 (2008).

[151] H. M. Lee, S. B. Suh and K. S. Kim, *J. Chem. Phys.*, **119**, 7685 (2003).

[152] W.-S. Sheu and Y.-T. Liu, *Chem. Phys. Let.*, **374**, 620 (2003).

[153] D. Majumdar, J. Kim and K. S. Kim, *J. Chem. Phys.*, **112**, 101 (2000).

[154] T. Takayanagi, *J. Phys. Chem. A*, **110**, 7011 (2006).

[155] H.-Y. Chen and W.-S. Sheu, *Chem. Phys. Let.*, **335**, 475 (2001).

[156] F. D. Vila and K. D. Jordan, *J. Phys. Chem. A*, **106**, 1391 (2002).

[157] Q. K. Timerghazin and G. H. Peslherbe, *J. Am. Chem. Soc.*, **125**, 9904 (2003).

[158] T. Shimanouchi, *Tables of Molecular Vibrational Frequencies, Consolidated Volume I*, National Bureau of Standards (1972).

[159] T. E. Sharp and H. M. Rosenstock, *J. Chem. Phys.*, **41**, 3453 (1964).

[160] F. Duschinsky, *Acta physicochimica U.R.S.S.*, **7**, 551 (1937).

[161] P. Chen, *Photoelectron Spectroscopy of Reactive Intermediates; in Unimolecular and Bimolecular Reactions Dynamics* (Ng, C.-Y., Baer, T. and Powis, I., eds.), John Wiley and Sons, Chichester, USA, chapter 8, 371–425 (1994).

[162] M. Kowal, R. W. Gora, S. Roszak and J. Leszczynski, *J. Chem. Phys.*, **115**, 9260 (2001).

[163] H. M. Lee and K. S. Kim, *J. Chem. Phys.*, **114**, 4461 (2001).

[164] Q. K. Timerghazin and G. H. Peslherbe, *Chem. Phys. Let.*, **354**, 31 (2002).

[165] R. Mabbs, E. Surber and A. Sanov, *Analyst*, **128**, 765 (2003).

[166] F. Mbaiwa, M. Van Duzor, J. Wei and R. Mabbs, *J. Phys. Chem. A*, **114**, 1539 (2010).

[167] R. Mabbs, M. Van Duzor, F. Mbaiwa and J. Wei, *J. Phys.: Conf. Ser.*, **194**, 012051 (2009).

[168] W. P. Hu and D. G. Truhlar, *J. Phys. Chem.*, **98**, 1049 (1994).

[169] C. G. Bailey, C. E. H. Dessent, M. A. Johnson and K. H. Bowen, *J. Chem. Phys.*, **104**, 6976 (1996).

[170] A. R. P. Rau and U. Fano, *Phys. Rev. A*, **4**, 1751 (1971).

[171] I. P. Grant, *Relativistic Quantum Theory of Atoms and Molecules: Theory and Computation*, Springer New York (2007).

[172] R. D. Mead, K. R. Lykke, W. C. Lineberger, J. Marks and J. I. Brauman, *J. Chem. Phys.*, **81**, 4883 (1984).

[173] H. Beutler, *Z. Phys*, **93**, 177 (1935).

[174] U. Fano, *Nuovo Cimento*, **12**, 154 (1935).

[175] W. R. Johnson, K. T. Cheng, K.-N. Huang and M. Le Dourneuf, *Phys. Rev. A*, **22**, 989 (1980).

[176] J. Li, L. V. Ky, Y. Qu, J. Yan, P. Zhang, H. Zhou and P. Faucher, *Phys. Rev. A*, **55**, 3239 (1997).

[177] V. Lange, M. Aymar, U. Eichmann and W. Sandner, *J. Phys. B*, **24**, 91 (1991).

[178] W. R. Johnson, C. D. Lin, K. T. Cheng and C. M. Lee, *Phys. Scr.*, **21**, 409 (1980).

[179] S. T. Manson, *Can. J. Phys.*, **87**, 5 (2009).

[180] M. Gutowski and P. Skurski, *J. Phys. Chem. B*, **101**, 9143 (1997).

[181] M. Kołaski, H. M. Lee, C. Pak, M. Dupuis and K. S. Kim, *J. Phys. Chem. A*, **109**, 9419 (2005).

[182] Q. K. Timerghazin, T.-N. Nguyen and G. H. Peslherbe, *J. Chem. Phys.*, **116**, 6867 (2002).

[183] H. Haberland, C. Ludewigt, H. Schindler and D. R. Worsnop, **81**, 3742 (1984).

[184] T. Tsurusawa and S. Iwata, *Chem. Phys. Let*, **287**, 553 (1998).

[185] G. H. Lee, S. T. Arnold, J. G. Eaton, H. W. Sarkas, K. H. Bowen, C. Ludewigt and H. Haberland, *Z. Phys. D*, **20**, 9 (1991).

[186] C. Bässmann, U. Boesl, D. Yang, G. Drechsler and E. Schlag, *Int. J. Mass Spec. Ion Proc.*, **159**, 153 (1996).

[187] C. E. H. Dessent, J. Kim and M. A. Johnson, *Acc. Chem. Res.*, **31**, 527 (1998).

[188] A. Szabo and N. S. OStlund, *Modern Quantum Chemistry: Introduction to Advanced Electronic Structure Theory*, Dover Publications, Inc (1996).

[189] P. Skurski, , M. Gutowski and J. Simons, *Int. J. Quant. Chem.*, **80**, 1024 (2000).

[190] A. P. Hitchcock, M. Tronc and A. Modelli, *J. Phys. Chem.*, **93**, 3068 (1989).

[191] P. D. Burrow, A. E. Howard, A. R. . Johnston and K. . D. Jordan, *J. Phys. Chem.*, **96**, 7570 (1992).

[192] K. D. Jordan and P. D. Burrow, *Acc. Chem. Res.*, **11**, 341 (1978).

[193] W. Sailer, A. Pelc, P. Limão-Vieira, N. Mason, J. Limtrakul, P. Scheier, M. Probst and T. Märk, *Chem. Phys. Let.*, **381**, 216 (2003).

[194] R. M. Stehman and S. B. Woo, *Phys. Rev. A*, **20**, 281 (1979).

[195] F. Edard, A. P. Hitchcock and M. Tronc, *J. Phys. Chem*, **94**, 2768 (1990).

[196] S. Tauro and K. Liu, *J. Phys. B*, **41**, 225001 (2008).

[197] V. E. Chernov, A. V. Dolgikh and B. A. Zon, *Phys. Rev. A*, **72**, 052701 (2005).

[198] J. Schiedt, R. Weinkauf, D. Neumark and E. Schlag, *Chem. Phys.*, **239**, 511 (1998).

[199] R. M. Stehman, *A zero core-contribution model for photodetachment of atomic and molecular negative ions.*, Ph.D. thesis, University of Delaware (1980).

[200] R. M. Stehman and S. B. Woo, *Phys. Rev. A*, **23**, 2866 (1981).

[201] W. B. Clodius, R. M. Stehman and S. B. Woo, *Phys. Rev. A*, **28**, 1160 (1983).

[202] C. M. Oana and A. I. Krylov, *J. Chem. Phys.*, **131**, 124114 (2009).

[203] G. A. Gallup, *Phys. Rev. A*, **80**, 012511 (2009).

[204] C. L. Adams, H. Schneider, K. M. Ervin and J. M. Weber, *J. Chem. Phys.*, **130**, 074307 (2009).

[205] R. Nakanishi and T. Nagata, *J. Chem. Phys.*, **130**, 224309 (2009).

[206] S. Y. Han, J. H. Kim, J. K. Song and S. K. Kim, *J. Chem. Phys.*, **109**, 9656 (1998).

[207] L. Velarde, T. Habteyes, E. R. Grumbling, K. Pichugin and A. Sanov, *J. Chem. Phys.*, **127**, 084302 (2007).

[208] F. H. Read, *J. Phys. B*, **1**, 893 (1968).

[209] K. H. Kochem, W. Sohn, K. Jung, H. Ehrhardt and E. S. Chang, *J. Phys. B*, **18**, 1253 (1985).

[210] S. Miyabe, D. J. Haxton, K. V. Lawler, A. E. Orel, C. W. McCurdy and T. N. Rescigno, *Phys. Rev. A*, **83**, 043401 (2011).

[211] M. S. Chiappero, R. G. Badini and G. A. Argüello, *Int. J. Chem. Kin.*, **29**, 155 (1997).

Vita

Foster Mbaiwa

Date of Birth   July 23, 1977

Place of Birth   Tutume, Botswana

Degrees   BSc. , Chemistry, May 2003
MPhil. , Inorganic chemistry, May 2005
MA, Chemistry, 2008

Publications

F. Mbaiwa, D. Dao, N. Holtgrewe, J. Lasinski and R. Mabbs, Inter-channel effects in monosolvated atomic iodide cluster anion detachment: Correlation of the anisotropy parameter with solvent dipole moment, Submitted to the *Journal of Chemical Physics*

M. Van Duzor, **F. Mbaiwa**, J. Lasinski, N. Holtgrewe and R. Mabbs, $I^- \cdot (CH_3I)_2$ photoexcitation: The influence of dipole bound states on detachment and fragmentation, *Journal of Chemical Physics* **134**, 214301 (2011)

M. Van Duzor, **F. Mbaiwa**, J. Lasinski, D. Dao, N. Holtgrewe and R. Mabbs, Near threshold $Cl^- \cdot CH_3I$ photodetachment: Apparent $^2P_{1/2}$ channel suppression and enhanced $^2P_{3/2}$ channel vibrational excitation, *Journal of Chemical Physics* **134**, 184315 (2011)

F. Mbaiwa, J. Wei, M. Van Duzor and R. Mabbs, Threshold effects in $I^- \cdot CH_3CN$ and $I^- \cdot H_2O$ cluster anion detachment: The angular distribution as an indicator of electronic autodetachment, *Journal of Chemical Physics* **132**, 134304 (2010)

F. Mbaiwa, M. Van Duzor, J. Wei and R. Mabbs, Direct and Indirect Detachment in the Iodide-Pyrrole Cluster Anion: The Role of Dipole Bound and Neutral Cluster States, *Journal of Physical Chemistry A,* **114**, 1539 (2010)

M. Van Duzor, J. Wei, **F. Mbaiwa** and R. Mabbs, I$^-$·CH$_3$X (X = Cl, Br, I) photodetachment: The effect of electron-molecule interactions in cluster anion photodetachment spectra and angular distributions, *Journal of Chemical Physics* **133**, 144303 (2010)

R. Mabbs, **F. Mbaiwa**, J. Wei, M. Van Duzor, S. T. Gibson, S. J. Cavanagh and B. R. Lewis, Observation of vibration-dependent electron anisotropy in O$_2^-$ photodetachment, *Physical Review A* **82**, 011401(R) (2010)

M. Van Duzor, **F. Mbaiwa**, J. Wei, T. Singh, R. Mabbs, A Sanov, S. J. Cavanagh, S. T. Gibson, B. R. Lewis and J. R. Gascooke, Vibronic coupling in the superoxide anion: The vibrational dependence of the photoelectron angular distribution, *Journal of Chemical Physics* **133**, 174311 (2010)

M. Van Duzor, J. Wei, **F. Mbaiwa** and R. Mabbs, The effect of intracluster photoelectron interactions in I$^-$·CH$_3$Iphotodetachment, *Journal of Chemical Physics* **131**, 204306 (2009).

R. Mabbs, M. Van Duzor, **F. Mbaiwa** and J. Wei, Intra-cluster photoelectron interactions: Scattering and dissociative attachment in halide-methyl halide cluster anions, *Journal of Physics: Conference Series* **194**, 012051 (2009)

F. Mbaiwa and C. A. L. Becker, Chelate complexes from diphosphine substitution in pentakis(arylisocyanide)cobalt(I) complexes, *Journal of Coordination Chemistry* **60**, 153 (2007)

F. Mbaiwa and C. A. L. Becker, Diphosphine substitution in pentakis(arylisocyanide)cobalt(I) complexes; ^{31}P NMR, cyclic voltammetric and ESI mass spectrometry studies, *Inorganica Chimica Acta* **359**, 1041 (2006)

December 2011

DIPOLE MOMENT IN PHOTODETACHMENT, Mbaiwa, Ph.D. 2011